Designing and development of phthalimides as potent anti-tubulin hybrid molecules against malaria

Vigyasa Singh [a,1,†], Rahul Singh Hada [b,1], Ravi Jain [a,1], Manu Vashistha [d,1], Geeta Kumari [a,1], Snigdha Singh [c,1], Neha Sharma [c,1], Meenakshi Bansal [c], Poonam [e,h], Martin Zoltner [f], Conor R. Caffrey [g], Brijesh Rathi [c,h,**], Shailja Singh [a,*]

[a] Special Centre for Molecular Medicine, Jawaharlal Nehru University, New Delhi, 110067, India
[b] Department of Life Sciences, Shiv Nadar University, Gautam Buddha Nagar, UP, 201314, India
[c] Laboratory for Translational Chemistry and Drug Discovery, Department of Chemistry, Hansraj College, University of Delhi, Delhi, 110007, India
[d] Advanced Instrumentation Research Facility, Jawaharlal Nehru University, New Delhi, 110067, India
[e] Department of Chemistry, Miranda House, University of Delhi, Delhi, 110007, India
[f] Drug Discovery and Evaluation Unit, Department of Parasitology, Faculty of Science, Charles University, BIOCEV, Vestec, Czech Republic
[g] Center for Discovery and Innovation in Parasitic Diseases, Skaggs School of Pharmacy and Pharmaceutical Sciences, University of California San Diego, 9500 Gilman Drive, La Jolla, CA, 92093, USA
[h] Delhi School of Public Health, Institute of Eminence, University of Delhi, Delhi, 110007, India

ARTICLE INFO

ABSTRACT

Constant emergence of drug-resistant *Plasmodium falciparum* warrants urgent need for effective and inexpensive drugs. Herein, phthalimide (Pht) analogs possessing the bioactive scaffolds, benzimidazole and 1,2,3-triazole, were evaluated for *in vitro* and *in vivo* anti-plasmodial activity without any apparent hemolysis, or cytotoxicity. Analogs **4(a-e)** inhibited the growth of 3D7 and RKL-9 strains at submicromolar concentrations. Defects were observed during parasite egress from or invasion of the red blood cells. Mitochondrial membrane depolarization was measured as one of the causes of cell death. Phts **4(a-e)** in combination with artemisinin exhibited two-to three-fold increased efficacy. Biophysical and biochemical analysis suggest that Pht analogs mediate plasmodial growth inhibition by interacting with tubulin protein of the parasite. Lastly, Phts **4(a-e)** significantly decreased parasitemia and extended host survival in murine model *Plasmodium berghei* ANKA infection. Combined, the data indicate that Pht analogs should be further explored, which could offer novel value to the antimalarial drug development pipeline.

1. Introduction

The constant battle with emerging drug resistance in *Plasmodium falciparum* (*Pf*) necessitates a continuous exploration and development of diverse therapeutics [1,2]. Further, resistance to the frontline chemotherapy, Artemisinin Combination Therapy (ACTs), is now threatened by the emergence of resistance [3,4]. To combat these issues, identification of new and potent antimalarial chemistries is essential, particularly those demonstrating novel modes of action and favorable pharmacological properties [5]. In this context, the molecular diversity

and high bioactivity of nitrogen-containing heterocycles have significantly contributed to the area of drug discovery. Phthalimide (Pht) scaffolds are of special interest as crucial synthons for the synthesis of various alkaloids and pharmacophores [6–9]. The high lipophilicity of Phts contributes to their favorable pharmacological applications [10]. Likewise, the *N*-containing heterocycles *i.e.*, benzimidazole and triazole are also important substructures found in various natural and synthetic alkaloids and possess therapeutic applications [11]. Further, combining bioactive scaffolds to construct hybrid molecules has emerged as an exciting exploratory idea for generating new pharmaceutical agents [12,

13]. Pht functionalized with benzimidazole and triazole display favorable ADME (absorption, distribution, metabolism, and excretion) properties, and negligible toxicity towards HepG2 cells [14]. The ADME results are shown in Table S1 (supporting information).

Our group has reported Pht analogs as potent antiplasmodial agents against various *Pf* strains, including against the chloroquine resistant strain, *Pf*7G8 [15–17]. With a view to explore the structural diversity of Phts and to identify the lead compounds against malaria, we synthesized a library of 13 known along with 5 novel Pht analogs. Firstly, all the listed Pht analogs were assessed for antiparasitic activity against *Pf*3D7, with the best five compounds **4(a-e)** displaying submicromolar 50% inhibition (IC$_{50}$) values. These hits were further evaluated for *in vitro* activity against the resistant strain, RKL-9 including in combination with ART, and an *in vivo* efficacy study in a mouse model. Finally, we demonstrated interaction of Pht analogs with αI-tubulin using biophysical, biochemical and bioinformatics analyses, which may be helpful in understanding the mechanism of action for these novel Pht antiplasmodial candidates.

2. Results and discussion

2.1. Synthesis and antiparasitic evaluation against Pf3D7 and PfRKL-9 strains, and growth progression analysis

As part of our drug discovery project, a synergistic combination of Pht, benzimidazole and triazole scaffolds against malaria was previously reported, and a few of these compound analogs 1–4 (Fig. 1) exhibited growth-inhibitory concentrations in the submicromolar range [15]. However, the potency of these molecules (1, 3 and 4) was compromised by toxicity towards the human lymphoblast cell line, U937.

Subsequently, a hit to lead approach was implemented to improve potency against *Pf* strains, limit toxicity to the human cell line and tune compound lipophilicity (Fig. 2, Pht I). The narration started with Pht I, which was reported as moderately active (IC$_{50}$ = 20 μM) against *Pf*3D7 [16]. Optimization of its chemical structure led to Pht II with significantly improved potency (IC$_{50}$ = 0.9 μM) but with some residual toxicity (CC$_{50}$ = 28.82 μM) towards U937 cells. Replacement of the fluoro group with trifluoromethyl generated a potent antiplasmodial Pht analog (4a) very low toxicity to human cells (CC$_{50}$ > 100 μM). This overall effect may be attributed to the introduction of trifluoromethyl group (-CF$_3$), which has been shown to improve activity of antimalarials by extending their plasma half-life [18].

In this manuscript, we report the synthesis and antiplasmodial assessment of five new and 13 previously reported Pht analogs (Scheme 1) [14]. Procedure for synthesis began with a simple reaction of substituted indolines (1a-d) with *ortho*-phenylenediamine in the presence of *N,N*-diisopropylethylamine (DIPEA) and 2-(1H-benzo-triazol-1-yl)-1,1,3,3-tetramethylaminium tetrafluoroborate (TBTU) as

depicted in Scheme 1. This reaction resulted in indoline-benzimidazole derivatives (2a-d), which were further propargylated to obtain their alkyne substituents (3a-d). Next, a click reaction was optimized for the synthesis of the desired compounds (4a–e) in moderate to good yield. The chemical composition of the novel Pht analogs (4a-e) was confirmed by NMR (^{1}H & ^{13}C) and mass spectroscopy (supporting information).

An initial growth inhibition assay was performed for all the listed Phts against the chloroquine (CQ) sensitive strain, *Pf*3D7. Percent growth inhibition (Table 1) of the parasites was assessed by SYBR Green assay and Giemsa staining [19,20]. Parasites treated with CQ were taken as positive control. From this, five hits **4(a-e)** were selected for the determination of inhibitory concentrations (IC$_{50}$). Three analogs **4(a-c)** significantly inhibited the growth of *Pf*3D7 with 50% inhibitory concentration (IC$_{50}$) values in submicromolar range. The other two analogs, **4c** and **4d**, displayed IC$_{50}$ values of approximately 2 μM. All five Phts also inhibited the growth of the CQ-resistant strain, RKL-9, in a dose-dependent manner (Fig. 3A–E).

Hemolytic activity of hit compounds **4(a-e)** was determined for human red blood cells (*h*RBCs), which indicated no significant lysis up to a 5 μM concentration (Fig. 3F), suggesting their selectivity towards the infected blood cells over the normal blood cells. Pht analogs **4(a-e)** displayed potent antiplasmodial activity and reduced cytotoxicity (HepG2 cells), with therapeutic indices (TI) of >135, 156, 123, 46 and 43, respectively. Also, all the hits were tolerable up to a concentration of 500 μM against HEK2GST cells, and, subsequently, the TI was significantly improved with values of >800 for the most potent compound, **4b**.

Next, the effect of Pht analogs **4(a-e)** on the growth of blood stage *Pf* was determined. Synchronized, ring-stage parasite cultures were treated with Pht analogs **4(a-e)** at their respective IC$_{50}$ concentrations and compared to untreated parasites as control. The effects of Phts **4(a-e)** on the blood specific stage of parasite growth were observed over 60 h [21–23]. The growth of untreated control parasites was normal and late ring parasites successfully reached the mid trophozoite stage with a 3-4-fold increase in parasitemia. In the presence of **4b**, many merozoites were found sticking on the red blood cell surface with only few rings being formed, indicating an invasion defect. In case of **4c** and **4e**, parasites showed a significant delay in maturation of rings associated with transformation into pyknotic trophozoites. Overall, the parasitemia remained very low, with apparent growth defect and stress response during the progression. In case of **4d**, parasites were stuck at the late schizont stage and failed to egress even after 60 hpt (hours post treatment). In case of **4a**, pyknotic trophozoites and rings were noted at 60 hpt with a reduction in the percentage parasitemia, indicating defects in invasion and egress stages (Fig. 4).
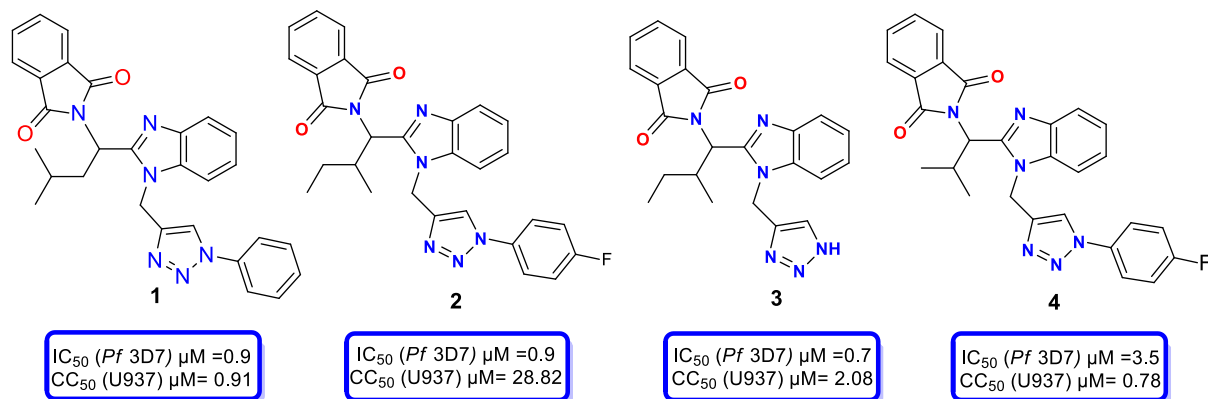

1
IC$_{50}$ (*Pf* 3D7) μM =0.9
CC$_{50}$ (U937) μM= 0.91

2
IC$_{50}$ (*Pf* 3D7) μM =0.9
CC$_{50}$ (U937) μM= 28.82

3
IC$_{50}$ (*Pf* 3D7) μM =0.7
CC$_{50}$ (U937) μM= 2.08

4
IC$_{50}$ (*Pf* 3D7) μM =3.5
CC$_{50}$ (U937) μM= 0.78

Fig. 1. Reported Pht blended heterocycles as potent *Pf*3D7 inhibitor [15].
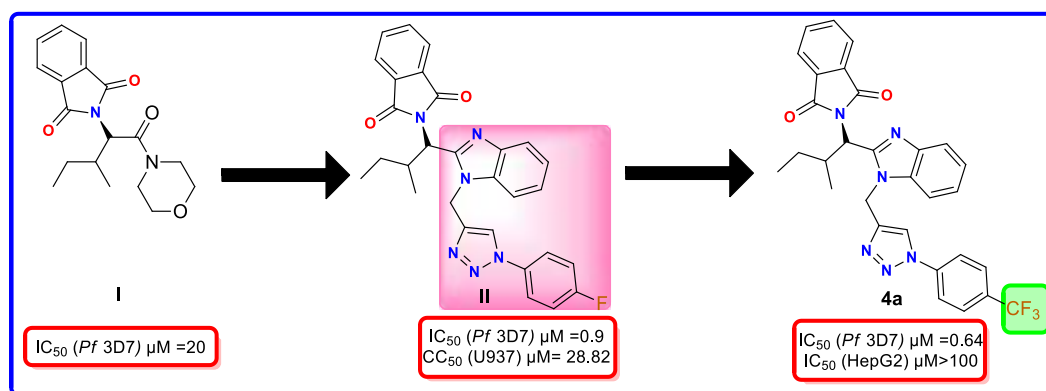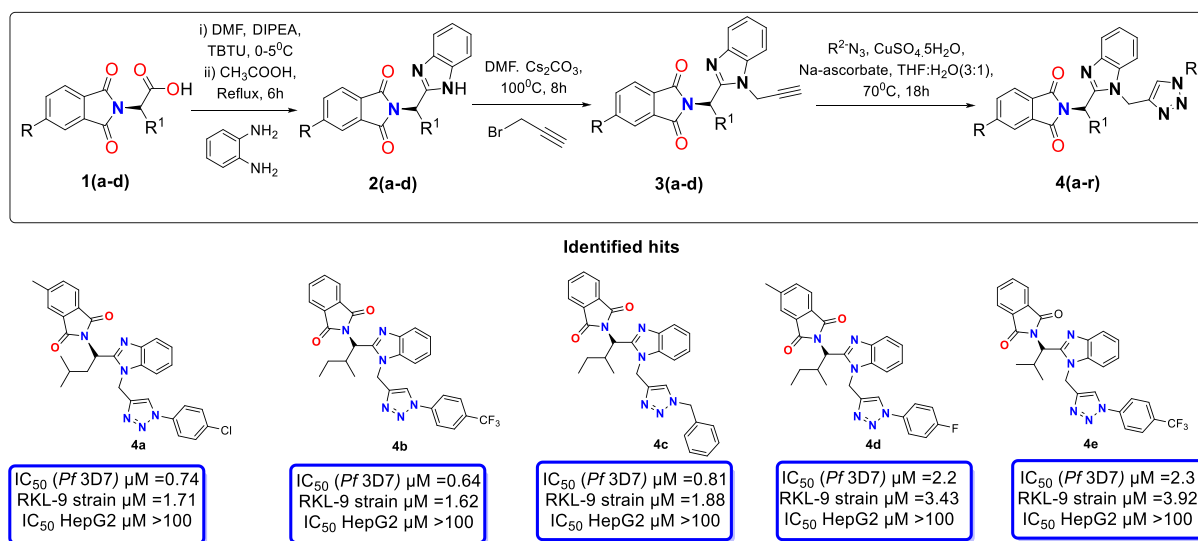
Fig. 2. Hit to lead optimization.

Scheme 1. Synthesis of Pht hit analogs **4(a-r)** and their bioactivity against *Pf*3D7 and *Pf*RKL-9 strains.

2.2. Effect of Pht analogs on mitochondrial membrane potential ($\Delta\psi_m$)

To study the effect of Pht analogs on mitochondrial membrane potential, spectrofluorometric and microscopic analyses were performed with the $\Delta\psi_m$ sensitive, cationic carbocyanin dye JC-1, which accumulates and aggregates in mitochondria dependent on $\Delta\psi_m$. This aggregation leads to a shift of emission maximum to approximately 590 nm (red fluorescence), which is different from the green fluorescent monomer [24]. The parasites were treated with Phts at their respective IC$_{50}$ concentrations. In microscopic analysis, mostly red fluorescence was observed across the untreated control erythrocytes whereas in the case of Pht analogs, an increase in mitochondrial green fluorescence was noticed. Pht analogs **4(a-e)** treated parasites showed a decreased ratio of red/green fluorescence intensity as compared to untreated control, indicating the mitochondrial dysregulation via depolarization of mitochondrial membrane (Fig. 5A). Our finding is in accordance with previous reports of antimalarial agents treated parasites indicates depolarized mitochondrial membrane [25,26]. In the spectro-fluorometric assay, the ratio of red/green fluorescence intensity at 590/530 for each of the Pht analogs at their respective IC$_{50}$ concentrations was: **4a** = 4.62 ± 0.12; **4b** = 4.61 ± 0.39, **4c** = 124.31 ± 0.13, **4d** = 5.56 ± 0.23 and **4e** = 5.06 ± 0.12, whereas for untreated controls, the ratio was 6.96 ± 0.94 (Fig. 5B).

2.3. Combination study of Pht analogs with artemisinin (ART)

A combination study was performed with *Pf*3D7 trophozoites to evaluate the effect of Pht analogs **4(a-e)** alone, and in combination with ART on the IC$_{50}$ values after 72 h. Overall, the combination of ART and Pht analogs as compared to the respective single treatment showed a gradual but significant IC$_{50}$ reduction. From the fixed ratio values, mean FIC values were plotted for seven different combinations between ART and Pht analogs to obtain an isobologram (Fig. 6). Synergistic interaction were observed in case of ART:4a combination (2:3 and 1:4) with [(Σ FIC, 0.87 (0.2 & 0.67)] and [(Σ FIC, 0.98 (0.05 & 0.93)], ART:4b combination (2:3 and 1:4) with [(Σ FIC, 0.86 (0.18 & 0.68)] and [(Σ FIC, 0.67 (0.05 & 0.62)], whereas ART:4c combination at 1:4 with [(Σ FIC, 0.67 (0.05 & 0.62)] and ART:4e combination at 1:1 with [(Σ FIC, 0.93 (0.5 & 0.43)], while additive interaction was observed in most the combinations. The results suggested a notable improvement in combination activity, especially for Phts **4a** and **4b**, respectively, which advocates their potential role as antiparasitic agents, either as standalone or combination therapies. Several combinations were reported to study interaction with or among the ART, chloroquine and quinine [27–30].

2.3.1. Role of Pf microtubule and its known inhibitors

Malaria parasites require a robust and flexible cytoskeleton to function effectively because they undergo considerable morphological changes during asexual erythrocytic development [31–33]. Apart from

Table 1
Estimation of *in vitro* percent growth inhibition of Pht analogs against *Pf*3D7 in culture.

S. No	Code	R	R¹	R²	% Inhibition 1 (µM)	10 (µM)
1.	**4a**	CH₃	CH₂CH(CH₃)₂	4-chlorophenyl	43	73
2.	**4b**	H	CH(CH₃)CH₂CH₃	4-trifluoromethylphenyl	45	68
3.	**4c**	H	CH(CH₃)CH₂CH₃	CH₂Ph	35	66
4.	**4d**	CH₃	CH(CH₃)CH₂CH₃	4-fluorophenyl	20	64
5.	**4e**	H	CH(CH₃)₂	4-trifluoromethylphenyl	22	75
6.	**4f**	CH₃	CH₂CH(CH₃)₂	4-fluorophenyl	0.3	46
7.	**4g**	CH₃	CH₂CH(CH₃)₂	4-methylphenyl	−8.63	68.9
8.	**4h**	CH₃	CH₂CH(CH₃)₂	H	−64	71
9.	**4i**	H	CH₂CH(CH₃)₂	4-trifluoromethylphenyl	−53	88
10.	**4j**	CH₃	CH₂CH(CH₃)₂	4-trifluoromethylphenyl	37	75
11.	**4k**	CH₃	CH₂CH(CH₃)₂	4-methoxyphenyl	−43	65
12.	**4l**	H	CH(CH₃)CH₂CH₃	Pentafluorophenyl	−44	77
13.	**4m**	H	CH(CH₃)CH₂CH₃	2-fluorophenyl	8	87
14.	**4n**	CH₃	CH(CH₃)CH₂CH₃	2,4-difluorophenyl	21	94
15.	**4o**	CH₃	CH(CH₃)CH₂CH₃	2-fluorophenyl	−23	91
16.	**4p**	CH₃	CH(CH₃)CH₂CH₃	Pentafluorophenyl	−4	95
17.	**4q**	H	CH(CH₃)₂	2,4-difluorophenyl	−12	88
18.	**4r**	H	CH(CH₃)₂	2,6-difluorophenyl	−26	91

microfilaments and intermediate filaments, there are other structural constituents of the eukaryotic cytoskeleton, such as microtubules seen in malaria parasites. These elements are associated with other cytoskeletal proteins such actin, actin-associated proteins, myosin, and intermediate filaments. At every stage of the parasite life cycle, a large number of microtubules are identified along the subpellicular areas of sporozoites, ookinetes, and merozoites [34–37]. Spindle microtubules are present in parasites that multiply during schizogony. These findings suggest that microtubules play a function not only in nuclear separation but also in the generation of daughter cells [38,39]. Several studies by several authors have revealed that all microtubules in Plasmodium are derived from microgametes. Plasmodium microgametes' flagellum is distinguished by the distinctive microtubule architecture seen in eukaryotic axonemes [40–43]. The flagellum is utilised to reach a macrogamete in addition to mobility and effective sexual reproduction. Given the importance of microtubules in parasite development, which includes the sporozoite, erythrocyte, gametocyte, and ookinete stages, focusing on suppressing microtubules at these phases could be a promising approach of inhibiting the parasite at different points of its life cycle.

There is evidence that significant malarial parasite disruptors, such as Paclitaxel, Docetaxel, Vincristine, Vinblastine, Dolstatin-15, and Taxol, are highly efficient against them in relevant quantities [44–47]. The fact that these inhibitors are valuable does not negate the reality that their antimalarial potential is limited. This is due to their negative impact on human cells. Other microtubule inhibitors, such as phosphorothioamide and dinitroaniline, are less toxic to mammalian cells but less efficient against human malaria parasites [48–50].

2.3.2. Analysis of the potential for tubulin modulation by Pht analogs

Microtubules are essential components of molecular machinery and mechanisms that regulate multiple cellular activities such as

intracellular trafficking, spindle formation during cell division, and cellular morphology maintenance. As a result, microtubules are viewed as an appealing macromolecular target for designing and developing chemotherapeutic drugs that regulate microtubule dynamics. In this context, the mechanistic role of commercially available and recently identified 'benzimidazole' and '1,2,3-triazole' derivatives as tubulin modulators is widely disseminated in scientific literature, indicating that these compounds have a tubulin modulation mechanism distinct from those of well-characterized clinically available tubulin modulators.

In medicinal chemistry, 'benzimidazole' is considered as a *privileged* sub-structure due to its wide recurrence in *bioactive* molecules, and has been reported to be physiologically and pharmacologically active in the treatment of both pathogenic and non-pathogenic diseases including development of anti-cancer chemotherapeutics [51]. There have been innumerous speculations regarding location of the target binding site(s) of benzimidazole in the tubulin isoforms. Some literature propose that benzimidazole interacts with β-tubulin [52–54]. However, others have suggested that the target binding site of benzimidazole is located either on α-tubulin [55,56]; or, on α-tubulin and regulated by β-tubulin [57]; or, on both α- and β-tubulins [58]; or, at the interface of α/β-tubulin heterodimer [56,59]. M. E. Oxberry et al. reported that the interaction of benzimidazole occurs with the highest affinity to α-tubulin [60].

Concomitantly, '1,2,3-triazole' sub-structure has been extensively used as a potential pharmacological *linker* to design and develop novel anti-cancer hybrids and tubulin polymerization inhibitors owing to their *anti-tubulin* effect [61–63]. Examples include, a sulfanilamide derivative which displays potent tubulin polymerization-inhibitory activity *in vitro* [64]; Combretatriazole which acts as a cytotoxic and anti-tubulin agent [65]; and, *N*-((1-Benzyl-1H-1,2,3-triazol-4-yl) methyl)arylamide which inhibits tubulin polymerization *in vitro* [66]. More recently, anti-tubulin sub-structures: Trimethoxyphenyl (TMP) and 1,2,3-triazole were conjugated (along with an anti-cancer unit) to yield a novel scaffold involved in anti-proliferative and *anti-tubulin* mechanisms [67]. Overall, literature survey indicates that 'benzimidazole' and '1,2,3-triazole' derivatives disrupt microtubule dynamics, harbor good pharmacokinetic properties and are capable of overcoming multidrug resistance in numerous cell lines.

In the same line, Pht derivatives used in this study which harbors both bioactive *anti-tubulin* scaffolds: 'benzimidazole' and '1,2,3-triazole', with antiplasmodial activity *in vitro*, were evaluated experimentally for their interaction with recombinant (r) *Pf*αI- and *Pf*β-tubulin proteins (with 6x-His tag at their *N*-termini) purified from *E. coli* strain BL21, by combining biophysical and biochemical approaches using Surface Plasmon Resonance (SPR) and Thermal Shift Assay (TSA), respectively.

2.4. Pht analog binds to and confers thermal stability to Pfα-tubulin in vitro

To test the hypothesis that the Pht analogs (n = 3) mediated *in vitro* plasmodial growth inhibition is conferred by their interaction with *Pf*tubulin isoforms (αI and/or β), Surface Plasmon Resonance (SPR)-based interaction analysis was performed for binding analysis between the Pht analogs and recombinant tubulins using AutoLab Esprit SPR, as mentioned in material and methods section. With increasing concentration of one of the Pht analogs, **4b**, a gradual increase in SPR sensor signal was observed, which linearly correlated with corresponding change in refractive index of the medium immediately adjacent to the *Pf*αI-tubulin coated SPR sensing surface, yielding a dissociation constant (K_D) value of 26.4 ± 7.6 µM. However, no such interaction was observed either for *Pf*αI-tubulin/(**4a** & **4d**) or for *Pf*β-tubulin/(**4a**, **4b** & **4d**). Concentration dependent real-time sensorgrams for *Pf*αI-tubulin/(**4a**, **4b** & **4d**) and *Pf*β-tubulin/(**4a**, **4b** & **4d**) interactions, along with respective K_D values are shown in Fig. 7a. Sensor signals obtained from the biomolecular interaction analysis were further transformed into polynomial calibration curves to show relationship between Response at
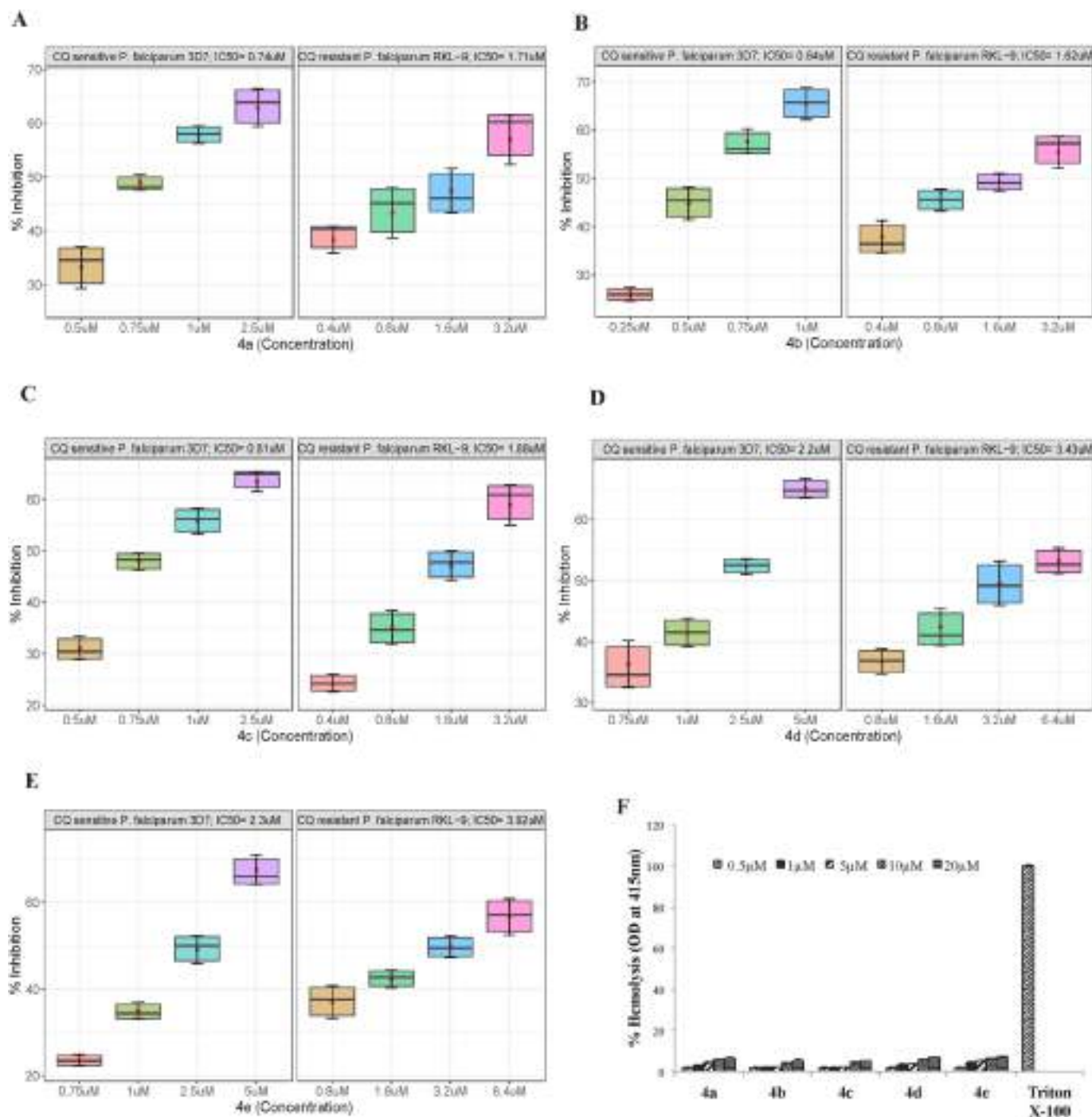
Fig. 3. Estimation of *in vitro* growth inhibition and half maximal inhibition concentration (IC$_{50}$) of Pht analogs **4(a-e)** against *Pf* 3D7 and *Pf* RKL-9 strains. Synchronized late trophozoite parasites were treated with Pht analogs from 0.025 μM to 10 μM concentrations. Graph Pad Prism 8 software was used to calculate IC$_{50}$ values. **(A–E)** Graph showing percent inhibition of Pht analogs. **(F)** Effect of Pht analogs **4(a-e)** on human RBCs. Hemolytic effect was checked at 0.5, 1, 5, 10, 20 μM with a 10% (v/v) RBCs suspension after 1 h. Absorbance, taken at 415 nm, indicates no significant lysis occurred in case of the Pht analogs up to 5 μM. Experiments were repeated three times each in triplicate and data are expressed as mean values ± SD.

steady state (*i.e.*, at equilibrium; denoted as R$_{eq}$) and concentrations of the compounds (data not shown). SPR analysis indicated that Pht analog **4b** interacts with *Pf*αI-tubulin, suggestive of a tendency to disrupt tubulin dynamics in the parasite. To verify this inference, the compounds were further examined for detection of binding events with recombinant *Pf*αI-tubulin *in vitro* by Thermal Shift Assay (TSA).

To further validate our SPR-based interaction analysis and confirm that the anti-plasmodial activity of the Pht analogs (n = 3) is conferred by their interaction with *Pf*αI-tubulin, TSA was done for binding analysis

between the recombinant protein and Pht analogs, as mentioned in material and methods section. In the chosen temperature range of 4 °C–80 °C, *Pf*αI-tubulin treated individually with all three Pht analogs could be detected in solution at all tested temperature points, while the protein precipitated at temperatures over 60 °C when omitting the compound (DMSO only control). This significant ligand-dependent thermo-stabilization of *Pf*αI-tubulin as compared to control is consistent with our SPR-based findings (Fig. 7b).
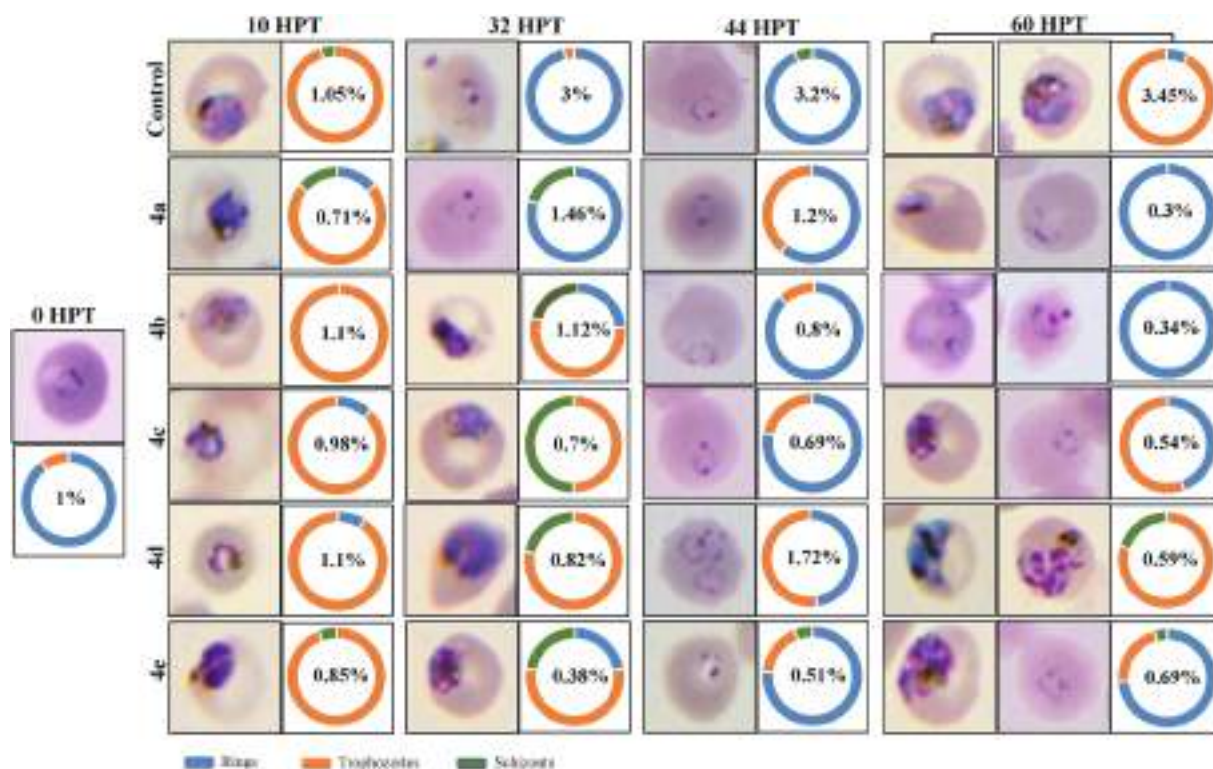
Fig. 4. Light microscopic analysis of different blood stages of *Pf*3D7 after treatment with Pht analogs. Progression of the growth cycle (from ring to trophozoite stage) was analyzed by Giemsa staining at 10, 32, 44 and 60 hpt.

2.5. 4b interacts with PfαI tubulin via hydrophobic and H-bonds

Owing to the high sequence similarity between tubulin orthologs from *Pf*3D7 strain and *Bos taurrus*, X-Ray diffraction based structural model of *Bt*α-β tubulin heterodimer was used as a template to generate three-dimensional co-ordinates of *Pf*αfdβ tubulin by homology modeling, and thus, inter-monomeric H-bond interactions were elucidated (Fig. 8A). After optimal rigid-body superimposition of *Bt*αtgβ tubulin with the generated structural model of *Pf*αfiβ tubulin, overall, Root-Mean-Square Deviation (RMSD) value of the C-alpha atomic co-ordinates was found to be 1.88 Å, suggesting a reliable 3D structural model of *Pf*αfrβ tubulin (Fig. 8A). Assessment of stereochemical quality and accuracy of the generated structural model displayed 88.9% of amino acid residues lying in the most favored (*core*) regions, with 10.5%, 0.4%, and 0.1% residues in *additional allowed*, *generously allowed* and *disallowed regions* of Ramachandran plot, respectively, indicating that the backbone dihedral angles: ϕ and Ψ of the generated structural model of *Pf*αfrβ tubulin were reasonably accurate. RMSD value and Ramachandran plot characteristics confirmed reliability of the homology-based structural model of *Pf*αI/β tubulin to be taken further for *in silico* interaction analysis.

To evaluate a possible mode of interaction of the Pht analogs **4a**, **4b** and **4d** with *Pf*αI tubulin, *in silico* interaction analysis was performed, as described in the material and methods section. *Despite the high structural similarity* among the Pht analogs, as evaluated by structural superimposition using BIOVIA Discovery Studio Visualizer v20.1.0.19295 (Fig. 8B), significant differences in their interaction behavior with *Pf*αI tubulin were observed (Fig. 8D and E), consistent with our SPR and TSA-based *in vitro* interaction analysis. **4a** and **4b** were found to fit into the overlapping binding pockets of *Pf*αI tubulin located at the interface of *Pf*αI/β monomers and interact via hydrophobic (predominantly) and polar contacts (H-bonds) with amino acid residues of the protein (Fig. 8D and E). Presence of the '4-trifluoromethylphenyl' moiety allowed **4b** a reasonably better fit into the *Pf*αI tubulin binding pocket, with

lower free binding energy (-10.7 kCal/mol) as compared to **4a** (-9.6 kCal/mol). **4b** was found to form H-bond interaction with Asn-206 (bond length: 2.88 Å) of *Pf*αI tubulin. Concomitantly, presence of the '*4-fluorophenyl*' moiety rendered **4d** completely inert to show any interaction with *Pf*αI tubulin.

2.6. Antiparasitic efficacy in a murine model of Plasmodium berghei infection

Pht analogs **4(a-e)** possessing purity above 97% were evaluated for their *in vivo* antiplasmodial activity. Compounds were administered intra-peritoneally to BALB/c mice infected with *Plasmodium berghei (Pb)* ANKA at a daily dose of 30 mg/kg for seven days. A considerable decrease in parasitemia (Fig. 9A) and mortality rate (Fig. 9B) was observed in treated mice over the untreated controls after seven and 15 days of infection, respectively. Among the five compounds, **4(a-b,e)** showed a decrease in the parasite load to 3.6%, 2.1% and 3.9%, respectively as compared to 36.5% observed for the untreated control group on day 7 post infection. A lower mortality rate was observed for mice treated with **4(a-b,e)** with a mean survival time (MST) of 11.07, 11.42 and 10.47 days, respectively as compared to control with a MST of 8 days. Notably, the low toxicity observed in the test groups during experiments was also encouraging.

Next, the predicted ADME (absorption, distribution, metabolism, excretion) profile of **4(a-e)** was calculated using the SwissADME Data predictor Table 1 (supplementary information) [68]. All of the analogs showed tolerable pharmacological features, including good adherence to Lipinski rules [69].

2.7. Structure-activity relationship (SAR) analysis

Five Pht analogs, **4(a–e)**, with IC$_{50}$ values below 2.3 μM for the *Pf*3D7 strain have been described. In addition, these compounds inhibited the growth of the RKL-2 strain with IC$_{50}$ values below 4 μM.
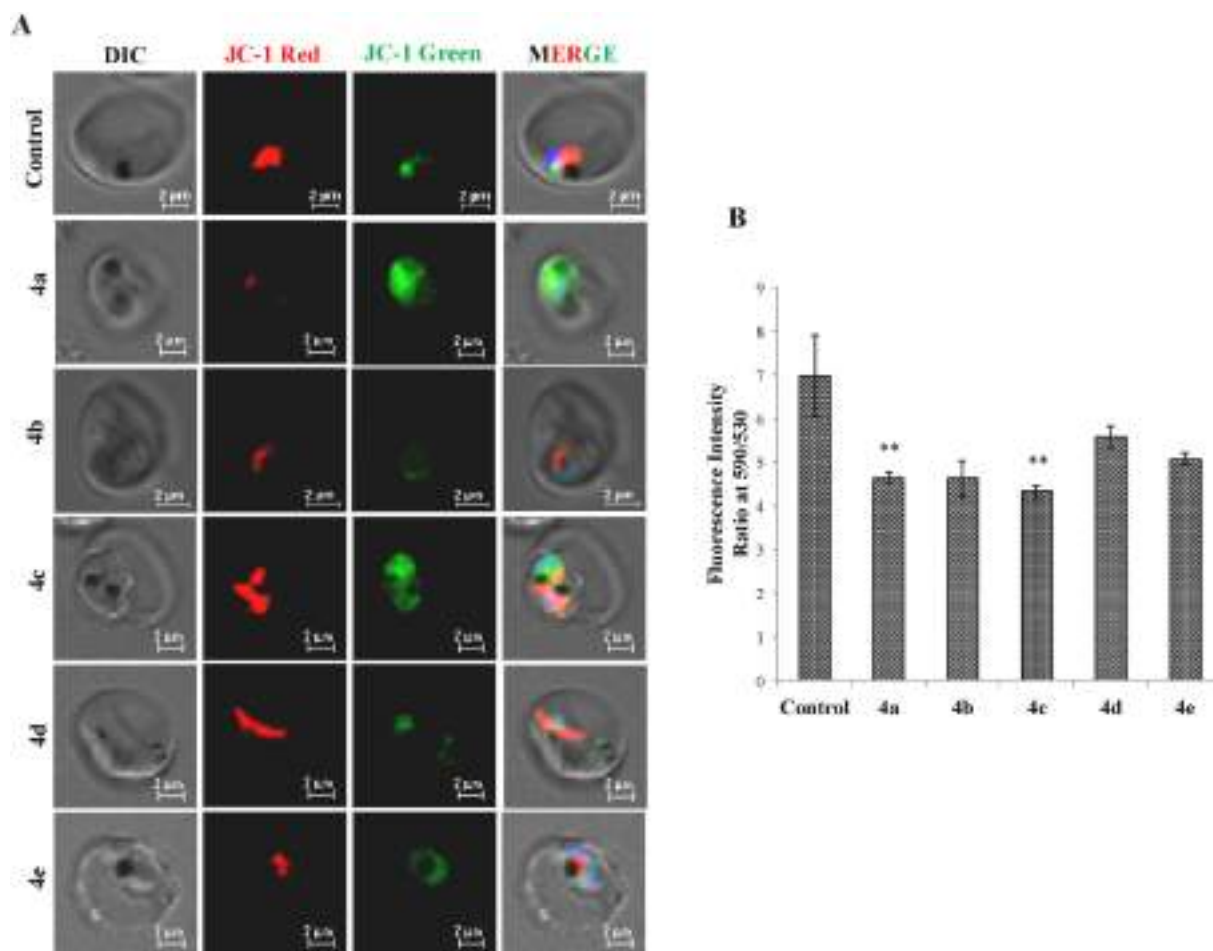
Fig. 5. (A) Fluorescence images of parasites displaying monomeric JC-1 (green) in the cytoplasm and JC-1 aggregates (red) in mitochondria. The first row (control) exhibits untreated parasites with bright red signal at 590 nm indicating a functional mitochondrion. Subsequent rows exhibit the effects of the Pht analogs **4(a-e)** with bright green and faint red signals. **(B)** The fluorometric ratio of JC-1 (aggregates)/JC-1 (monomeric) in the parasite population after treatment with Pht analogs *vs.* untreated control.

The SAR is mainly centred on the different substitutions on the triazole ring and amino acids. Phts analogs possess higher potency *viz.* **4a** (IC_{50} = 0.74 μM); **4b** (IC_{50} = 0.64 μM); and **4c** (IC_{50} = 0.81 μM) when the linker (R_1; Scheme 1) is a bulky group such as isobutyl or *sec*-butyl group. When the linker is an isopropyl group, the potency is slightly decreased, as in case of **4e** (IC_{50} = 2.3 μM) (Fig. 10).

Analogs possessing a butyl group and 4-fluorophenyl ring (**4f**) on the triazole moiety, displayed higher potency at 1 μM (% inhibition, 0.33; Table 1) over the analog, **4g** with 4-methyl phenyl group on the triazole (% inhibition, −8.68) at the same concentration. However, at 10 μM, the percentage inhibition of **4f** increased from 0.33% to 45%. Similarly, the percentage inhibition for **4g** was increased to 69% at 10 μM concentration (Table 1). As demonstrated by **4m** and **4o**, which possess an isobutyl linker and a fluorophenyl group on the triazole, varying the R group on the Pht does not seem to alter activity. Analogs with an unsubstituted benzyl ring on the triazole (**4c**) and an isobutyl linker also exhibited anti-plasmodial activity. The greatest activity was noted for analogs possessing a fluoro-substituted phenyl ring on the triazole moiety, and a *n*-butyl or isobutyl linker (**4b** and **4d**), probably due to the high electronegativity and/or increased lipophilicity of the fluorine substituents. Similarly, we observed that variation of R_2 groups from 2-fluorophenyl (**4o**) to pentafluorophenyl (**4p**) did not alter the % inhibition at 10 μM. Also, moderate and similar activity was observed when position of fluorine in R_2 groups changes from -*ortho* to –*para* (*i.e.*, **4q** and **4r**) (Fig. 10). As expected, CQ displayed significant potency even in its nanomolar concentration, and the IC_{50} value was reported to be 29 nM.

3. Conclusion

Hybrid molecules that utilize new chemical entities with a variety of pharmacophores, represent a rational approach for the development of novel therapeutics. As a follow up to our earlier work in the design of Pht analogs as antimalarials, we synthesized additional derivatives and evaluated their effect on *Pf in vitro* [15,17,70,71]. Structural modifications around the Pht pharmacophore showed that the replacement of fluorine on the triazole ring with other groups improved antiparasitic activity. In drug like molecules, the introduction of trifluoromethyl has become a popular lipophilic group that can improve affinity to target enzymes and exert significant changes on neighboring groups [14,18, 72]. Pht analogs **4(a-e)** produced growth defects, specifically, inhibiting parasite egress from or invasion of the blood cell. At their respective IC_{50} concentrations, the Pht analogs induced depolarization of the mitochondrial membrane potential leading to cell death. *In vitro*, the Pht analogs and ART act synergistically, and thus represent a promising starting point for combination therapy. Biophysical and biochemical analyses, in order to test the hypothesis that plasmodial growth inhibition by Pht analogs is mediated by their interaction with *Pf*tubulin isoforms, revealed that one of the Pht analog, **4b** interacts with *Pf*αI-tubulin, indicating the possibility of the compound disrupting tubulin dynamics in the parasite. Finally, the Pht analogs **4(a-e)** demonstrated robust antiparasitic activity in a murine model of P.
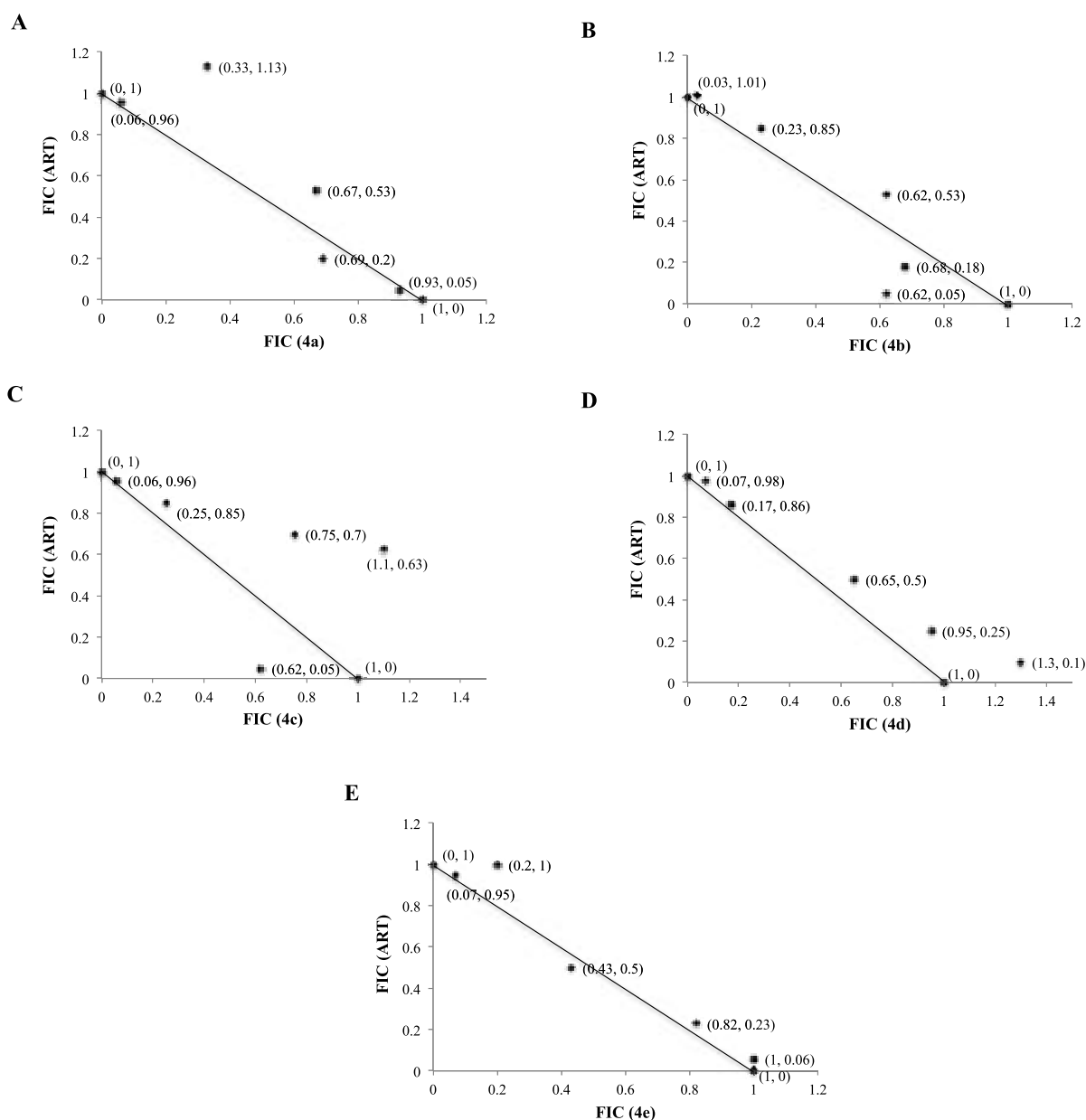
Fig. 6. *In vitro* combination assay showing the effect of Pht analogs and ART in alone as well as in combination against *Pf* 3D7. Isobologram graphs represents the interaction between Pht analogs and ART displaying the mean FIC of ART on (Y-axis) along with mean FIC of Pht analogs **4(a-e)** (X-axis), respectively. ΣFIC <1 represent synergism, ΣFIC ≥1 and <2 represent additive effect, ΣFIC ≥2 and <4 represent slight antagonism, ΣFIC ≥4 represent marked antagonism. Experiments were carried out in duplicate.

berghei infection, thereby providing the formal proof-of-concept to support the continued investigation of these analogs as antimalarials.

3.1. Material and methods

Chemistry. Solvents and reagents were purchased from commercial sources and used without purification for the experiments. Homogeneity/purity of all the products was assayed by thin-layer chromatography (TLC) on alumina-coated plates (Merck). Product samples in chloroform ($CHCl_3$) were loaded on TLC plates and developed in Ethyl acetate/Petroleum ether (1:1, v/v). When slight impurities were detected by UV light visualization, compounds were further purified by column chromatography on silica gel (100–200 mesh size, CDH). Melting points were determined on Melting point machine M − 560 (Buchi). ^1H and ^{13}C nuclear magnetic resonance (NMR) spectra were recorded in $CDCl_3$,

DMSO medium on a JEOL ECX-400P NMR at 400 MHz and 100 MHz, respectively at USIC, University of Delhi, using TMS as an internal standard. Chemical shifts are expressed in ppm (δ-scale) and coupling constants (*J*) in Hz. Splitting patterns are described as singlet (s), doublet (d), doublet of doublet (dd), triplet (t), quartet (q) and multiplet (m). The high-resolution mass spectral data was obtained using an Agilent Technology-6530, Accurate mass, Q-TOF LCMS spectrometer at USIC, University of Delhi. All the listed Pht analogs were prepared following literature procedures [14]. The purity of Phts analogs **4(a-e)** was assessed on HPLC system (Gilson, USA) with an analytical column (C18) and a Thermo Separation Spectra SERIES UV100 detector coupled with software. The mobile phase for the analysis was prepared from acetonitrile and water (v/v) and compounds showed purity >97%. The spectroscopic data for the new analogs **4(a-e)** is provided, however the composition of others, **4(f-r)** was confirmed by their melting points. The
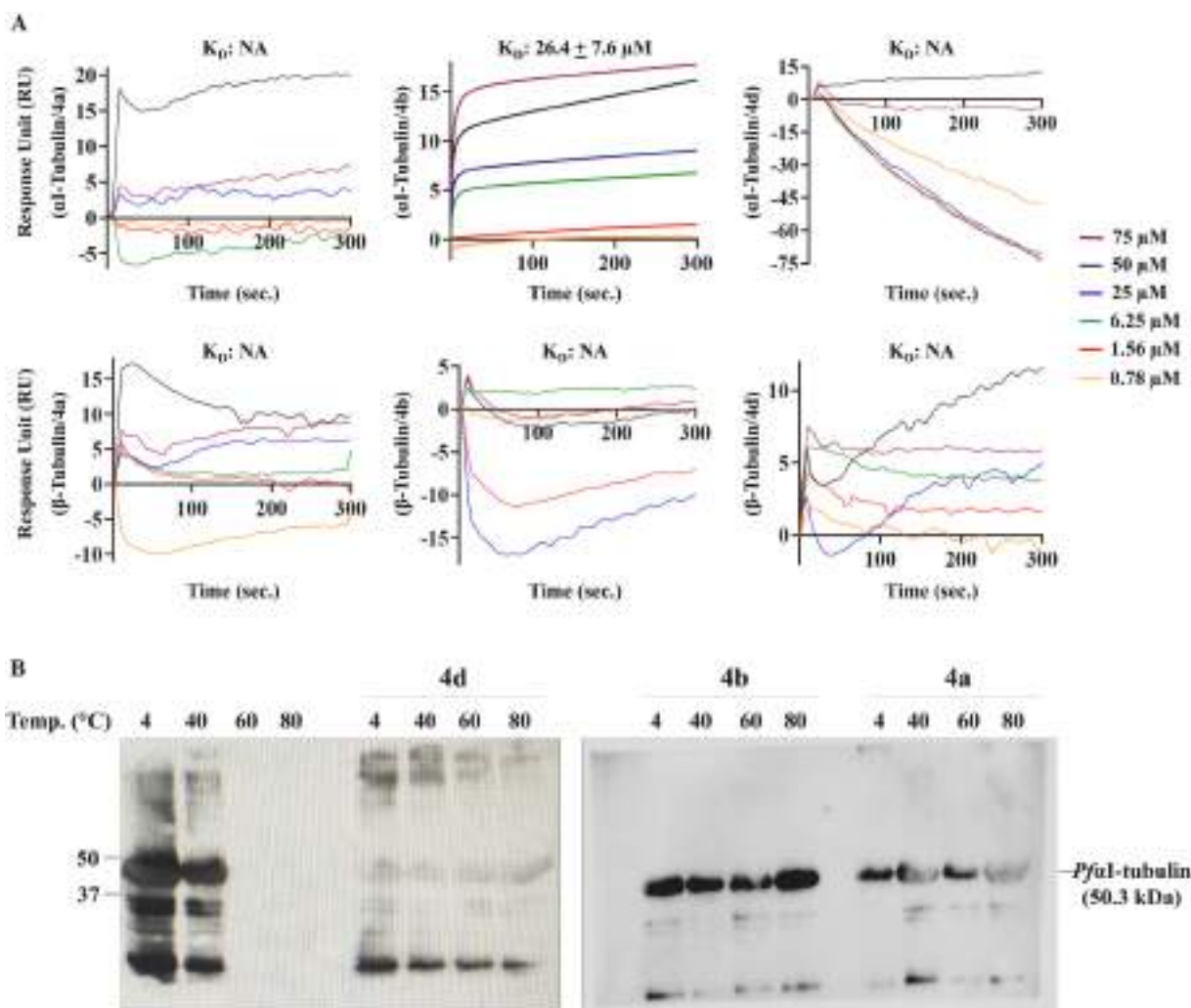
Fig. 7. Pht analogs interact with *Pf*αI-tubulin *in vitro*. **(A)** Concentration dependent real-time sensograms for SPR based biomolecular interaction analysis of *Pf*tubulin isoforms (αI and β) and Pht analogs (n = 3). Pht analog, **4b** showed binding affinity for recombinant *Pf*αI-tubulin, with K$_D$ of 26.4 ± 7.6 μM. However, no such interaction was observed either for *Pf*αI-tubulin/(**4a** & **4d**) or for *Pf*β-tubulin/(**4a**, **4b** & **4d**). **(B)** SPR-based *Pf*αI-tubulin/(Pht analogs) interaction was further confirmed with TSA. Representative immunoblots showing thermo-stabilization of *Pf*αI-tubulin in the presence of Pht analogs.

spectra for **4(a-e)** are provided in the supporting information (Figs. S1–S14).

3.2. Spectroscopic data

2-(1-(1-(((1-(4-Chlorophenyl)-1*H*-1,2,3-triazol-4-yl)methyl)-1H-benzo[d]imidazole-2-yl)-3-methylbutyl)-5-methylisoindoline-1,3-dione (4a): White solid; mp 100–102 °C; Yield: 73%. ^{1}H NMR (400 MHz, CDCl$_3$): δ 7.88 (d, *J* = 7.4 Hz, 1H), 7.44 (d, *J* = 7.5 Hz, 1H), 7.34 (d, *J* = 8.6 Hz, 2H), 7.25–7.27 (m, 7H), 7.13 (s, 1H), 5.76 (dd, *J* = 10.7, 4.1 Hz, 1H), 5.47 (s, 2H), 2.84–2.77 (m, 1H), 2.37–2.6 (m, 1H), 2.25 (s, 3H), 1.59–1.56 (m, 1H), 1.03 (d, *J* = 6.4 Hz, 3H), 0.96 (d, *J* = 6.6 Hz, 3H); ^{13}C NMR (100 MHz, CDCl$_3$): δ 167.63, 167.51, 151.26, 145.49, 144.43, 142.32, 135.45, 134.79, 134.65, 134.49, 131.23, 130.00, 129.72, 129.44, 128.29, 123.94, 123.69, 123.65, 123.27, 123.00, 122.75, 121.27, 121.00, 120.74, 118.79, 109.16, 45.19, 39.83, 38.81, 24.84, 23.46, 21.90, 21.73, 17.79.

2-(2-Methyl-1-(1-(((1-(4-(trifluoromethyl)phenyl)-1*H*-1,2,3-tri-azol-4-yl)methyl)-1*H*-benzo[d]imidazole-2-yl)butyl)isoindoline-1,3-dione(4b): White solid; mp 196–198 °C; Yield: 64%; HRMS *m/z* calcd. (M + H)$^+$ 558.5537, found 559.2069; ^{1}H NMR (400 MHz, CDCl$_3$): δ 7.89 (d, *J* = 7.4 Hz, 1H), 7.71–7.60 (m, 4H), 7.57–7.49 (m, 4H), 7.38 (s, 1H), 7.34 (d, *J* = 7.4 Hz, 1H), 7.31–7.22 (m, 2H), 5.69–5.51 (m, 2H), 5.40 (dd, *J* = 10.4, 7.7 Hz, 1H), 3.42–3.37 (m, 1H), 1.61 (d, *J* = 81.3 Hz,

1H), 1.25–1.08 (m, 3H), 0.98–0.91 (m, 4H). ^{13}C NMR (100 MHz, CDCl$_3$): δ 167.62, 167.56, 150.35, 150.21, 144.61, 144.56, 142.55, 138.80, 134.99, 134.84, 134.15, 131.08, 126.96, 123.52, 123.35, 122.72, 122.68, 120.74, 120.11, 119.43, 109.60, 51.94, 51.49, 39.38, 34.57, 34.07, 27.18, 25.42, 17.16, 15.39, 11.15, 10.70.

2-(1-(1-(((1-Benzyl-1*H*-1,2,3-triazol-4-yl)methyl)-1*H*-benzo[d]imidazole-2-yl)-2-methylbutyl)isoindoline-1,3-dione(4c): White solid; mp 76–78 °C; Yield: 79%; HRMS *m/z* calcd. (M + H)$^+$ 504.5823, found 505.2353; ^{1}H NMR (400 MHz, CDCl$_3$): δ 7.80 (d, *J* = 7.3 Hz, 1H), 7.72–7.65 (m, 2H), 7.65–7.59 (m, 2H), 7.29 (d, *J* = 6.5 Hz, 1H), 7.25 (s, 3H), 7.17 (t, *J* = 6.0 Hz, 2H), 7.12 (s, 1H), 7.05 (d, *J* = 4.3 Hz, 2H), 5.58 (dd, *J* = 22.6, 16.6 Hz, 1H), 5.45–5.29 (m, 2H), 5.19 (q, *J* = 14.9 Hz, 2H), 3.49–3.31 (m, 1H), 1.52–1.38 (m, 1H), 1.15–0.96 (m, 1H), 0.95–0.77 (m, 6H); ^{13}C NMR (100 MHz, CDCl$_3$): δ 167.74, 150.52, 150.31, 143.58, 143.50, 142.51, 134.83, 134.70, 134.36, 134.25, 131.36, 129.09, 128.76, 127.92, 123.45, 123.30, 122.50, 121.71, 120.55, 109.94, 54.02, 51.84, 51.64, 39.27, 34.47, 33.91, 26.95, 25.46, 16.83, 15.47, 11.16, 10.62.

2-(1-(1-(((1-(4-Fluorophenyl)-1*H*-1,2,3-triazol-4-yl)methyl)-1*H*-benzo[d]imidazole-2-yl)-2-methylbutyl)-5-methylisoindoline-1,3-dione (4d): Green solid; mp 109–111 °C; Yield:45%; HRMS *m/z* calcd. (M + H)$^+$ 523.5728, found 523.2248; ^{1}H NMR (400 MHz, CDCl$_3$): δ 7.80 (s, *J* = 7.3 Hz, 1H), 7.72–7.65 (m, 1H), 7.65–7.59 (m, 1H), 7.40 (s, 1H),
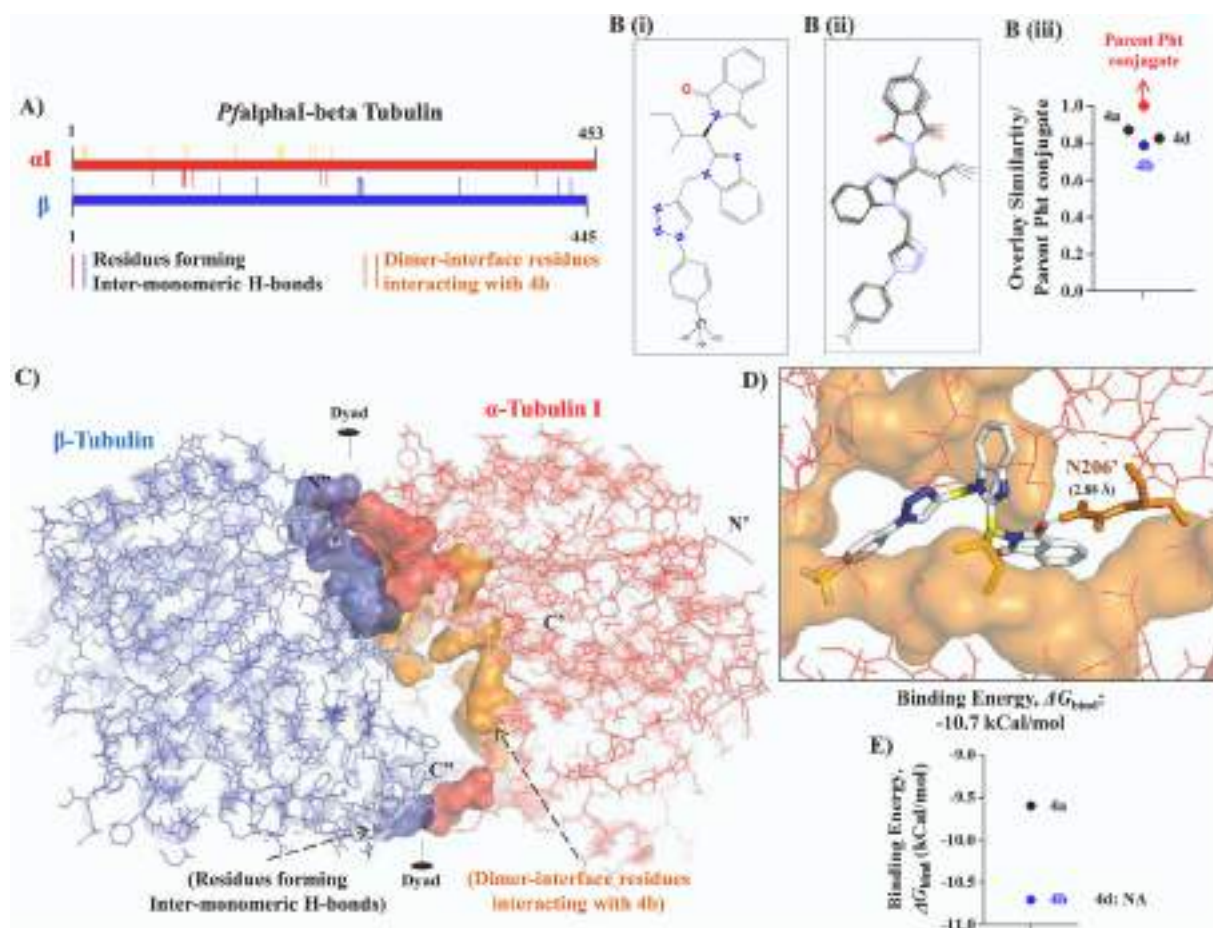
Fig. 8. Homology modeling based structural model of *Pf*αI-β tubulin and *in silico* interaction analysis with Pht analogs. **(A)** X-Ray diffraction-based crystal structure of *Bt*α-β tubulin (PDB ID: 1JFF) was used as template to generate homology modeling based structural *model* of *Pf*αI-β tubulin. Optimal rigid-body superimposition of both the proteins revealed RMSD value of 1.88 Å, suggesting that the generated homology model of *Pf*αI-β tubulin is reliable. **(B)** 2D-structure of **4b** (i), structural superimposition of the Pht analogs **(ii)** and overlay similarity **(iii)**, as analyzed using BIOVIA Discovery studio Visualizer, are shown. **(C)** Amino acid residues of *Pf*αI- & β-tubulin involved in inter-monomeric H-bond interactions, and those involved in interaction with **4b** are shown. **(D)** Schematic representation of complex formation between the binding pocket of *Pf*αI tubulin localized at the interface of *Pf*αI/β monomers and **4b**. **(E)** Presence of '4-trifluoromethylphenyl' moiety in **4b** allowed the Pht analog to fit reasonably better into the *Pf*αI tubulin binding pocket, with lower free binding energy (−10.7 kCal/mol) as compared to **4a** (−9.6 kCal/mol). Presence of '4-fluorophenyl' moiety rendered **4d** completely inert to show any interaction with *Pf*αI tubulin. 3D visualization of protein structure and interactions analysis was rendered with PyMOL Molecular Graphics System, Version 1.7.4.5 Schrödinger, LLC.
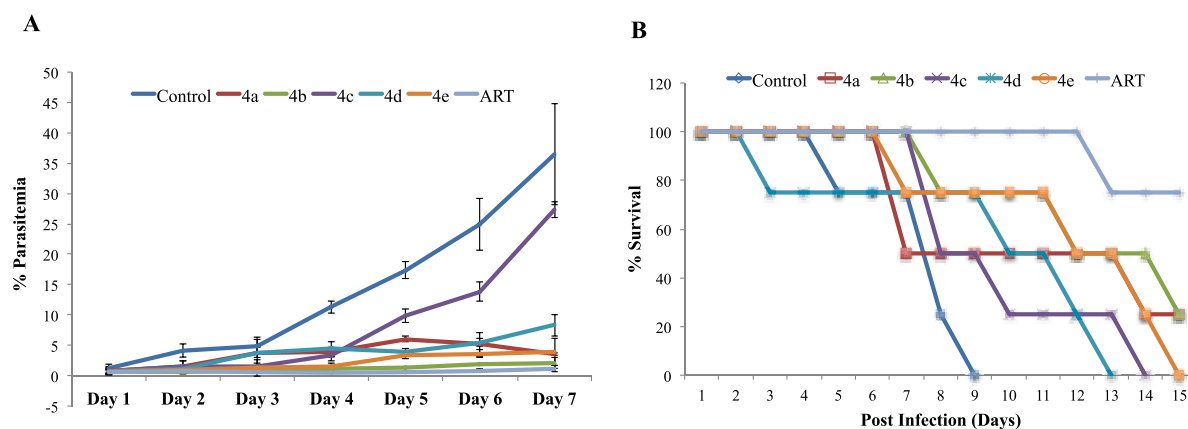
Fig. 9. Efficacy of Pht analogs **4(a-e)** in *Pb* ANKA infected Balb/c mice. Untreated mice were used as negative control. Pht analogs were administered intraperitoneally at 30 mg/kg; n = 4) for seven consecutive days. A) Percent parasitemia was calculated by Giemsa-stained thin blood smears from day 1 to day 7 post infection; B) Percent survival was calculated up to 15 days post infection.
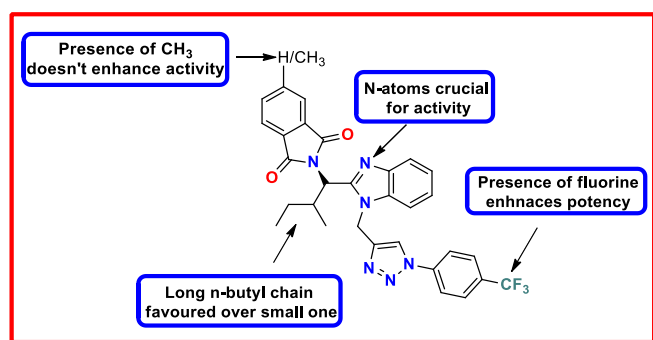
Fig. 10. SAR for the antiplasmodial activity of **4(a-e)**.

7.34 (s, 3H), 7.25 (s, 3H), 7.08 (t, $J = 7.9$ Hz, 2H), 5.75–5.47 (m, 2H), 5.40 (dd, $J = 9.5$, 5.4 Hz, 1H), 3.45 (dd, $J = 13.3$, 6.5 Hz, 1H), 2.48 (s, 1H), 2.35 (d, $J = 25.5$ Hz, 3H), 1.72–1.43 (m, 1H), 1.02–0.78 (m, 6H); ^{13}C NMR (100 MHz, CDCl$_3$): δ 168.74, 167.66, 163.64, 161.16, 150.42, 145.63, 142.35, 135.20, 134.77, 132.91, 131.46, 128.51, 124.39, 123.95, 123.76, 123.47, 122.84, 122.13 (d, $J = 7.7$ Hz), 120.74, 116.74, 116.51, 109.81, 51.54, 39.68, 34.06, 27.16, 25.46, 21.97, 17.16, 15.43, 11.17, 10.69.

2-(2-Methyl-1-(1-((1-(4-(trifluoromethyl)phenyl)-1H-1,2,3-triazol-4-yl)methyl)-1H-benzo[d]imidazol-2-yl)propyl)isoindoline-1,3-dione(4e): White solid; mp 202–204 °C; Yield, 69%; HRMS *m/z* calcd. $(M + H)^+$ 545.5271, found 545.1918; ^{1}H NMR (400 MHz, CDCl$_3$): δ 7.90 (d, $J = 7.5$ Hz, 1H), 7.69–7.58 (m, 4H), 7.53–7.48 (m, 4H), 7.33 (d, $J = 7.3$ Hz, 2H), 7.30–7.22 (m, 2H), 5.58 (q, $J = 37.4$, 17.1 Hz, 2H), 5.31 (d, $J = 10.6$ Hz, 1H), 3.62–3.51 (m, 1H), 1.17 (d, $J = 6.4$ Hz, 3H), 1.00 (d, $J = 6.7$ Hz, 3H); ^{13}C NMR (100 MHz, CDCl$_3$): δ 167.52, 150.07, 144.70, 142.55, 138.74, 134.89, 134.14, 131.00, 126.95 (d, $J = 3.4$ Hz), 126.94, 123.62, 123.36, 122.78, 120.87, 120.09, 119.19, 109.44, 67.15, 53.06, 39.49, 28.57, 21.24, 19.39.

3.3. Hemolytic activity

Hemolysis assay was performed as described previously [73]. In brief, RBCs suspension 10% (v/v) washed with $1 \times$ PBS (pH 7.4) and resuspended in $1 \times$ PBS. Suspension was treated with Pht analogs at different concentrations for 2 h at 37 °C. Samples were centrifuged at $8000 \times g$ for 5 min at Room Temperature (RT, 298 K). Supernatant were taken for absorbance at 415 nm to obtained percentage of RBCs lysis. Triton X-100 with 1% (v/v) was used as a positive control. Percentage of RBCs lysis was obtained by using following formula:

$$\% \text{ RBCs lysis} = (OD_{415nm} \text{ sample} - OD_{415nm} \text{ PBS}) / (OD_{415nm} \text{ Triton X-100 } 1\% - OD_{415nm} \text{ PBS})$$

3.4. Parasite culture

All of the synthesized Pht analogs were screened for *in vitro* anti-malarial activity against CQ-sensitive strain (*Pf*3D7, Malaria Research and Reference Reagent Resource Center, MR4) and CQ-resistant strain (*Pf*RKL-9, Rourkela, Odisha, India). The antiplasmodial activity screening was performed by counting on Giemsa-stained smears. *Pf*3D7 and RKL-9 were cultured as described by the reported methods [74]. Culture media used for parasite culture supplemented with complete RPMI 1640, 0.2% NaHCO$_3$, 0.5% AlbuMax I, 0.1 mM hypoxanthine, 25 mg ml^{-1} gentamicin at 37 °C in human O$^+$ RBCs and maintained in mixed gas environment (5% O$_2$, 5% CO$_2$ and 90% N$_2$). Geimsa staining of thin blood smears routinely monitored parasites. Parasites were synchronized at ring stage by 5% D-sorbitol.

3.5. SYBR green I based fluorescence assay

Growth of one intraerythrocytic cycle of *Pf* was monitored to check the percent growth inhibition [19,20]. Parasites were treated with **4 (a–e)** whereas untreated parasites were considered as control. To calculate percent growth inhibition, SYBR Green assay and Giemsa staining methods were used. The IC$_{50}$ of the Pht analogs **4(a-e)** were determined with the help of Graph Pad Prism 8 software. Synchronized late trophozoite parasites (36–40 h) were treated with different concentrations of Pht analogs **4(a–e)** to calculate IC$_{50}$ values. SYBR green I based fluorescence assay was performed to check the inhibitory effect of Pht analogs at different concentrations against *Pf*3D7 and *Pf*RKL-9 strains [75]. Parasites were initially taken at 1% parasitemia with 2% hemotocrit and incubated with different concentrations of Pht analogs ranging from 1 μM to 10 μM, whereas DMSO was used as a control. Samples were seeded in 96 well microtiter plates and incubated at 37 °C for one cycle of parasite growth. Using Giemsa stain did morphological analysis. Spectrofluorometric analysis was done to determine the percent growth inhibition by SYBR green dye assay. The fluorescence intensity was observed at 485 nm excitation and 530 nm emission spectrum. Percent growth inhibition was calculated as follows: % Inhibition = [1 - % Parasitemia (Treatment)/% Parasitemia (Control)] *100. Data were expressed as mean ± SD.

3.6. Progression assay

To estimate the blood stage specific effect of Pht analogs on *Pf*3D7, progression assay was performed [76]. Briefly, synchronized ring stage parasites (0.8% parasitemia and 2% hematocrit) were treated with Pht analogs **4(a-e)** at IC$_{50}$ concentration in a complete RPMI-1640 medium and seeded in 96-well flat bottom microtiter plates respectively. Parasite culture was incubated and monitored up to 72h at 37 °C. Morphological analysis was performed by counting Giemsa-stained slides in duplicate with the help of light microscope (Olympus).

3.7. Mitochondrial membrane potential

Mitochondrial membrane potential is an indicator of mitochondria's functional status. Alteration in mitochondrial membrane potential leading to mitochondrial dysfunction causes cell death [24,77–79]. Mitochondrial dysfunction was observed by using membrane permeant JC-1 dye. JC-1 is a cationic probe, due to electronegative environment inside the functionally active mitochondria with high $\Delta\psi$m, it aggregates in energized mitochondria and gives red color fluorescence at 590 nm but in case of low $\Delta\psi$m (depolarized state) JC-1 remain in monomeric form and gives green color fluorescence at 530-10 nm. Mitochondrial membrane potential was determined by using method described previously [24]. In brief, trophozoite stage parasites (10–12% parasitemia) were treated with IC$_{50}$ concentration of Pht analogs for 3h at 37 °C in the CO$_2$ incubator. Samples were washed with 1xPBS by centrifugation at $500 \times g$ for 2 min at RT and resuspended again in 1xPBS. Freshly prepared JC-1 dye with working concentration of 5 μg/ml was added to each sample and incubated for 30 min at 37 °C in a CO$_2$ incubator. Cells were washed twice with 1xPBS and resuspended again in 1xPBS. Mitochondrial membrane potential was calculated with the help of spectrofluorometry by observing fluorescence intensities from the parasite lysate at wavelength of excitation (520 nm) and emission (590 nm) respectively. *In vivo* cell imaging was performed using Olympus fluoview3000 confocal microscopy. Live cell imaging was observed under a 100X objective (oil immersion) and band pass filter at 355–460 nm. Experiments were repeated thrice and only representative figures are shown.

3.8. Combination study

Among the several factors affecting malaria eradication, drug

resistance is one of the resistors of malaria control system. Resistance of artemisinin towards *Pf* strains leads to development of novel synthetic drugs and ART combination therapy (ACTs) [80–82]. The rationale behind the combination study to obtain the drug interaction pattern between Pht analogs and ART as compared to the sum of individual drugs. The *in-vitro* combination study was used to check the effect of **4 (a–e)** Pht analogs along with ART, as described earlier [83]. For testing combination of ART and Pht analogs against *Pf*3D7 0.5% parasitemia of synchronized ring stage parasites with 2% hematocrit were seeded in a 96 well plate. Parasites were treated with Pht analogs and artemisinin in the range of $1/4xIC_{50}$ to $4xIC_{50}$ concentrations alone as well as in combination whereas untreated culture was used as negative control according to fixed ratio method. Samples were seeded in flat-bottom sterile 96 well microtitre tissue culture plates. Plates were incubated in incubator at 37 °C and 5% CO_2, 90% N_2 and 5% O_2 for 72 h. Parasitemia with respect to untreated control was determined by using flow cytometry and Giemsa staining. Experiments were done in duplicate.

3.9. SPR analysis of binding affinity between Pht analogs and Pf-tubulins

Cloning, over-expression and purification of *Pf*αI- and *Pf*β-tubulins (PlasmoDB IDs: PF3D7_0903700 and PF3D7_1008700, respectively) was done, as described previously by our group [84]. To determine binding strength of the Pht derivatives (n = 3) with potent anti-plasmodial activity *in vitro*, real-time biomolecular interaction analysis was carried out with SPR at physiologically relevant concentrations, by using AutoLab Esprit SPR (at Advanced Instrumentation Research Facility, Jawaharlal Nehru University, New Delhi, India), and K_D value was determined at RT. SPR analysis was performed by following previously described protocols [85,86]. Briefly, all three Pht analogs were injected individually at different concentrations: 75, 50, 25, 6.25, 1.56 and 0.78 μM over the *Pf*αI-tubulin (5.1 ng per mm^2) and *Pf*β-tubulin (2.6 ng per mm^2) immobilized SPR sensor chip surfaces with association and dissociation time of 300 s and 200 s, respectively, followed by comparing their respective binding affinities at RT. A control flow cell was activated and blocked in a similar manner with injection of equivalent concentrations of DMSO to allow for reference subtraction. HEPES-NaCl buffer was used both as immobilization and binding solutions. The sensor chip surface was regenerated with 50 mM NaOH. Data were fit to the two-state conformational change model using AutoLab SPR Kinetic Evaluation software provided with the instrument. K_D values were calculated using the Integrated Rate Law (IRL) equation.

3.10. TSA for interaction analysis of Pht analogs and PfTubulins

Thermostability of *Pf*αI-tubulin was monitored, *in vitro*, for the detection of binding events between *Pf*αI-tubulin and the Pht derivatives (n = 3) with potent anti-plasmodial activity, by essentially following a protocol described earlier [86,87]. Briefly, 20 μg of the recombinant *Pf*αI-tubulin, per reaction, was individually incubated with all three Pht derivatives at concentrations corresponding to their anti-plasmodial IC_{50} values, in HEPES-NaCl buffer, pH 7.2. Protein in control reactions was incubated with an equivalent volume of DMSO. Following the incubations, reaction mixtures were heated on C1000 Touch™ Thermal Cycler (Bio-Rad) at different temperatures ranging from 4 °C to 80 °C for 3 min, and then cooled down to RT for 5 min. Following centrifugation at 10,000 rpm for 45 min at 4 °C, SDS–PAGE of supernatants was performed. Anti-*Pf*αI-tubulin antibody (raised in rabbit) diluted at 1:1000 in 1% Bovine Serum Albumin (BSA; prepared in PBST) was used to probe *Pf*αI-tubulin. Blot was developed with Clarity Western ECL system (Bio-Rad), and the image was generated & analyzed with ChemiDoc™ Imaging System (Bio-Rad).

3.11. PfαI-β tubulin architecture and in silico interaction analysis with Pht analogs

Comparative or homology modeling was employed to model 3D structure of *Pf*αI-β tubulin heterodimer, by following the protocol as described previously by our group [86,88]. To accomplish this, amino acid sequences of *Pf*αI- and *Pf*β-tubulins (PlasmoDB IDs: PF3D7_0903700 and PF3D7_1008700, respectively) were retrieved from PlasmoDB database [89]. To search for a suitable template for homology modeling, BLASTp search was performed using amino acid sequences of *Pf*αI- and *Pf*β-tubulins as query sequences, against Protein Data Bank (PDB) database [90,91]. Amino acid sequence identities among tubulin orthologs from *Pf* strain 3D7 and *Bos taurrus* were found to be 84.1% (α-tubulin) and 88.8% (β-tubulin), thus rendering X-Ray diffraction based structural model of *Bt*α-β tubulin heterodimer (PDB ID: 1JFF; resolution: 3.5 Å) as a suitable template to model 3D structure of *Pf*αI-β tubulin [92]. Homology modeling was done by using Modeler v9.17 software [93]. Generated model was further subjected to structural refinement by using ModRefiner [94]. Reliability of the refined structural model of *Pf*αI-β tubulin was assessed by examining backbone dihedral angles: phi (Ø) and psi (Ψ) of the amino acid residues lying in the energetically favorable regions of Ramachandran space [95]. This was done by using PROCHECK v.3.5 [96]. Percent quality assessment of the protein structure was evaluated by utilizing four sorts of occupancies: core, additionally allowed, generously allowed and disallowed regions. The refined 3D structural model of *Pf*αI-β Tubulin heterodimer, thus generated, was subsequently used for *in silico* interaction analysis with Pht analogs: **4a**, **4b** and **4d**.

Structural superimposition of the Pht analogs was done by using BIOVIA Discovery Studio Visualizer v20.1.0.19295, developed by Dassault Systèmes (https://www.3ds.com/products-services/biovia/) and overlay similarity was evaluated taking the parent Pht scaffold (Pht conjugated with benzimidazole and 1,2,3-triazole) as a reference compound. Chemical structures of the Pht analogs were drawn by using ChemDraw Ultra 12.0.2, followed by generating their energy-minimized 3D structural models by using Chem3D Pro 12.0 (https://perkinelminformatics.com/products/research/chemdraw/), as described previously by our group [88]. Molecular docking studies were performed by using Autodock Vina Tools 1.5.6 to rationalize the inhibitory activities of the Pht analogs against *Pf*αI-β tubulin [97]. We ensured that the whole tubulin heterodimer was covered while constructing the virtual grid for docking. For this, a virtual 3D grid of 64 × 70 × 90, with x, y, z coordinates of the center of energy: 227.06, 386.225 and 192.023, respectively, was constructed using Autogrid module of AutoDock Tools. Top scoring docked conformations of the Pht analogs were selected based on their most negative free binding energies and visualized for polar contacts (if any) with the amino acid residues of *Pf*αI-β tubulin by using PyMOL Molecular Graphics System [98].

3.12. In vivo antimalarial activity assay

The *in vivo* antimalarial activity of Pht analogs was observed by the method described previously and was carried out at Jawaharlal Nehru University, New Delhi, India [99,100]. Briefly, intra-peritoneal injection of 1×10^7 *Pb* infected erythrocytes diluted with sterile 1xPBS was injected into mice. In each group four mice were taken. Making thin smears from the tail blood of mice checked infection. Post infection, mice were administered intra-peritoneal route with Pht analogs (30 mg/kg body weight) for seven consecutive days. Mice treated with 1xPBS were kept as vehicle control. Parasitemia was counted by making thin blood smears from day 1 to up to day 7. Data was calculated and presented as percent increase in the parasitemia.

3.13. Statistical analysis

The data were calculated as one-way analysis of variance (ANOVA)

to observe the mean values obtained for control and after treatment with analogs. Dunnett's test was used to compare the treatment and control and statistical significance was set at $P \leq 0.01$.

Author contributions

Declaration of competing interest

The authors declare that they have no known competing financial interests or personal relationships that could have appeared to influence the work reported in this paper.

Acknowledgements

Appendix A. Supplementary data

Supplementary data to this article can be found online at https://doi.org/10.1016/j.ejmech.2022.114534.

References

[1] S.J. Draper, B.K. Sack, C.R. King, C.M. Nielsen, J.C. Rayner, M.K. Higgins, C.A. Long, R.A. Seder, Malaria vaccines: recent advances and new horizons, Cell Host Microbe 24 (2018), https://doi.org/10.1016/j.chom.2018.06.008.

[2] J. Talapko, I. Škrlec, T. Alebić, M. Jukić, A. Včev, Malaria: the past and the present, Microorganisms 7 (2019), https://doi.org/10.3390/microorganisms7060179.

[3] E.A. Ashley, M. Dhorda, R.M. Fairhurst, C. Amaratunga, P. Lim, S. Suon, S. Sreng, J.M. Anderson, S. Mao, B. Sam, C. Sopha, C.M. Chuor, C. Nguon, S. Sovannaroth, S. Pukrittayakamee, P. Jittamala, K. Chotivanich, K. Chutasmit, C. Suchatsoonthorn, R. Runcharoen, T.T. Hien, N.T. Thuy-Nhien, N.V. Thanh, N.H. Phu, Y. Htut, K.-T. Han, K.H. Aye, O.a. Mokuolu, R.R. Olaosebikan, O.O. Folaranmi, M. Mayxay, M. Khanthavong, B. Hongvanthong, P.N. Newton, M.a. Onyamboko, C.I. Fanello, A.K. Tshefu, N. Mishra, N. Valecha, A.P. Phyo, F. Nosten, P. Yi, R. Tripura, S. Borrmann, M. Bashraheil, J. Peshu, M.A. Faiz, A. Ghose, M.A. Hossain, R. Samad, M.R. Rahman, M.M. Hasan, A. Islam, O. Miotto, R. Amato, B. MacInnis, J. Stalker, D.P. Kwiatkowski, Z. Bozdech, A. Jeeyapant, P.Y. Cheah, T. Sakulthaew, J. Chalk, B. Intharabut, K. Silamut, S.J. Lee, B. Vihokhern, C. Kunasol, M. Imwong, J. Tarning, W.J. Taylor, S. Yeung, C.J. Woodrow, J.a. Flegg, D. Das, J. Smith, M. Venkatesan, C.V. Plowe, K. Stepniewska, P.J. Guerin, A.M. Dondorp, N.P. Day, N.J. White, 00270 spread of artemisinin resistance in plasmodium falciparum malaria, N. Engl. J. Med. (2014), https://doi.org/10.1056/NEJMoa1314981.

[4] E.A. Winzeler, M.J. Manary, Drug resistance genomics of the antimalarial drug artemisinin, Genome Biol. (2014), https://doi.org/10.1186/s13059-014-0544-6.

[5] A.M. Thu, A.P. Phyo, J. Landier, D.M. Parker, F.H. Nosten, Combating multidrug-resistant Plasmodium falciparum malaria, FEBS J. 284 (2017), https://doi.org/10.1111/febs.14127.

[6] N. Kushwaha, D. Kaushik, Recent advances and future prospects of phthalimide derivatives, J. Appl. Pharmaceut. Sci. 6 (2016), https://doi.org/10.7324/JAPS.2016.60330.

[7] H. Shiheido, F. Terada, N. Tabata, I. Hayakawa, N. Matsumura, H. Takashima, Y. Ogawa, W. Du, T. Yamada, M. Shoji, T. Sugai, N. Doi, S. Iijima, Y. Hattori, H. Yanagawa, A phthalimide derivative that inhibits centrosomal clustering is effective on multiple myeloma, PLoS One 7 (2012), https://doi.org/10.1371/journal.pone.0038878.

[8] L.C.D. Coêlho, M.V.D.O. Cardoso, D.R.M. Moreira, P.A.T.D.M. Gomes, S.M.T. Cavalcanti, A.R. Oliveira, G.B.D.O. Filho, L.R.P. De Siqueira, M.D.O. Barbosa, E.F.D.O. Borba, T.G. Da Silva, B. Kaskow, M. Karimi, L.J. Abraham, A.C.L. Leite, Novel phthalimide derivatives with TNF-α and IL-1β expression inhibitory and apoptotic inducing properties, Medchemcomm 5 (2014), https://doi.org/10.1039/c4md00070f.

[9] M. Horvat, L. Uzelac, M. Marjanović, N. Cindro, O. Franković, K. Mlinarić-Majerski, M. Kralj, N. Basarić, Evaluation of Antiproliferative Effect of N-(alkyladamantyl)phthalimides in vitro, Chem. Biol. Drug Des. 79 (2012), https://doi.org/10.1111/j.1747-0285.2011.01305.x.

[10] J.G. da Silva Júnior, Therapeutic potential of phthalimide derivatives: a review, Am. J. Biomed. Sci. Res. 3 (2019), https://doi.org/10.34297/ajbsr.2019.03.000699.

[11] K. Shah, S. Chhabra, S.K. Shrivastava, P. Mishra, Benzimidazole: a promising pharmacophore, Med. Chem. Res. 22 (2013), https://doi.org/10.1007/s00044-013-0476-9.

[12] F.W. Muregi, A. Ishih, Next-generation antimalarial drugs: hybrid molecules as a new strategy in drug design, Drug Dev. Res. 71 (2010), https://doi.org/10.1002/ddr.20345.

[13] D. Agarwal, R.D. Gupta, S.K. Awasthi, Are antimalarial hybrid molecules a close reality or a distant dream? Antimicrob. Agents Chemother. 61 (2017) https://doi.org/10.1128/AAC.00249-17.

[14] S. Singh, N. El-sakkary, D.E. Skinner, P.P. Sharma, S. Ottilie, Y. Antonova-koch, P. Kumar, E. Winzeler, Poonam, C.R. Caffrey, B. Rathi, Synthesis and bioactivity of phthalimide analogs as potential drugs to treat schistosomiasis, a neglected disease of poverty, Pharmaceuticals 13 (2020), https://doi.org/10.3390/ph13020025.

[15] P. Kumar, A.O. Achieng, V. Rajendran, P.C. Ghosh, B.K. Singh, M. Rawat, D.J. Perkins, P. Kempaiah, B. Rathi, Synergistic blending of high-valued heterocycles inhibits growth of Plasmodium falciparum in culture and P. berghei infection in mouse model, Sci. Rep. 7 (2017), https://doi.org/10.1038/s41598-017-06097-z.

[16] A.K. Singh, V. Rajendran, A. Pant, P.C. Ghosh, N. Singh, N. Latha, S. Garg, K.C. Pandey, B.K. Singh, B. Rathi, Design, synthesis and biological evaluation of functionalized phthalimides: a new class of antimalarials and inhibitors of falcipain-2, a major hemoglobinase of malaria parasite, Bioorg. Med. Chem. 23 (2015), https://doi.org/10.1016/j.bmc.2015.02.029.

[17] A.K. Singh, S. Rathore, Y. Tang, N.E. Goldfarb, B.M. Dunn, V. Rajendran, P.C. Ghosh, N. Singh, N. Latha, B.K. Singh, M. Rawat, B. Rathi, Hydroxyethylamine based phthalimides as new class of plasmepsin hits: design, synthesis and antimalarial evaluation, PLoS One 10 (2015), https://doi.org/10.1371/journal.pone.0139347.

[18] N. Boechat, L.C.S. Pinheiro, T.S. Silva, A.C.C. Aguiar, A.S. Carvalho, M.M. Bastos, C.C.P. Costa, S. Pinheiro, A.C. Pinto, J.S. Mendonça, K.D.B. Dutra, A.L. Valverde, O.A. Santos-Filho, I.P. Ceravolo, A.U. Krettli, New trifluoromethyl triazolopyrimidines as Anti-Plasmodium falciparum agents, Molecules 17 (2012), https://doi.org/10.3390/molecules17078285.

[19] R.B. de Oliveira, E.M. de Souza-Fagundes, R.P.P. Soares, A.A. Andrade, A.U. Krettli, C.L. Zani, Synthesis and antimalarial activity of semicarbazone and thiosemicarbazone derivatives, Eur. J. Med. Chem. 43 (2008), https://doi.org/10.1016/j.ejmech.2007.11.012.

[20] G. François, Naphthylisoquinoline alkaloids exhibit strong growth-inhibiting activities against Plasmodium falciparum and P. berghei in vitro -Structure-activity relationships of dioncophylline C, Ann. Trop. Med. Parasitol. 90 (1996), https://doi.org/10.1080/00034983.1996.11813035.

[21] M.L. Gazarini, C.R.S. Garcia, Interruption of the blood-stage cycle of the malaria parasite, Plasmodium chabaudi, by protein tyrosine kinase inhibitors, Braz. J. Med. Biol. Res. 36 (2003), https://doi.org/10.1590/S0100-879X2003001100003.

[22] T.S. Skinner, L.S. Manning, W.A. Johnston, T.M.E. Davis, In vitro stage-specific sensitivity of Plasmodium falciparum to quinine and artemisinin drugs, Int. J. Parasitol. 26 (1996), https://doi.org/10.1016/0020-7519(96)89380-5.

[23] D. Engelbrecht, P.M. Durand, T.L. Coetzer, On programmed cell death in Plasmodium falciparum: status quo, J. Trop. Med. (2012), https://doi.org/10.1155/2012/646534.

[24] A. Roy, A. Ganguly, S. BoseDasgupta, B.B. Das, C. Pal, P. Jaisankar, H.K. Majumder, Mitochondria-dependent reactive oxygen species-mediated programmed cell death induced by 3,3′-diindolylmethane through inhibition of F0F1-ATP synthase in unicellular protozoan parasite Leishmania donovani, Mol. Pharmacol. 74 (2008), https://doi.org/10.1124/mol.108.050161.

[25] H. Xie, V.A. Valera, M.J. Merino, A.M. Amato, S. Signoretti, W.M. Linehan, V.P. Sukhatme, P. Seth, LDH-A inhibition, a therapeutic strategy for treatment of hereditary leiomyomatosis and renal cell cancer, Mol. Cancer Therapeut. 8 (2009), https://doi.org/10.1158/1535-7163.MCT-08-1049.

[26] J. Wang, L. Huang, J. Li, Q. Fan, Y. Long, Y. Li, B. Zhou, Artemisinin directly targets malarial mitochondria through its specific mitochondrial activation, PLoS One 5 (2010), https://doi.org/10.1371/journal.pone.0009582.

[27] S. Gupta, M.M. Thapar, W.H. Wernsdorfer, A. Björkman, In vitro interactions of artemisinin with atovaquone, quinine, and mefloquine against Plasmodium falciparum, Antimicrob, Agents Chemother 46 (2002), https://doi.org/10.1128/AAC.46.5.1510-1515.2002.

[28] D.N. Nandakumar, V.A. Nagaraj, P.G. Vathsala, P. Rangarajan, G. Padmanaban, Curcumin-artemisinin combination therapy for malaria, Antimicrob. Agents Chemother. 50 (2006), https://doi.org/10.1128/AAC.50.5.1859-1860.2006.

[29] A. Bhattacharya, L.C. Mishra, V.K. Bhasin, In vitro activity of artemisinin in combination with clotrimazole or heat-treated amphotericin B against Plasmodium falciparum, Am. J. Trop. Med. Hyg. 78 (2008), https://doi.org/10.4269/ajtmh.2008.78.721.

[30] Z. Neto, M. Machado, A. Lindeza, V. Do Rosário, M.L. Gazarini, D. Lopes, Treatment of plasmodium chabaudi parasites with curcumin in combination with antimalarial drugs: drug interactions and implications on the ubiquitin/proteasome system, J. Parasitol. Res. (2013), https://doi.org/10.1155/2013/429736, 2013.

[31] C.P.H. Yang, S.B. Horwitz, Taxol®: the first microtubule stabilizing agent, Int. J. Mol. Sci. 18 (2017), https://doi.org/10.3390/ijms18081733.

[32] J.D. Warncke, H.-P. Beck, Host cytoskeleton remodeling throughout the blood stages of plasmodium falciparum, Microbiol. Mol. Biol. Rev. 83 (2019), https://doi.org/10.1128/mmbr.00013-19.

[33] R. Tomasina, F.C. González, M.E. Francia, Structural and functional insights into the microtubule organizing centers of toxoplasma gondii and plasmodium spp, Microorganisms 9 (2021), https://doi.org/10.3390/microorganisms9122503.

[34] The Role of Microtubules in Cell Biology, Neurobiology, and Oncology, 2008, https://doi.org/10.1007/978-1-59745-336-3.

[35] J. Vanderberg, J. Rdodin, M. Yoeli, Electron microscopic and histochemical studies of sporozoite formation in plasmodium berghei, J. Protozool. 14 (1967), https://doi.org/10.1111/j.1550-7408.1967.tb01452.x.

[36] B. Spreng, H. Fleckenstein, P. Kübler, C. Di Biagio, M. Benz, P. Patra, U. S. Schwarz, M. Cyrklaff, F. Frischknecht, Microtubule number and length determine cellular shape and function in Plasmodium, EMBO J. 38 (2019), https://doi.org/10.15252/embj.2018100984.

[37] M. Cyrklaff, M. Kudryashev, A. Leis, K. Leonard, W. Baumeister, R. Menard, M. Meissner, F. Frischknecht, Cryoelectron tomography reveals periodic material at the inner side of subpellicular microtubules in apicomplexan parasites, J. Exp. Med. 204 (2007), https://doi.org/10.1084/jem.20062405.

[38] X. Wang, P. Qian, H. Cui, L. Yao, J. Yuan, A protein palmitoylation cascade regulates microtubule cytoskeleton integrity in Plasmodium, EMBO J. 39 (2020), https://doi.org/10.15252/embj.2019104168.

[39] B. Liffner, S. Absalon, Expansion microscopy reveals plasmodium falciparum blood-stage parasites undergo anaphase with a chromatin bridge in the absence of mini-chromosome maintenance complex binding protein, Microorganisms 9 (2021), https://doi.org/10.3390/microorganisms9112306.

[40] R. Rashpa, M. Brochet, Expansion microscopy of Plasmodium gametocytes reveals the molecular architecture of a bipartite microtubule organisation centre coordinating mitosis with axoneme assembly, PLoS Pathog. 18 (2022), e1010223.

[41] R.E. Sinden, E.U. Canning, R.S. Bray, M.E. Smalley, Gametocyte and gamete development in Plasmodium falciparum, Proc. R. Soc. London - Biol. Sci. 201 (1978), https://doi.org/10.1098/rspb.1978.0051.

[42] R.E. Sinden, E.U. Canning, B. Spain, Gametogenesis and fertilization in Plasmodium yoelii nigeriensis: a transmission electron microscope study, Proc. R. Soc. London - Biol. Sci. 193 (1976), https://doi.org/10.1098/rspb.1976.0031.

[43] D. Nicastro, C. Schwartz, J. Pierson, R. Gaudette, M.E. Porter, J.R. McIntosh, The molecular architecture of axonemes revealed by cryoelectron tomography, Science (80-) (2006) 313, https://doi.org/10.1126/science.1128618.

[44] B. Kappes, P. Rohrbach, Microtubule inhibitors as a potential treatment for malaria, Future Microbiol. 2 (2007), https://doi.org/10.2217/17460913.2.4.409.

[45] B.J. Fennell, J.A. Naughton, E. Dempsey, A. Bell, Cellular and molecular actions of dinitroaniline and phosphorothioamidate herbicides on Plasmodium falciparum: tubulin as a specific antimalarial target, Mol. Biochem. Parasitol. 145 (2006), https://doi.org/10.1016/j.molbiopara.2005.08.020.

[46] J. Schrevel, V. Sinou, P. Grellier, F. Frappier, D. Guenard, P. Potier, Interactions between docetaxel (Taxotere) and Plasmodium falciparum- infected erythrocytes, Proc. Natl. Acad. Sci. U.S.A. 91 (1994), https://doi.org/10.1073/pnas.91.18.8472.

[47] B.J. Fennell, J.A. Naughton, E. Dempsey, A. Bell, J. Schrevel, V. Sinou, P. Grellier, F. Frappier, D. Guenard, P. Potier, B.J. Fennell, S. Carolan, G.R. Pettit, A. Bell, Effects of the antimitotic natural product dolastatin 10, and related peptides, on the human malarial parasite Plasmodium falciparum, Proc. Natl. Acad. Sci. U.S.A. 91 (1994), https://doi.org/10.1016/j.molbiopara.2005.08.020.

[48] R.E. Fowler, R.E. Fookes, G.H. Mitchell, L.H. Bannister, Malaria, microtubules and merozoite invasion: reply, parasitol, Today Off. 14 (1998), https://doi.org/10.1016/s0169-4758(97)01172-1.

[49] G.S. Dow, A. Armson, M.R. Boddy, T. Itenge, D. McCarthy, J.E. Parkin, R.C. A. Thompson, J.A. Reynoldson, Plasmodium: assessment of the antimalarial potential of trifluralin and related compounds using a rat model of malaria, Rattus norvegicus, Exp. Parasitol. 100 (2002), https://doi.org/10.1016/S0014-4894(02)00016-4.

[50] E. Bertiaux, A.C. Balestra, L. Bournonville, V. Louvel, B. Maco, D. Soldati-Favre, M. Brochet, P. Guichard, V. Hamel, Expansion microscopy provides new insights into the cytoskeleton of malaria parasites including the conservation of a conoid, PLoS Biol. 19 (2021), https://doi.org/10.1371/journal.pbio.3001020.

[51] F. Torres, M. Garcia-Rubino, C. Lozano-Lopez, D. Kawano, V. Eifler-Lima, G. Poser, J. Campos, Imidazoles and benzimidazoles as tubulin-modulators for anti-cancer therapy, Curr. Med. Chem. 22 (2015), https://doi.org/10.2174/0929867322666150114164032.

[52] M.K. Jung, B.R. Oakley, Identification of an amino acid substitution in the benA, β-tubulin gene of Aspergillus nidulans that confers thiabendazole resistance and benomyl supersensitivity, Cell Motil Cytoskeleton 17 (1990), https://doi.org/10.1002/cm.970170204.

[53] M.S.G. Kwa, F.N.J. Kooyman, J.H. Boersema, M.H. Roos, Effect of selection for benzimidazole resistance in Haemonchus contortus on β-tubulin isotype 1 and isotype 2 genes, Biochem. Biophys. Res. Commun. 191 (1993), https://doi.org/10.1006/bbrc.1993.1233.

[54] S.K. Katiyar, V.R. Gordon, G.L. McLaughlin, T.D. Edlind, Antiprotozoal activities of benzimidazoles and correlations with β- tubulin sequence, Antimicrob. Agents Chemother. 38 (1994), https://doi.org/10.1128/AAC.38.9.2086.

[55] L. Serrano, J. De la Torre, R.B. Maccioni, J. Avila, Involvement of the carboxyl-terminal domain of tubulin in the regulation of its assembly, Proc. Natl. Acad. Sci. U.S.A. 81 (1984), https://doi.org/10.1073/pnas.81.19.5989.

[56] G.W. Lubega, R.K. Prichard, Beta-tubulin and benzimidazole resistance in the sheep nematode Haemonchus contortus, Mol. Biochem. Parasitol. 47 (1991), https://doi.org/10.1016/0166-6851(91)90155-Y.

[57] A. Banerjee, R.F. Luduena, Kinetics of colchicine binding to purified β-tubulin isotypes from bovine brain, J. Biol. Chem. 267 (1992), https://doi.org/10.1016/s0021-9258(18)42215-6.

[58] L.J. Floyd, L.D. Barnes, R.F. Williams, Photoaffinity labeling of tubulin with (2-nitro-4-azidophenyl)deacetylcolchicine: direct evidence for two colchicine binding sites, Biochemistry 28 (1989), https://doi.org/10.1021/bi00447a037.

[59] D.L. Sackett, B. Bhattacharyya, J. Wolff, Local unfolding and the stepwise loss of the functional properties of tubulin, Biochemistry 33 (1994), https://doi.org/10.1021/bi00209a019.

[60] M.E. Oxberry, T.G. Geary, R.K. Prichard, Assessment of benzimidazole binding to individual recombinant tubulin isotypes from Haemonchus contortus, Parasitology 122 (2001), https://doi.org/10.1017/S0031182001007788.

[61] D.J. Fu, J. Song, Y.H. Hou, R.H. Zhao, J.H. Li, R.W. Mao, J.J. Yang, P. Li, X.L. Zi, Z.H. Li, Q.Q. Zhang, F.Y. Wang, S.Y. Zhang, Y.B. Zhang, H.M. Liu, Discovery of 5,6-diaryl-1,2,4-triazines hybrids as potential apoptosis inducers, Eur. J. Med. Chem. 138 (2017), https://doi.org/10.1016/j.ejmech.2017.07.011.

[62] S.Y. Zhang, D.J. Fu, X.X. Yue, Y.C. Liu, J. Song, H.H. Sun, H.M. Liu, Y.B. Zhang, Design, synthesis and structure-activity relationships of novel chalcone-1,2,3-triazole-azole derivates as antiproliferative agents, Molecules 21 (2016), https://doi.org/10.3390/molecules21050653.

[63] D.J. Fu, S.Y. Zhang, Y.C. Liu, X.X. Yue, J.J. Liu, J. Song, R.H. Zhao, F. Li, H. H. Sun, Y.B. Zhang, H.M. Liu, Design, synthesis and antiproliferative activity studies of 1,2,3-triazole-chalcones, Medchemcomm 7 (2016), https://doi.org/10.1039/c6md00169f.

[64] D.J. Fu, J.F. Liu, R.H. Zhao, J.H. Li, S.Y. Zhang, Y.B. Zhang, Design and antiproliferative evaluation of novel sulfanilamide derivatives as potential tubulin polymerization inhibitors, Molecules 22 (2017), https://doi.org/10.3390/molecules22091470.

[65] L. Cafici, T. Pirali, F. Condorelli, E. Del Grosso, A. Massarotti, G. Sorba, P. L. Canonico, G.C. Tron, A.A. Genazzani, Solution-phase parallel synthesis and biological evaluation of combretatriazoles, J. Comb. Chem. 10 (2008), https://doi.org/10.1021/cc800090d.

[66] J.A. Stefely, R. Palchaudhuri, P.A. Miller, R.J. Peterson, G.C. Moraski, P. J. Hergenrother, M.J. Miller, N -((1-benzyl-1 H -1,2,3-triazol-4-yl)methyl) arylamide as a new scaffold that provides rapid access to antimicrotubule agents: synthesis and evaluation of antiproliferative activity against select cancer cell lines, J. Med. Chem. 53 (2010), https://doi.org/10.1021/jm1000979.

[67] D.J. Fu, P. Li, B.W. Wu, X.X. Cui, C. Bin Zhao, S.Y. Zhang, Molecular diversity of trimethoxyphenyl-1,2,3-triazole hybrids as novel colchicine site tubulin polymerization inhibitors, Eur. J. Med. Chem. 165 (2019), https://doi.org/10.1016/j.ejmech.2019.01.033.

[68] A. Daina, O. Michielin, V. Zoete, SwissADME: a free web tool to evaluate pharmacokinetics, drug-likeness and medicinal chemistry friendliness of small molecules, Sci. Rep. 7 (2017), https://doi.org/10.1038/srep42717.

[69] C.A. Lipinski, F. Lombardo, B.W. Dominy, P.J. Feeney, Experimental and computational approaches to estimate solubility and permeability in drug discovery and development settings 1PII of original article: S0169-409X(96) 00423-1. The article was originally published in Advanced Drug Delivery Reviews 23 (1997), Adv. Drug Deliv. Rev. 46 (2002) 3–26, https://doi.org/10.1016/s0169-409x(00)00129-0.

[70] S. Singh, V. Rajendran, J. He, A.K. Singh, A.O. Achieng, Vandana, A. Pant, A. S. Nasamu, M. Pandit, J. Singh, A. Quadiri, N. Gupta, Poonam, P.C. Ghosh, B. K. Singh, L. Narayanan, P. Kempaiah, R. Chandra, B.M. Dunn, K.C. Pandey, D. E. Goldberg, A.P. Singh, B. Rathi, Fast-acting small molecules targeting malarial aspartyl proteases, plasmepsins, inhibit malaria infection at multiple life stages, ACS Infect. Dis. 5 (2019), https://doi.org/10.1021/acsinfecdis.8b00197.

[71] A.K. Singh, V. Rajendran, S. Singh, P. Kumar, Y. Kumar, A. Singh, W. Miller, V. Potemkin, Poonam, M. Grishina, N. Gupta, P. Kempaiah, R. Durvasula, B. K. Singh, B.M. Dunn, B. Rathi, Antiplasmodial activity of hydroxyethylamine analogs: synthesis, biological activity and structure activity relationship of plasmepsin inhibitors, Bioorg. Med. Chem. 26 (2018), https://doi.org/10.1016/j.bmc.2018.06.037.

[72] C. Upadhyay, M. Chaudhary, R.N. De Oliveira, A. Borbas, P. Kempaiah, P. Singh, B. Rathi, Fluorinated scaffolds for antimalarial drug discovery, Expet Opin. Drug Discov. 15 (2020), https://doi.org/10.1080/17460441.2020.1740203.

[73] B.C. Evans, C.E. Nelson, S.S. Yu, K.R. Beavers, A.J. Kim, H. Li, H.M. Nelson, T. D. Giorgio, C.L. Duvall, Ex vivo red blood cell hemolysis assay for the evaluation of pH-responsive endosomolytic agents for cytosolic delivery of biomacromolecular drugs, JoVE (2013), https://doi.org/10.3791/50166.

[74] H.B. Reilly, H. Wang, J.A. Steuter, A.M. Marx, M.T. Ferdig, Quantitative dissection of clone-specific growth rates in cultured malaria parasites, Int. J. Parasitol. 37 (2007), https://doi.org/10.1016/j.ijpara.2007.05.003.

[75] M.T. Makler, D.J. Hinrichs, Measurement of the lactate dehydrogenase activity of Plasmodium falciparum as an assessment of parasitemia, Am. J. Trop. Med. Hyg. 48 (1993), https://doi.org/10.4269/ajtmh.1993.48.205.

[76] C. Moneriz, P. Marín-García, A. García-Granados, J.M. Bautista, A. Diez, A. Puyet, Parasitostatic effect of maslinic acid. I. Growth arrest of Plasmodium falciparum intraerythrocytic stages, Malar. J. 10 (2011), https://doi.org/10.1186/1475-2875-10-82.

[77] E. Gottlieb, S.M. Armour, M.H. Harris, C.B. Thompson, Mitochondrial membrane potential regulates matrix configuration and cytochrome c release during apoptosis, Cell Death Differ. 10 (2003), https://doi.org/10.1038/sj.cdd.4401231.

[78] D.M. Rhoads, A.L. Umbach, C.C. Subbaiah, J.N. Siedow, Mitochondrial reactive oxygen species. Contribution to oxidative stress and interorganellar signaling, Plant Physiol. 141 (2006), https://doi.org/10.1104/pp.106.079129.

[79] D.F. Suen, K.L. Norris, R.J. Youle, Mitochondrial dynamics and apoptosis, Genes Dev. 22 (2008), https://doi.org/10.1101/gad.1658508.

[80] H.A. Perez, M. De la Rosa, R. Apitz, In vivo activity of ajoene against rodent malaria, Antimicrob, Agents Chemother 38 (1994), https://doi.org/10.1128/AAC.38.2.337.

[81] M.A.M. Ridzuan, U. Ruenruetai, A.N. Rain, S. Khozirah, I. Zakiah, Antimalarial properties of Goniothalamin in combination with chloroquine against Plasmodium yoelii and Plasmodium berghei growth in mice, Trop. Biomed. 23 (2006).

[82] P. Rasoanaivo, C.W. Wright, M.L. Willcox, B. Gilbert, Whole plant extracts versus single compounds for the treatment of malaria: synergy and positive interactions, Malar. J. 10 (2011), https://doi.org/10.1186/1475-2875-10-S1-S4.

[83] Q.L. Fivelman, I.S. Adagu, D.C. Warhurst, Modified fixed-ratio isobologram method for studying in vitro interactions between atovaquone and proguanil or dihydroartemisinin against drug-resistant strains of Plasmodium falciparum, Antimicrob. Agents Chemother. 48 (2004), https://doi.org/10.1128/AAC.48.11.4097-4102.2004.

[84] M. Chakrabarti, N. Joshi, G. Kumari, P. Singh, R. Shoaib, A. Munjal, V. Kumar, A. Behl, M. Abid, S. Garg, S. Gupta, S. Singh, Interaction of Plasmodium falciparum apicortin with α- and β-tubulin is critical for parasite growth and survival, Sci. Rep. 11 (2021), https://doi.org/10.1038/s41598-021-83513-5.

[85] R. Jain, P. Dey, S. Gupta, S. Pati, A. Bhattacherjee, M. Munde, S. Singh, Molecular dynamics simulations and biochemical characterization of Pf14-3-3 and PfCDPK1 interaction towards its role in growth of human malaria parasite, Biochem. J. 477 (2020), https://doi.org/10.1042/BCJ20200145.

[86] R. Jain, S. Gupta, M. Munde, S. Pati, S. Singh, Development of novel anti-malarial from structurally diverse library of molecules, targeting plant-like CDPK1, a multistage growth regulator of P. falciparum, Biochem. J. 447 (2020), https://doi.org/10.1042/BCJ20200045.

[87] M. Hashimoto, E. Girardi, R. Eichner, G. Superti-Furga, Detection of chemical engagement of solute carrier proteins by a cellular thermal shift assay, ACS Chem. Biol. 13 (2018) 1480–1486, https://doi.org/10.1021/acschembio.8b00270.

[88] S.S. Dangi P, R. Jain, R. Mamidala, V. Sharma, S. Agarwal, C. Bathula, M. Thirumalachary, S. Sen, Natural product inspired novel indole based chiral scaffold kills human malaria parasites via ionic imbalance mediated cell death, Sci. Rep. 9 (2019), https://doi.org/10.1038/s41598-019-54339-z.

[89] C. Aurrecoechea, J. Brestelli, B.P. Brunk, J. Dommer, S. Fischer, B. Gajria, X. Gao, A. Gingle, G. Grant, O.S. Harb, M. Heiges, F. Innamorato, J. Iodice, J.C. Kissinger, E. Kraemer, W. Li, J.A. Miller, V. Nayak, C. Pennington, D.F. Pinney, D.S. Roos, C. Ross, C.J. Stoeckert, C. Treatman, H. Wang, PlasmoDB: a functional genomic database for malaria parasites, Nucleic Acids Res. 37 (2009) D539–D543, https://doi.org/10.1093/nar/gkn814.

[90] S.F. Altschul, W. Gish, W. Miller, E.W. Myers, D.J. Lipman, Basic local alignment search tool, J. Mol. Biol. 215 (1990) 403–410, https://doi.org/10.1016/S0022-2836(05)80360-2.

[91] H.M. Berman, J. Westbrook, Z. Feng, G. Gilliland, T.N. Bhat, H. Weissig, I. N. Shindyalov, P.E. Bourne, The protein Data Bank, Nucleic Acids Res. 28 (2000) 235–242, https://doi.org/10.1002/0471721204.ch9.

[92] J. Löwe, H. Li, K.H. Downing, E. Nogales, Refined structure of alpha beta-tubulin at 3.5 A resolution, J. Mol. Biol. 313 (2001).

[93] B. Webb, A. Sali, Comparative protein structure modeling using MODELLER, Curr. Protoc. Bioinforma. 54 (2016), https://doi.org/10.1002/cpbi.3, 5.6.1-5.6.37.

[94] D. Xu, Y. Zhang, Improving the physical realism and structural accuracy of protein models by a two-step atomic-level energy minimization, Biophys. J. 101 (2011) 2525–2534, https://doi.org/10.1016/j.bpj.2011.10.024.

[95] G.N. Ramachandran, V. Sasisekharan, Conformation of polypeptides and proteins, Adv. Protein Chem. 23 (1968) 283–437, https://doi.org/10.1016/S0065-3233(08)60402-7.

[96] R.A. Laskowski, M.W. MacArthur, J.M. Thornton, PROCHECK: a program to check the stereochemical quality of protein structures, J. Appl. Crystallogr. 26 (1993) 283–291.

[97] oleg Trott, Arthur J. Olson, AutoDock Vina, Improving the speed and accuracy of docking with a new scoring function, efficient optimization, and multithreading, J. Comput. Chem. 31 (2010) 455–461, https://doi.org/10.1002/jcc.

[98] W.L. Delano, The PyMOL Molecular Graphics System, Schrodinger, 2002.

[99] D.J. Knight, W. Peters, The antimalarial activity of N-benzyloxydihydrotriazines: I. The activity of clociguanil (BRL 50216) against rodent malaria, and studies on its mode of action, Ann. Trop. Med. Parasitol. 74 (1980), https://doi.org/10.1080/00034983.1980.11687360.

[100] S. Ounjaijean, M. Kotepui, V. Somsak, Antimalarial activity of tinospora baenzigeri against plasmodium berghei- infected mice, J. Trop. Med. (2019), https://doi.org/10.1155/2019/5464519, 2019.

RSC
Medicinal Chemistry

Accepted Manuscript

RSC
Medicinal Chemistry

ROYAL SOCIETY
OF CHEMISTRY

ROYAL SOCIETY
OF CHEMISTRY

rsc.li/medchem

ARTICLE

Biological Activity and Structure–Activity Relationship of Dehydrodieugenol B Analogues against Visceral Leishmaniasis

Maiara Amaral[a,b], ‡ Hannah Asiki[c], ‡ Claire E. Sear[c], Snigdha Singh,[c] Pauline Pieper[c], Marius M. Haugland[c], Edward A. Anderson[c]* and Andre G. Tempone[b]*

Visceral leishmaniasis is a neglected protozoan disease with high mortality. Existing treatments exhibit a number of limitations, resulting in a significant challenge for public health, especially in developing countries in which the disease is endemic. With a limited pipeline of potential drugs in clinical trials, natural products could offer an attractive source of new pharmaceutical prototypes, not least due to their high chemodiversity. In the present work, a study of anti-*L. (L.) infantum* potential was carried out for a series of 39 synthetic compounds based on the core scaffold of the neolignan dehydrodieugenol B. Of these, 14 compounds exhibited activity against intracellular amastigotes, with 50% Inhibitory Concentration (IC_{50}) values between 3.0 and 32.7 μM. A structure–activity relationship (SAR) analysis demonstrated a requirement for polar functionalities to improve activity. Lacking mammalian cytotoxicity and presenting the highest potency against the clinically relevant form of the parasite, compound **24** emerged as the most promising, fulfilling the hit criteria for visceral leishmaniasis defined by the Drugs for Neglected Diseases initiative (DND*i*). This study emphasizes the potential of dehydrodieugenol B analogues as new candidates for the treatment of visceral leishmaniasis and suggests **24** to be a suitable compound for future optimization, including mechanism of action and pharmacokinetic studies.
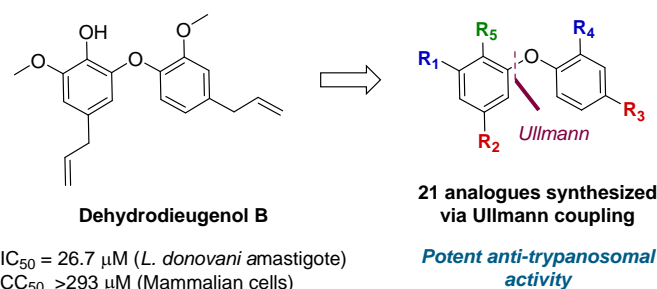
Introduction

Leishmaniases are neglected tropical diseases caused by parasites of the genus *Leishmania* which affect more than 12 million people worldwide, mainly in low-income populations. The disease complex is present in 98 countries, with approximately 1.3 million new cases per year and 350 million people at risk of infection (World Health Organization, 2017; Lee et al., 2019). Human visceral leishmaniasis (VL) is a systemic disease which typically affects mononuclear phagocytic system cells. If treated, VL mortality rates can be as low as 10 to 20%; but if untreated, the disease is 100% fatal within two years (Hailu, 2016). Although VL is the most severe form of the disease, it has received relatively little attention in terms of new treatments; a limited chemotherapeutic arsenal is available, with many current therapies eliciting adverse effects (Jain and Jain, 2018). As a result, the search for safe and accessible therapeutic alternatives is of exceptional importance.

In the search for new drugs, natural products stand out as compounds that offer enormous pharmacological potential. Newman and Cragg (2020) showed that approximately 50% of all FDA-approved drugs feature natural product scaffolds as the basis of their pharmacophores. Our previous studies described the anti-*Leishmania* (*L.*) *donovani* and anti-*Trypanosoma* (*T.*) *cruzi* activity of a small family of neolignans isolated from branches and leaves of *Nectandra leucanta* (Lauraceae) (Costa-Silva et al., 2015; Grecco et al., 2017a, 2017b). Subsequently, using dehydrodieugenol B, four new semi-synthetic compounds were prepared and their antileishmanial activity reported (Amaral et al., 2019).

A total synthesis of dehydrodieugenol B was developed based on a copper-catalyzed Ullmann coupling to form the biaryl ether core (Sear et al., 2020) (Figure 1). This enabled site-specific modifications, and evaluation of a series of analogues against *T. cruzi*, resulting in the identification of several compounds that displayed enhanced bioactivity and selectivity against the trypomastigote form of the parasite, and meeting the Drugs for Neglected Diseases initiative (DND*i*) criteria for hit compounds (Katsuno et al, 2015).

a Instituto de Medicina Tropical, Faculdade de Medicina, Universidade de Sao Paulo, Sao Paulo - 05403-000, Brazil.
b Centre for Parasitology and Mycology, Instituto Adolfo Lutz, São Paulo -01246-000, Brazil.
c Chemistry Research Laboratory, Department of Chemistry, University of Oxford, 12 Mansfield Road, Oxford, OX1 3TA, U.K.
‡These authors contributed equally.
*Corresponding authors: AGT (andre.tempone@ial.sp.gov.br); EAA (edward.anderson@chem.ox.ac.uk).

Figure 1. Previous work on dehydrodieugenol B synthesis and anti-parasitic activity of natural product analogues.

Dehydrodieugenol B

IC_{50} = 26.7 μM (*L. donovani* amastigote)
CC_{50} >293 μM (Mammalian cells)

21 analogues synthesized via Ullmann coupling

Potent anti-trypanosomal activity

RSC Medicinal Chemistry Accepted Manuscript

ARTICLE

In this work, the bioactivity of a series of 39 analogues of dehydrodieugenol B was studied against *Leishmania (L.) infantum* intracellular amastigotes. These compounds feature a variety of structural modifications which aim to improve biological activity over the natural product, and also to obtain information about the pharmacophore. Additionally, absorption, distribution, metabolism, excretion and toxicity (ADMET) parameters of the most promising compounds were evaluated using an *in silico* platform to investigate the drug-likeness profile.

Results and discussion

A series of 39 compounds was synthesized to explore the structure-activity relationships (SAR) of this family as antileishmanial compounds. Three different approaches were employed: I) Substitution on the phenol group of the A-ring (S1); II) Saturation, substitution or removal of the allyl side chains (S2-A and B), and III) Removal of the methoxy groups (S3-A or B) (Figure 2). These compounds were prepared by similar chemistry to our previous work (Sear et al., 2020), using an Ullmann coupling to form the C–O biaryl ether bond to the A ring from appropriately functionalized precursors (see the Supporting Information for synthesis details).
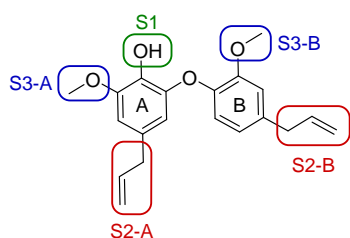
Figure 2. SAR strategy to explore antileishmanial activity of the dehydrodieugenol B scaffold.

The synthesized compounds were evaluated for their anti-*L. (L.) infantum* activity on intracellular amastigotes following 96h treatment, with standard drug miltefosine used as a control. The 50% inhibitory concentration (IC_{50}) was determined by the infection index (Chang et al., 1986), and mammalian toxicity (CC_{50}) for the series was evaluated against NCTC cells.

We first considered modification at the S1 (phenol) position of dehydrodieugenol B (Table 1). Although the p-methoxybenzyl ether of the natural product (**1**) had shown high activity against *T. cruzi* trypomastigotes in our previous work (4.0 ± 1.4 μM), this derivative proved inactive against *L.*(*L.*) *infantum* amastigotes. The introduction of a polar group on the sidechain seems to be necessary for activity, as other modifications at this position were inactive. Having a larger pK_a is beneficial for these compounds as the more basic amines (**4**, **5**) exhibited lower IC_{50} values than their corresponding amides (**6**, **7**), although these four compounds also displayed moderate mammalian cytotoxicity.

Next, the effect of modifying the allyl sidechain functionalities on each of the A and B rings (positions S2) by substitution, saturation or deletion was considered (Table

Table 1. Anti-*Leishmania* (*L.*) *infantum* activity and mammalian cytotoxicity of the dehydrodieugenol B analogues, modification at S1.

Comp.	S1	IC_{50} (μM) ± SD	CC_{50} (μM) ± SD	SI
1	OPMB	NA	>200	ND
2	OMOM	NA	>200	ND
3	OAllyl	NA	>200	ND
4		4.1 ± 1.1	24.9 ± 2.6	6
5		9.6 ± 3.6	63.7 ± 0.2	6.6
6		20.3 ± 5.9	52.9 ± 15.2	2.6
7		NA	111.5 ± 8.2	ND
8	H	NA	>200	ND
Milt.	–	6.5 ± 3.0	119.7 ± 4.2	18.4

CC_{50}: 50% Cytotoxic Concentration in NCTC cells; IC_{50}: 50% Inhibitory Concentration in intracellular amastigotes; SI: Selectivity Index, given by the ratio between CC_{50} and IC_{50}; SD: Standard deviation; ND: Not determined; NA: Not Active (>50 μM); Milt: Miltefosine

2). Saturation or deletion of either of the allyl groups did not lead to antileishmanial activity in any of the analogues prepared, with the exception of moderate activity in **9** and **11**. We noted a detrimental effect on the CC_{50} values in **15**, **17**, and **18**, but this is more likely due to the presence of a free phenol in position S1 and not a result of the saturations or deletions (a result we had observed in our analogous work on *T. cruzi*); all other derivatives showed no toxicity to mammalian cells at the tested concentrations.

The substitution of the allyl sidechains with polar morpholine or piperidine groups led to increased activity in all cases **24**-**30**, although a pyrrolidine substitution (**23**) did not. Substitution at position S2-B tends to result in higher antileishmanial activity (IC_{50} ranging from 3.7 to 9.7 μM) than S2-A (IC_{50} ranging from 13.2 μM to inactive). An attempt to amplify the activity increase with a double substitution (**27**) did not have the desired effect, instead resulting in an IC_{50} value comparable to the less potent S2-A substitutions. Unlike position S1 there does not appear to be a consistent anti-parasitic IC_{50} trend corresponding to the different pKa values for the morpholine (least basic), piperidine and pyrrolidine (most basic) derivatives at position S2. The compounds broadly fit the trend of higher pKa corresponding to higher mammalian cytotoxicity with pyrrolidine containing compound **23** having the worst CC_{50} value for this series.

Table 2. Anti-*Leishmania* (*L.*) *infantum* activity and mammalian cytotoxicity of the dehydrodieugenol B analogues, modification at S2.

Comp	S1	S2A	S2B	IC50 (µM) ± SD	CC50 (µM) ± SD	SI
9	OPMB	Allyl	H	24.2 ± 18.2	>200	>8.3
10	OPMB	H	Allyl	NA	>200	ND
11	OAcyl	Allyl	H	32.7 ± 5.0	>200	>6.1
12	OAcyl	H	Allyl	NA	>200	ND
13	OMe	Allyl	H	NA	>200	ND
14	OMe	H	Allyl	NA	>200	ND
15	OH	Allyl	H	NA	31.6 ± 11.3	ND
16	OH	H	Allyl	NA	>200	ND
17	OH	Allyl	n-Pr	NA	42.0 ± 3.8	ND
18	OH	n-Pr	Allyl	NA	14.2 ± 0.1	ND
19	OMe	Allyl	n-Pr	NA	>200	ND
20	OPMB	Allyl	n-Pr	NA	>200	ND
21	OPMB	n-Pr	Allyl	NA	>200	ND
22	OPMB	n-Pr	n-Pr	NA	>200	ND
23	OPMB	Allyl	*(pyrrolidine structure)*	NA	6.2 ± 1.2	ND
24	OPMB	Allyl	*(morpholine structure)*	9.7 ± 2.0	>200	>20.6
25	OPMB	n-Pr	*(morpholine structure)*	7.7 ± 0.8	74.4 ± 4.4	9.7
26	OPMB	n-Pr	*(piperidine structure)*	3.7 ± 0.5	14.5 ± 0.2	3.9
27	OPMB	*(morpholine structure)*	*(morpholine structure)*	27.8 ± 7.4	74.4 ± 5.8	2.7
28	OPMB	*(morpholine structure)*	n-Pr	16.4 ± 4.3	>200	>12.2
29	*(CF₃ benzyl structure)*	*(morpholine structure)*	n-Pr	13.2 ± 2.1	>200	15.1
30	*(OMe trimethoxy benzyl structure)*	*(morpholine structure)*	n-Pr	26.3 ± 3.2	>200	>7.6
31	OH	Allyl	*(morpholine structure)*	NA	51.4 ± 4.7	ND
32	OH	Allyl	*(pyrrolidine structure)*	NA	43.3 ± 5.3	ND
Milt.	–			6.5 ± 3.0	119.7 ± 4.2	18.4

CC₅₀: 50% Cytotoxic Concentration in NCTC cells; IC₅₀: 50% Inhibitory Concentration in intracellular amastigotes; SI: Selectivity Index, given by the ratio between CC₅₀ and IC₅₀; SD: Standard deviation; ND: Not determined; NA: Not Active (>50 µM); Milt: Miltefosine

Our next step was to investigate ortho-methoxy groups at position **S3** (Table 3). Deletion of the methoxy group at S3-B in compounds **33** and **34** was well-tolerated, with no effect on antileishmanial activity. The same is not true for S3-A: **35** was inactive against *L. (L.) infantum* upon deletion of this methoxy group compared to the corresponding highly active compound **25**. Therefore, the methoxy group at S3-B is expendable, which could offer synthetic benefits, while that at S3-A is crucial for maintaining anti-parasitic activity. These results demonstrate that the presence of a polar functionality such as morpholine, pyrrolidine or piperidine is generally required for anti-*Leishmania (L.) infantum* activity, with 12 of

Table 3. Anti-*Leishmania* (*L.*) *infantum* activity and mammalian cytotoxicity of the dehydrodieugenol B analogues, modification at S3.

Comp	S1	S2A	S2B	S3A	S3B	IC₅₀ (µM) ± SD	CC₅₀ (µM) ± SD	SI
33	OPMB	*(piperidine structure)*	n-Pr	OMe	H	3.0 ± 1.1	22.7 ± 0.9	7.6
34	OPMB	*(morpholine structure)*	n-Pr	OMe	H	15.3 ± 1.9	>200	>13.1
35	OPMB	n-Pr	*(morpholine structure)*	H	OMe	NA	33.8 ± 4.9	ND
36	OPMB	Allyl	Allyl	OMe	H	NA	>200	ND
37	OH	Allyl	Allyl	OMe	H	NA	123.4 ± 9.4	ND
38	OPMB	Allyl	Allyl	H	OMe	NA	>200	ND
39	OH	Allyl	Allyl	H	OMe	NA	128.6 ± 5.2	ND
Milt.	–					6.5 ± 3.0	119.7 ± 4.2	18.4

CC₅₀: 50% Cytotoxic Concentration in NCTC cells; IC₅₀: 50% Inhibitory Concentration in intracellular amastigotes; SI: Selectivity Index, given by the ratio between CC₅₀ and IC₅₀; SD: Standard deviation; ND: Not determined; NA: Not Active (>50 µM); Milt: Miltefosine

the 14 active analogues containing one of these functional groups. **9** and **11** are the only exceptions but display a fairly low activity of 24.2 and 32.7 µM respectively. This polar group requirement could be linked to compound solubility and ability to permeate cell membranes; due to the nature of *Leishmania (L.) infantum* amastigotes residing in intracellular vacuoles the compound must pass through multiple cell membranes to act directly on the parasite. The presence of a free phenol at position S1 (as in the natural product itself) led to no anti-parasitic activity in every example tested, even when paired with a polar functionality as in **31** and **32**, indicating the importance of a substituent in the S1 position. The series **28** to **30** attempted to investigate the effect of decreasing electron density at the benzylic S1 substituent. Electron withdrawing para-trifluoromethylbenzyl group showed a slightly lower IC₅₀ value than strongly electron-donating trimethoxybenzyl, with para-methoxybenzyl having an IC₅₀ in between the two. However, these changes were of a small magnitude indicating electron density at this position is unlikely to play a major role in compound activity. Interestingly, the introduction of a piperidine group leads to lower IC₅₀ values than morpholine substitution: compounds **26** and **33** have potent IC₅₀ values of approximately 3 µM compared with the corresponding morpholine analogues **25** and **34** (7.7 and 15.3 µM respectively). However, this trend is also manifested in the mammalian cytotoxicity, with higher CC₅₀ values for the morpholine analogues, which overall gives the morpholine analogues a higher selectivity index.

Compound **24** emerged as the most favourable with the best selectivity index due to its high anti-parasitic activity (9.7 µM) coupled with no mammalian cytotoxicity (>200 µM). It was therefore selected for an *in silico* study of pharmacokinetic

Table 4. *In silico* predictions of physicochemical, structural and ADMET parameters.

Properties	24	28	34
Molecular weight	505.25	507.26	477.25
LogP	5.18	5.65	5.69
LogD	3.82	4.12	4.17
LogS	-5.27	-6.03	-6.07
TPSA	58.62	58.62	49.39
Caco-2 permeability	-5.03, Optimal	-5.46, Moderate	-5.30, Moderate
Pgp inhibitor	Yes	Yes	Yes
Pgp substrate	No	No	No
HIA (≥30%)	Yes	Yes	Yes
Oral bioavailability	≥30% F	≥30% F	≥30% F
BBB penetration	No	No	No
Distribution (V_D) (L/Kg)	0.72, Optimal	0.72, Optimal	0.95, Optimal
CYP1A2 inhibitor	No	No	No
CYP2C19 inhibitor	Yes	Yes	Yes
CYP2C9 inhibitor	Yes	No	Yes
CYP2D6 inhibitor	No	No	No
CYP3A4 inhibitor	Yes	Yes	Yes
Clearance (mg/min/kg)	11.6, Moderate	11.6, Moderate	11.7 Moderate
hERG blockers	Yes	Yes	Yes
Human hepatotoxicity	No	No	No
AMES toxicity	No	No	No
DILI	Moderate	Moderate	Moderate
Lipinski rules	Fail	Fail	Pass
PAINs	0 alerts	0 alerts	0 alerts

TPSA: Topological Polar Surface Area; P-gp: glycoprotein P; HIA: Human Intestinal Absorption; BBB: Blood Brain Barrier; CYP: cytochrome P450; DILI: Drug Induced Liver Injury

properties alongside closely related analogues **28** and **34**. An analysis of pharmacokinetic properties and structural alerts for compounds **24**, **28** and **34** was conducted using ADMETlab 2.0 (Table 4) (Xiong et al, 2021). The predictions were performed to explore the safety and drug-likeness profile of these analogues.

The physicochemical property analysis for **24** predicts a logP value of 5.18, a close to optimum logD value of 3.82 and water solubility (logS) of -5.27, which falls into the moderate solubility class – an important characteristic that relates to oral bioavailability which we show here to be high (≥30%). Polarity of **24** is also predicted to be favourable (0 < TPSA < 140 Å^2). All these characteristics are improved in **24** compared to the related analogues **28** and **34**, further justification for choosing **24** as the best compound from this series (see the Supporting Information for further analysis on 24). The pharmacokinetic parameter for this series predicts a high Human Intestinal Absorption (HIA) being ≥30%, moderate (compounds **28**, **34**) to optimum (compound **24**) Caco-2 permeability – another model of intestinal absorption, and pleasingly no permeability to the blood-brain barrier, which could lead to side-effects in the nervous system (Monteiro-Neto et al., 2020). The cytochrome P450 superfamily of enzymes are responsible for compound metabolism; inhibition of these enzymes can induce adverse effects and toxicity due to accumulation of drug metabolites (Kirchmair et al, 2015). Of the five main isoforms (CYP1A2, CYP2C19, CYP2C9, CYP2D6, CYP3A4) **24** is proposed to be an inhibitor of three with CYP2C9 and CYP3A4 having only a weak positive result.

Compound **24** exceeds the suggested limit of flexibility (number of rotatable bonds < 11), having 12 rotatable bonds, and lies close to the recommended boundary for size criteria (100 < MW < 600) and lipophilicity (0 < logP < 3.0) although values up to 5.0 are still considered reasonable by Lipinski's rules (Lipinski et al, 1997). Compounds **24** and **28** fail Lipinski's rule due to the high molecular weight (>500), although they are close to the boundary at 505 and 507 respectively. This may imply flexibility issues which should be addressed with future structural optimization. Otherwise, compound **24** demonstrated favourable predictions for toxicity, with no indication of human hepatotoxicity or AMES mutagenicity, and only moderate Drug Induced Liver Injury measurements. It is also important to note there were no structural similarities to pan-assay interference compounds (PAINs).

According to Drugs for Neglected Diseases *initiative* (DND*i*), a new hit compound for Visceral Leishmaniasis, should: i) be synthesized in no more than 8 steps; ii) present IC$_{50}$ lower than 10 µM in amastigotes; iii) have selectivity index higher than 10; iv) exhibit an appropriate *in silico* ADME profile and, v) show no structural alerts (Don and Ioset, 2014; Katsuno et al., 2015). Based on these criteria and the results obtained herein, compound **24** can be considered as a promising hit for Visceral Leishmaniasis.

Experimental

General experimental procedures. MTT was purchased from Molecular Probes® (Invitrogen™). Fetal bovine serum (FBS) was obtained from Gibco. All absorbance readings were performed using the FilterMax F5 Multi-Mode Microplate Reader spectrofluorimeter (Molecular Devices). Proton (^{1}H) NMR spectra were recorded at 400 or 500 MHz and carbon (^{13}C) NMR spectra at 101 or 126 MHz with ^{1}H decoupling. Spectra were

recorded on Bruker AVIIIHD 400 or Bruker AVIIIHD 500 spectrometers with $CDCl_3$ as reference. High-resolution mass spectra (HRMS) were recorded by the Departmental Mass Spectrometry Service, University of Oxford on a Thermo Scientific Exactive Mass Spectrometer (using a Waters Equity autosampler and pump) for electrospray ionisation (ESI).

Animals. Golden hamsters (*Mesocricetus auratus*) and BALB/c mice were obtained from the animal breeding facility of the Instituto Adolfo Lutz - SP and maintained in sterilized cages with controlled environment, and received water and food ad libitum. All animal procedures were performed in accordance with the Guidelines for Care and Use of Laboratory Animals of the Brazilian National Council of Animal Experimentation (COBEA) and had the approval of the Animal Ethics Committee (CEUA IMT-USP 000404A) from University of São Paulo and Instituto Adolfo Lutz – Secretary of Health of Sao Paulo State (CEUA 05/2018).

Parasites and mammalian cell maintenance. *Leishmania (L.) infantum* (MHOM/BR/1972/LD) amastigotes were obtained by differential centrifugation from golden hamsters (*Mesocricetus auratus*) spleens with 60-70 days of infection and the number of parasites was determined by the Stauber method (Stauber et al., 1958). Murine conjunctive fibroblasts NCTC clone 929 (ATCC) were maintained in RPMI-1640 medium supplemented with 10% FBS at pH 7.2 and 37°C in a humidified incubator with 5% CO2. Peritoneal macrophages were by obtained by washing the peritoneal cavity of BALB/c mice with RPMI-1640 medium supplemented with 10% FBS, pH 7.2 and maintained at 37°C in a humidified incubator with 5% CO_2.

Anti-*L. (L.) infantum* activity *in vitro*. Peritoneal macrophages (1x105 /well) were added in 16-well slide chambers (NUNC) and incubated overnight at 37°C with 5% CO_2. Subsequently, the cells were infected with L. (L.) infantum amastigotes (10:1 amastigotes/macrophage) for 24h, treated with compounds serially diluted (6.25 to 50 µM) and incubated for 96h at 37°C with 5% CO_2. Miltefosine was used as standard drug and untreated cells as a negative control. Slides were fixed with methanol, stained with Giemsa and observed under a light microscope (Tempone et al., 2007). The 50% inhibitory concentration (IC_{50}) was determined by the infection index (number of infected macrophages × amastigotes / total macrophages) (Chang et al., 1986).

Mammalian toxicity in vitro. NCTC cells (6x104 /well) were added to 96-well plates and maintained at 37°C in a 5% CO2 humidified incubator for 96h with compounds serially diluted (1.6 to 200 µM). The 50% cytotoxic concentration (CC50) was determined using the MTT colorimetric method and the selectivity index was calculated by the ratio: CC50 against NCTC cells/IC50 against amastigotes (Tada et al., 1986).

In silico analysis. Predictions were performed using the web server ADMETlab 2.0. This platform includes several models for physicochemical properties, solubility, pharmacokinetic / pharmacodynamic parameters, drug-likeness profile and structural alerts for pan-assay interference compounds (PAINS) (Xiong et al, 2021).

Statistical analysis. The determination of CC50 and IC50 values was performed by sigmoid dose-response curves using the Graph Pad Prism 5 software. The samples were tested in duplicate and the assays were reproduced at least twice.

Conclusions

Among 39 tested analogues, 14 were active against the intracellular amastigote form of *Leishmania (L.) infantum*. SAR analysis suggests that polar functionalities are crucial for the activity of this family, with morpholine substituted analogues displaying the best SI. Derivative **24** was the most promising compound from this series, with excellent potency and selectivity, and can be considered a promising hit for VL. It is synthesized in 5 steps in the longest linear sequence (and 6 steps in total), displays promising bioactivity (9.7 µM), low mammalian toxicity (SI > 20.6), and meets the predicted ADME criteria.

Author Contributions

Conceptualization, AGT, EAA and MMH; methodology, MA, HA, CES, SS, PP; software, MA, HA; investigation, MA, HA, CES, SS, PP; resources, EEA and AGT; data curation, EAA and AGT; writing—original draft preparation, MA, HA, writing—review and editing, AGT, EAA, HA and MMH. All authors have read and agreed to the published version of the manuscript.

Conflicts of interest

There are no conflicts to declare.

Acknowledgements

Notes and references

Supporting Information

Synthetic procedures and copies of ^1H NMR data for all novel compounds (PDF). In silico bioavailability predictions.

W. Alcazar, S. Alakurtti, M. Padrón-Nieves, ML, Tuononen, N. Rodríguez, J. Yli-Kauhaluoma and A. Ponte-Sucre, *Microorganisms,* 2021, **9,** 320.

ARTICLE

M. Amaral, F.S. Sousa, T.A.C. Silva, A.J.G. Junior, N.N. Taniwaki, D.M. Johns, J.H.G. Lago, E.A. Anderson, A.G. Tempone, *Sci Rep.*, 2019, **9,** 6114.

Baell JB, *J. Nat. Prod.*, 2016, **79**, 616-628.

Baragaña B, Norcross NR, Wilson C, Porzelle A, Hallyburton I, Grimaldi R, Osuna-Cabello M, Norval S, Riley J, Stojanovski L, Simeons FR, Wyatt PG, Delves MJ, Meister S, Duffy S, Avery VM, Winzeler EA, Sinden RE, Wittlin S, Frearson JA, Gray DW, Fairlamb AH, Waterson D, Campbell SF, Willis P, Read KD, Gilbert IH, *J. Med. Chem.*, 2016, **59**, 9672-9685.

Benaim G, Paniz-Mondolfi AE, Sordillo EM, Martinez-Sotillo N., *Front. Cell Infect. Microbiol.*, 2020, **10**, 1-15.

Brindha J, Balamurali MM, Chanda K., *Front. Chem.*, 2021, **9**:622286.

Chang KP, Nacy CA, Pearson RD., *Methods Enzymol.,* 1986, **132,** 603-626.

Chicharro C, Granata C, Lozano R, Andreu D, Rivas L., *Antimicrob. Agents Chemother.*, 2001, **45**, 2441-2449.

Costa-Silva TA, Grecco SS, Sousa FS, Lago JH, Martins EG, Terrazas CA, Varikuti S, Owens KL, Beverley SM, Satoskar AR, Tempone AG., *J. Nat. Prod.*, 2015, **78,** 653–657.

Das A, Jawed JJ, Das MC, Sandhu P, De UC, Dinda B, Akhter Y, Bhattacharjee S., *Int. J. Antimicrob. Agents*, 2017, **50**, 512-522.

Davis RL., *iScience,* 2020, **23**, 101487.

Don R, Ioset JR., *Parasitology,* 2014, **141,** 140-146.

Ferreira DD, Sousa FS, Costa-Silva TA, Reimão JQ, Torrecilhas AC, Johns DM, Sear CE, Honorio KM, Lago JHG, Anderson EA, Tempone AG., *Eur. J. Med. Chem.*, 2019, **176,** 162-174.

Garcia FP, Lazarin-Bidóia D, Ueda-Nakamura T, Silva SO, Nakamura CV, *Evid. Based Complement. Alternat. Med.*, 2013, **2013,** 940531.

Grecco SS, Costa-Silva TA, Jerz G, Sousa FS, Alves Conserva GA, Mesquita JT, Galuppo MK, Tempone AG, Neves BJ, Andrade CH, Cunha RL, Uemi M, Sartorelli P, Lago JH, *Phytomedicine,* 2017a, **24,** 62-67.

Grecco SS, Costa-Silva TA, Jerz G, Sousa FS, Londero VS, Galuppo MK, Lima ML, Neves BJ, Andrade CH, Tempone AG, Lago JHG., *Chem. Biol. Interact.*, 2017b, **277,** 55-61.

Grecco SS, Martins EG, Girola N, Figueiredo CR, Matsuo AL, Soares MG, Bertoldo BC, Sartorelli P, Lago JH., *Pharm. Biol.*, 2015, **53,** 133–137.

Hailu T, Yimer M, Mulu W, Abera B., *J. Vector Borne Dis.*, 2016, **53,** 193-198.

Han Y, Zhang J, Hu CQ, Zhang X, Ma B, Zhang P., *Front. Pharmacol.,* 2019, **10**, 434.

Jain V, Jain K., *Drug Discov. Today,* 2018, **23**, 161-170.

Katsuno K, Burrows JN, Duncan K, Hooft van Huijsduijnen R, Kaneko T, Kita K, Mowbray CE, Schmatz D, Warner P, Slingsby BT., *Nat. Rev. Drug Discov.*, 2015, **14**, 751-758.

Kirchmair, J., Göller, A., Lang, D. Kunze, J., Testa, B., Wilson, I., Glen, R., Schneider, G., *Nat. Rev. Drug Discov.,* 2015, **14**, 387–404.

Lee SM, Kim MS, Hayat F, Shin D., *Molecules,* 2019, **24**, 1-45.

Lejay A, Charles AL, Zoll J, Bouitbir J, Thaveau F, Piquard F, Geny B. *Muscle Biopsy,* 2012, **2012,** 133-154.

Lipinkski CA, Lombardo F, Dominy BW, Feeney PJ. *Adv. Drug Del. Rev.,* 1997, **23**, 3-25.

Loría-Cervera EN, Andrade-Narvaez F., *Acta Trop.,* 2020, **207,** 105456.

Meade JC, *Parasite,* 2019, **26**, 69.

Menna-Barreto, R.F.S., Castro, S.L., *BioMed. Res. Int.*, 2014, **2014,** 1-14.

Moo-Young, M. (Ed.). *Comprehensive Biotechnology* (2ª ed). Academic Press, 2011.

Monteiro-Neto V, Souza CD, Gonzaga LF, Silveira BC, Sousa NCF, Pontes JP, Santos DM, Martins WC, Pessoa JFV, Carvalho Júnior AR, Almeida VSS, Oliveira NMT, Araújo TS, Maria-Ferreira D, Mendes SJF, Ferro TAF, Fernandes ES., *PLoS One,* 2020, **15**:e0232987.

Newman DJ, Cragg GM., *J. Nat. Prod.*, 2020, **83**, 770-803.

Pinto-Martinez AK, Rodriguez-Durán J, Serrano-Martin X, Hernandez-Rodriguez V, Benaim G., *Antimicrob. Agents Chemother.*, 2018, **62**:e01614-17.

Rajendran M, Dane E, Conley J, Tantama M. *Biol. Bull.*, 2016, **231**, 73-84.

Ramakrishnan, S, Docampo, R., *Genes,* 2018, **9**,304.

Scarpelli, PH, Pecenin, MF, Garcia, CRS. *Int. J. Mol. Sci.*, 2021, **22,** 1-12.

Sear, EC, Pieper, P, Amaral, A, Romanelli, MM, Costa-Silva, TA, Haugland, MM, Tate, JA, Lago, JHG, Tempone, AG, Anderson, EA. *ACS Infect. Dis.,* 2020, **6**, 2872-2878.

Stauber, LA, Franchino, EM, Grun, J. *J. Protozool.*, 1958, **5**, 269-273.

Sundar, S, Singh, B. *Expert Opin. Ther. Targets,* 2018, **22**,467-486.

Tada, H, Shiho, O, Kuroshima, K, Koyama, M, Tsukamoto, M. *J Immunol. Methods*, 1986, **93**,157-165.

Tempone, AG, Melhem, MSC, Prado, FO, Motoie, G, Hiramoto, RH, Antoniazzi, MM, Haddad, CFB, Jared, C. *Lett. Drug Des. Discov.,* 2007, **4**, 67-73.

Tiwari, N, Gedda, MR, Tiwari, VK, Singh, SP, Singh, RK. *Mini Rev. Med. Chem.* 2018, **18**, 26-41.

Van de Waterbeemd, H, Gifford, E. *Nat. Rev. Drug Discov.*, 2003, **2,** 192-204.

Venkatesh, M, Barathi, VA, Goh, ETL, Anggara, R, Fazil, MHUT, Ng AJY, Harini, S, Aung, TT, Fox, SJ, Liu, S, Yang, L, Barkham, TMS, Loh, XJ, Verma, NK, Beuerman, RW, Lakshminarayanan, R. *Antimicrob. Agents Chemother.,* 2017, **61**, e469-417.

World Health Organization. Integrating neglected tropical diseases into global health and development: fourth WHO report on neglected tropical diseases. Geneva; 2017.

Xiong G, Wu Z, Yi J, Fu L, Yang Z, Hsieh C, Yin M, Zeng X, Wu C, Lu A, Chen X, Hou T, Cao D. *Nuc. Acids Res.,* 2021, **49**, W5-W14.

Synthesis and characterization of Fe$_3$O$_4$@SiO$_2$@PDA@Ag core–shell nanoparticles and biological application on human lung cancer cell line and antibacterial strains

Snigdha Singh, Tanya Goel, Aarushi Singh, Heerak Chugh, Nayanika Chakraborty, Indrajit Roy, Manisha Tiwari & Ramesh Chandra

Published online: 29 Dec 2023.

Submit your article to this journal ↗

Article views: 17

View related articles ↗

View Crossmark data ↗

Taylor & Francis
Taylor & Francis Group

🔓 OPEN ACCESS | Check for updates

Synthesis and characterization of Fe₃O₄@SiO₂@PDA@Ag core–shell nanoparticles and biological application on human lung cancer cell line and antibacterial strains

Snigdha Singh[a] iD, Tanya Goel[a,b†], Aarushi Singh[a,c†], Heerak Chugh[a], Nayanika Chakraborty[a], Indrajit Roy[a], Manisha Tiwari[b] and Ramesh Chandra[a,b] iD

aDepartment of Chemistry, University of Delhi, Delhi, India; bDr. B. R. Ambedkar Center for Biomedical Research, University of Delhi, Delhi, India; cMax Planck Institute for Multidisciplinary Sciences, Göttingen, Germany

ABSTRACT

Novel magnetic and metallic nanoparticles garner much attention of researchers due to their biological, chemical and catalytic properties in many chemical reactions. In this study, we have successfully prepared a core–shell Fe₃O₄@SiO₂@PDA nanocomposite wrapped with Ag using a simple synthesis method, characterised and tested on small cell lung cancer and antibacterial strains. Incorporating Ag in Fe₃O₄@SiO₂@PDA provides promising advantages in biomedical applications. The magnetic Fe₃O₄ nanoparticles were coated with SiO₂ to obtain negatively charged surface which is then coated with polydopamine (PDA). Then silver nanoparticles were assembled on Fe₃O₄@SiO₂@PDA surface, which results in the formation core–shell nanocomposite. The synthesised nanocomposite were characterized using SEM-EDAX, dynamic light scattering, XRD, FT-IR and TEM. In this work, we report the anticancer activity of silver nanoparticles against H1299 lung cancer cell line using MTT assay. The cytotoxicity data revealed that the IC₅₀ of Fe₃O₄@SiO₂@PDA@Ag against H1299 lung cancer nanocomposites cells was 21.52 μg/mL. Furthermore, the biological data of nanocomposites against Gram-negative 'Pseudomonas aeruginosa' and Gram-positive 'Staphylococcus aureus' were carried out. The range of minimum inhibitory concentration was found to be 115 μg/mL where gentamicin was used as a standard drug. The synthesized AgNPs proves its supremacy as an efficient biomedical agent and AgNPs may act as potential beneficial molecule in lung cancer chemoprevention and antibacterial strains.

KEY MESSAGES

1. In the present study, we have successfully prepared a core-shell Fe₃O₄@SiO₂@PDA@Ag nanocomposite.
2. We have investigated the dose-dependent cellular toxicity of silver nanocomposite in the nonsmall cell lung cancer cell line H1299 using MTT assay.
3. Also, we have evaluated the mode of cell death using apoptosis.
4. We have also evaluated the bioactivity of AgNPs on both Gram-positive and Gram-negative bacterial cells with highly efficient antibacterial potency.

GRAPHICAL ABSTRACT
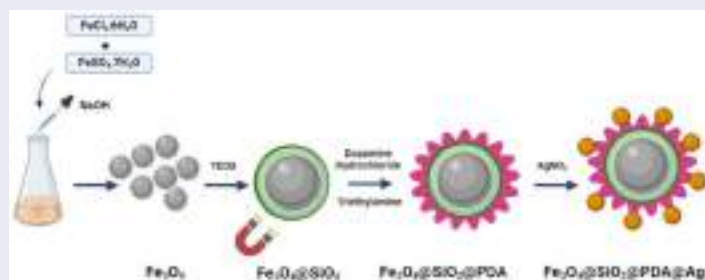
1. Introduction

Lung cancer is dominant and second most commonly diagnosed cancer among men and women which is largely widespread around the globe. It has a high morbidity and mortality rates worldwide, causing 1.8 million deaths [1]. However, the nanoparticles have proven as an effective tools

from its diagnosis to cancer therapy [2]. The size of synthetic nanoparticle derived from polymers, metals etc. having a diameter of <100 nm are particularly useful as size is similar to most of the biological structures and molecules. Hence, they confer functional properties for both *in vitro* and *in vivo* cancer research [3]. Silver NPs (AgNPs) show significant features like high catalytic activity, chemical stability, easy fabrication, good conductivity and potential therapeutical application such as antibacterial [4], anticancer [5,6], anti-inflammatory activities [7,8], nanoelectronic devices, water purification, and environmental pollution control [9,10]. Despite from other metal nanoparticles, silver nanoparticles are nontoxic at lower dosage for a human body [11,12]. The high surface to volume ratios of silver nanoparticles have high reactivity and hence provide its usage in biomedical applications. Recently, core shell AgNPs has been studied for effective gene delivery and it showed that it can completely condensate DNA and protect it from degradation [13]. Also hybrid $Fe_3O_4@$ AgNPs were synthesised *via* green route and demonstrated selective cytotoxicity against tumour cell line [14]. Silver nanoparticles (AgNPs) have now been recognised as significant class of nanomaterials for various biomedical applications and more attention are focused on AgNPs because they have risen up as promising therapeutic molecule in cancer treatment [15]. AgNPs have exhibited potential cytotoxicity against various cancer cell lines like lung cancer A549 [16–18], Hela cells [19], breast cancer MCF-7 cells [20–22] and so on. Furthermore, as we all are aware that bacterial infections are major threat to public health globally. Several nanocomposites based on Au [23], Ag [24,25], Cu [26,27] and ZnO [28] have been used as antibacterial agents [29]. As we know, various processes have now been established to synthesise highly dispersed AgNPs using solution based methods, therefore in order to address this challenge, increasing efforts has been aimed towards AgNPs introduction on solid supports (polymers, metal oxides) using different nanostructures like spheres, mesoporous silica to generate composite catalysts, which could be the best approach to avoid aggregation of small-sized AgNPs without affecting properties [30,31].

A new trend in field of material sciences is coating of materials and modifying their surface which can provide novel surface functionalities and properties [32]. Recently, three layered core-shell nanocomposites have gained much attention in cancer application. Among the other preferred carrier materials, silica coated with Fe_3O_4 magnetic carrier have emerged as a powerful catalytic support as they have excellent thermal stability, low toxicity, ease of synthesis, effortless separation from the reaction through external magnetic sources [33]. The SiO_2 core have some advantages like ease in controlling particle size, high colloidal stability and has potential application in drug delivery and biosensors [34,35]. However, the surface properties of silica nanoparticles have been found tuneable for various purposes like multi-functionalization, drug loading, drug release and delivery [36]. Usually, a nanomaterial using Fe_3O_4 core and SiO_2 shell has a good magnetic response and chemically modifiable surface. Polydopamine (PDA) has been

extensively used as a versatile functionalization tool since 2007, having been inspired by adhesive nature of amines and catechols in mussel adhesive proteins [37]. These PDA could self-polymerize and form PDA layers which can be subsequently applied to variety of substrates to improve biocompatibility and to tolerate other bio-functionalization [38,39]. PDA can readily be deposited under slightly basic conditions by dopamine polymerization, to form a biocompatible layer that will stick to range of material surfaces [40,41]. The metallic nanoparticles like Ag, Au Pd in combination with other metal oxides like (SiO_2, TiO_2), polymer matrices like polyaniline, PDA, pyrrolidone, polypyrrole have been exponentially explored due to high conductivity, thermal stability and redox potential nanocomposites [42].

Recently, Zhang et al. [43] reported the green synthesis of AgNPs decorated on $Fe_3O_4@PDA$ as effective antimicrobial agents. Wang et al. [44] have synthesised PDA coated magnetic nanocellulose AgNP for inactivation of *E. coli* bacteria in waste water. Nikmah et al. [45] have reported the synthesis of $Fe_3O_4@SiO_2@Ag$ nanocomposites and promising antibacterial activity using agar diffusion method. Baoliang et al. [46] have reported a composite of $Fe_3O_4@SiO_2@Ag$ and their application in Surface enhanced Raman Scattering. Similarly, novel cube like $Fe_3O_4@SiO_2@Au@Ag$ magnetic nanocomposites have been reported as efficient SERS substrate for pesticide detection [47]. Here, $Fe_3O_4@SiO_2@PDA$ core has been used as the support for Ag nanoparticles. In order to improve the biocompatibility of the nanoplatform, for the first time we report the fabrication and characterization of the synthesised '$Fe_3O_4@SiO_2@PDA@Ag$' nanocomposites where SiO_2 nanoparticles were synthesised by hydrolysis of TEOS followed by thermal decomposition and its used as core for synthesis for core–shell nanoparticles. Various studies reveal that Ag nanocomposites decorated with ferrite-silica core have the potential to destroy cancer cells without affecting the normal cells. Therefore, in the present study, we have investigated the dose-dependent cellular toxicity of silver nanocomposite in the non-small cell lung cancer cell line H1299 by the MTT. Also we have evaluated the mode of cell death using apoptosis. We have also evaluated the bioactivity of AgNPs on both Gram-positive and Gram-negative bacterial cells with highly efficient antibacterial potency and can be exploited as drugs next door in potential healthcare settings.

2. Experimental

2.1. Materials and reagents

$FeCl_3.6H_2O$ was purchased from Central Drug House Pvt. Ltd, $FeSO_4.7H_2O$, tetraethyl orthosilicate (TEOS) from Sigma Aldrich. The ethyl alcohol (C_2H_5OH, 95 %), and aqueous ammonia (25 wt %) were supplied by SRL Co., Ltd. All chemical reagents were directly used without further purification. MTT dye was purchased from Sigma Aldrich. Double deionised water was used throughout the study. All reagents were used without purification.

2.2. Synthesis of ferrite (Fe$_3$O$_4$) nanoparticles

Initially, FeCl$_3$.6H$_2$O, 6.0 g and FeSO$_4$.7H$_2$O, 4.2 g were dissolved in 250 ml of deionised water and were allowed to stir at 50 °C until appearance of yellow-orange solution. After, we added 25% ammonium hydroxide dropwise to slowly adjust the pH to 10 and then the mixture was allowed to stir for another 1h at 50 °C [48]. The ferrite nanoparticles were precipitated as a black material which was separated by an external magnet and washed several times with water and ethanol. This was dried overnight in oven at 50 °C to obtain the nanoparticles.

2.3. Synthesis of Fe$_3$O$_4$@SiO$_2$

The SiO$_2$ coating over ferrite nanoparticles was done using sol–gel approach. A suspension of 0.5 g of ferrite nanoparticles and 0.1 M HCl (2.2 ml) was prepared in water (50 ml) and ethanol (200 ml) mixture under sonication for 1 h at RT. After, 25 % NH$_4$OH (5 ml) was added to the mixture followed by dropwise addition of TEOS (1 ml) and resulting mixture was stirred at 50 °C for 6 h. The resulted silica coated magnetic nano particles Fe$_3$O$_4$@SiO$_2$ were separated magnetically and washed with ethanol and water several times and then dried in oven at 40 °C.

2.4. Synthesis of Fe$_3$O$_4$@SiO$_2$@PDA

The Fe$_3$O$_4$@SiO$_2$ nanoparticles (0.18 g) were dispersed *via* sonication into ethanol (100 ml) for half hour. Then dopamine hydrochloride (100 mg) and triethylamine (74 μL) were added to the reaction mixture. The mixture was then stirred at 50 °C for 24 h and then nanoparticles were purified by three wash cycles of centrifugation/redispersion in ethanol [32,49].

2.5. Synthesis of Fe$_3$O$_4$@SiO$_2$@PDA@Ag

Fe$_3$O$_4$@SiO$_2$@PDA nanospheres (100 mg) were dispersed in 100 ml water. In another beaker, dissolve 50 mg silver nitrate in 100 ml water. Mix the above two solutions and allowed to stir for 24 h. The mixture was washed with water and ethanol several times and then dried at 50 °C

3. Characterization of synthesised Fe$_3$O$_4$@SiO$_2$@PDA@Ag

3.1. Electron microscopy

To determine the size and morphology of synthesised nanocomposite, Fe$_3$O$_4$@SiO$_2$@PDA@Ag was subjected to transmission electron microscopy using TEM (TALOSTEM from Thermo Scientific). For TEM analysis, carbon-coated Cu grids were used, and the sample was deposited on them using the drop-casting method. Image J software was used to calculate the average size of nanoparticles.

0.5 mg of nanocomposite was diluted with 70% ethanol (1 ml), sonicated for 30 min before placing onto carbon coated copper grid.

The Fe$_3$O$_4$@SiO$_2$@PDA@Ag was subjected to FESEM-EDAX using Zeiss GeminiSEM 500 thermal field emission type microscope.

3.2. Particle size and zeta potential

Nanoparticle samples were dispersed, sonicated for 5 min in milliQ water and 1 ml of this was taken in quartz cuvette before analysis. The particle size was measured using dynamic light scattering (DLS), Nanoplus particle size analyser from Particulate Systems and surface charge measurement of nanocomposite were measured by Zetasizer Nano-ZS (Malvern Intsruments, UK). All measurements were carried out in triplicate ($n = 3$).

3.3. Fourier-transforms infra-red (FT-IR) spectroscopy

FTIR was performed using Shimadzu II FT-IR Spectrometer. In brief, spectrum for physical mixture of Fe$_3$O$_4$, Fe$_3$O$_4$@SiO$_2$ and Fe$_3$O$_4$@SiO$_2$@PDA as well as Fe$_3$O$_4$@SiO$_2$@PDA@Ag was recorded.

3.4. Powder X-ray diffraction pattern (PXRD)

The polymorphic state of the drug in lipid matrix was confirmed using Rigaku Ultima IV X-ray Diffractometer. The Ni-filtered, Cu Kα-radiation, voltage of 40 Kv and current of 40 mA was used. The scanning rate was 1°/min over 10 °–50° diffraction angle (2θ) range. The crystal lattice of Fe$_3$O$_4$@SiO$_2$@PDA@Ag was accounted.

3.5. Stability data

The stability analysis of Fe$_3$O$_4$@SiO$_2$@PDA@Ag nanocomposites was performed using DLS measurements at different time intervals. The suspension of AgNPs were kept at 4 °C and size measurements at different time intervals was observed using DLS at 1, 7, 14, and 21 days. Also, we have prepared the suspension of AgNPs in different PBS buffers (neutral, acidic and basic) and size was recorded [50,51].

4. Cellular experiments

Human lung adenocarcinoma H1299 cancer cells were purchased from the Cell Bank of Type Culture Collection of ACBR and cultured in DMEM supplemented with 10% foetal bovine serum and 1% penicillin/streptomycin in a cell culture incubator maintained under a 5% CO$_2$ atmosphere at 37 °C.

Gram positive 'Staphylococcus aureus' (S. aureus, MTCC 741) and Gram negative 'Pseudomonas aeruginosa' (P. aeruginosa) were the microbes used in this study. Both S. aureus and P. aeruginosa were grown and cultured in Brain Heart Infusion (BHI) media procured from HiMedia at 37 °C and 180 rpm for 12 h. Furthermore, pure colony of these bacteria were collected with a sterile inoculating loop from agar plate and sub cultured in BHI broth and stored at 4 °C for future experimental purpose.

4.1. MTT assay

H1299 lung adenocarcinoma cell line was cultured in DMEM supplemented with 10% foetal bovine serum (FBS) and 1% antibiotics penicillin and streptomycin (100 μg/mL). Cells were maintained in humidified incubator at 5% CO_2 and 37 °C. Cells were passaged and harvested at ∼80% confluency; they were seeded in 96 well plates at a cellular density of 7×10^3 cells per well. The seeded cells were grown overnight and treated with various concentrations of $Fe_3O_4@SiO_2@PDA$ and $Fe_3O_4@SiO_2@PDA@Ag$ nanocomposites in triplicates. A 2 mg/mL stock solution of $Fe_3O_4@SiO_2@PDA$ and $Fe_3O_4@SiO_2@PDA@Ag$ was prepared in MilliQ water and sonicated to achieve a homogenised solution. Carefully calculated amount of the nanocomposite was added to the 96 well plates for the following final concentrations- 5, 10, 20, 40, 60, 80, 100 μg/mL. The plates were then incubated at 37 °C, 5% CO_2 humidified incubator for 48 h. Post-incubation, the effect of $Fe_3O_4@SiO_2@PDA$ and $Fe_3O_4@SiO_2@PDA@Ag$ nanocomposite was evaluated using a freshly prepared Methylthiazolyldiphenyl-tetrazolium bromide (MTT) solution at a final concentration of 0.5 mg/mL each well. Next, 100 μl of DMSO was added to each well to dissolve the formazan crystals and reading was taken using a multiplate reader at 570 nm and reference at 630 nm.

$$\% \text{ Viability } = \text{ Average reading at 570nm}/ $$
$$\text{Average reading of control at 570 nm } * 100$$

4.2. Apoptosis

The mode of cell death upon treatment with $Fe_3O_4@SiO_2@PDA@Ag$ on H1299 cancer cell line was determined using Flow cytometer. The Annexin-FITC Apoptosis Detection Kit was used and the protocol was followed as per the manufacturer's protocol. In brief, H1299 cells were seeded separately in six-well cell culture with a total concentration of about 1×10^5 cells per well. Cells were grown for 24 h in DMEM medium containing 10% FBS prior to all experiments. The dosing solution was prepared in MilliQ the concentration close to IC_{50} of $Fe_3O_4@SiO_2@PDA@Ag$ was added to the well. Sample were incubated with cultured H1299 cells for 48 h. After predetermined incubation period, the treated cells were extensively rinsed with ice-cold PBS and harvested with Trypsin-EDTA, followed by centrifugation and washing with ice-cold PBS twice and incubated with Annexin/PI dye for 30 min. Then the analyses of the samples were performed on a flow cytometer at FL1 (FITC) and FL2 (PI) channels using BD FACS CALIBUR™. And data was further analysed using Cell Quest pro software.

4.3. Minimum inhibitory concentration (MIC)

MIC test is widely used in clinical microbiology as it provides the lowest concentration of the test antimicrobial agent required to inhibit the visible growth of the microorganism. In a 96-well sterile microtitration plate (Corning), we performed this microbroth dilution procedure with escalating dosages of the as-synthesised $Fe_3O_4@SiO_2@PDA@Ag$ nanocomposites. The final volume of 200 μL was achieved with 10 μL of mid-log phase bacterial inoculum and BHI broth with the desired nanoparticle concentration. Wells with only media and *S.aureus* or *P.aeruginosa* served as growth controls. The 96-well microtitration plates after inoculation was subjected to well-mixing and incubated in incubator shaker at 180 rpm and 37 °C for 16–18 h. The growth of the treated cells was monitored by measuring the absorbance at 600 nm in the TECAN Infinite M200 Pro, micro-plate reader.

4.3.1. SEM analysis of bacterial cell rupture on P. Aeruginosa cells

The structural changes in the bacterial morphology induced by as-synthesised $Fe_3O_4@SiO_2@PDA@Ag$ nanocomposites were examined by Scanning Electron Microscopy. *Pseudomonas aeruginosa* was grown overnight at 37 °C under aerobic conditions. Then,10^6 CFU/mL of the fresh cultures was used to carry out subsequent experiments. The bacterial suspensions were centrifuged at 4000 rpm for 10 min to separate bacterial pellets. The aqueous dispersion of nanoparticles (at MIC value) was incubated with freshly prepared culture of *P. aeruginosa*. The pellet appeared was thoroughly washed with 1X PBS solution (3 × 1 ml). After centrifugation, each bacterial pellet was fixed with 4% paraformaldehyde solution, and the pellet was kept at 4 °C overnight. After centrifugation, again the washing of each pellet was done with 1× PBS (3 × 1 ml). Ultimately, serial dehydration of bacterial cells was carried out by washing with increasing concentrations of ethanol (10%, 20%, 40%, 60%, 80% and 100%). The pellet was dried and deposited on SEM stub for analysis.

4.4. In vitro *Haemolysis assay*

Haemolysis assay was done to ascertain the lytic interactions of as synthesised nanocomposites with the mammalian membrane. The whole blood sample was washed with 1× PBS solution (pH = 7.4) and resuspended in PBS solution. 100 μL of diluted RBC suspension in 1× PBS solution was exposed to various 100 μL of the nanoparticle suspension at concentration of 100, 250, 350, 450, 550 and 650 μg/mL (test group), PBS (positive group), and 1% TritonX-100 (negative group). After incubation at 37 °C for 1 h and centrifugation for 5 min at 800 g, the supernatant of all samples was transferred to a 96-well plate and the absorbance was measured by a microplate reader (BioTek 800 TS absorbance reader) at 405 nm. The percent haemolysis was expressed by the following formula and plotted as a function of percent haemolysis with concentration (μg/mL):

$$\% \text{ Haemolysis } = \frac{\text{OD (test)} - \text{OD (negative)}}{\text{OD (positive)} - \text{OD (negative)}} \times 100$$

5. Result and discussion

5.1. Characterization of synthesised $Fe_3O_4@SiO_2@PDA@Ag$

5.1.1. Electron microscopy

The TEM images suggested that particles were roughly spherical in shape as show in the figure below at 50 nm scale with

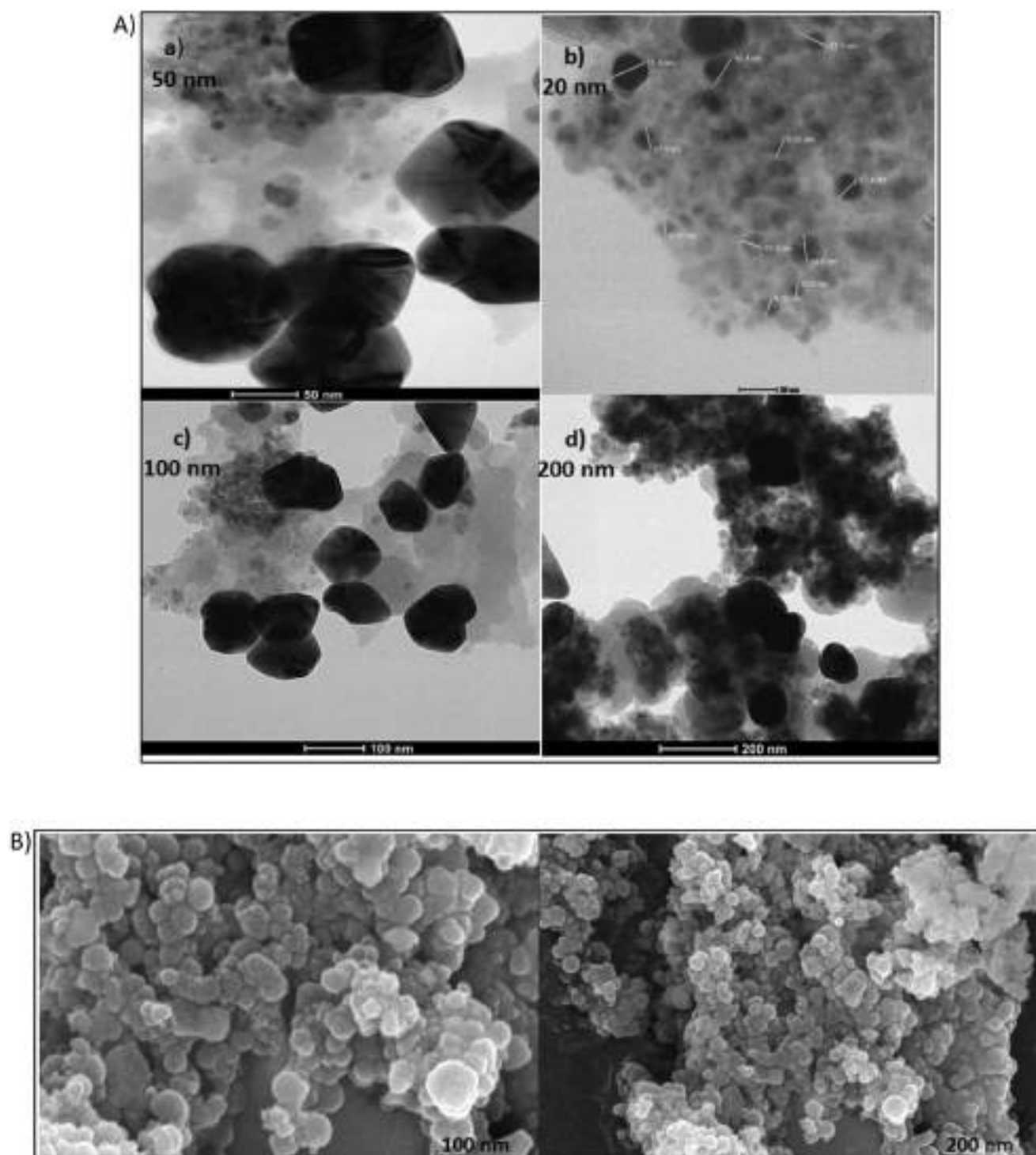**Figure 1.** (a) TEM image of synthesised Fe_3O_4@SiO_2@PDA@Ag nanocomposite.
(a) 50 nm (b) 20 nm (c) 100 nm (d) 200 nm. (**b**) Fe-SEM image of synthesised Fe_3O_4@SiO_2@PDA@Ag nanocomposite (a)100 nm (b) 200 nm (c) Elemental mapping image of synthesised Fe_3O_4@SiO_2@PDA@Ag nanocomposite.

the size ranging from 10 to 30 nm (Figure 1). However, TEM image at 100 nm suggested that the nanocomposites are present in chain-like confirmation.

5.1.2. DLS and zeta potential
The formation of Fe_3O_4@SiO_2@PDA@Ag was established by DLS study and the results revealed the hydrodynamic size of the nanostructures was found to be $\sim$ 139.1 nm at 25 °C in water as solvent with polydispersity index of 0.237 (Figure 2). This could be due to the aggregation of the nanostructures in water. However, the average size difference in TEM and DLS could be due to the hydrodynamic diameter with swollen nanostructures in DLS [52,53]. The low zeta potential value of 5.02 mV indicates that nanostructures could agglomerate. (Figure 3).

Figure 1. Continued.
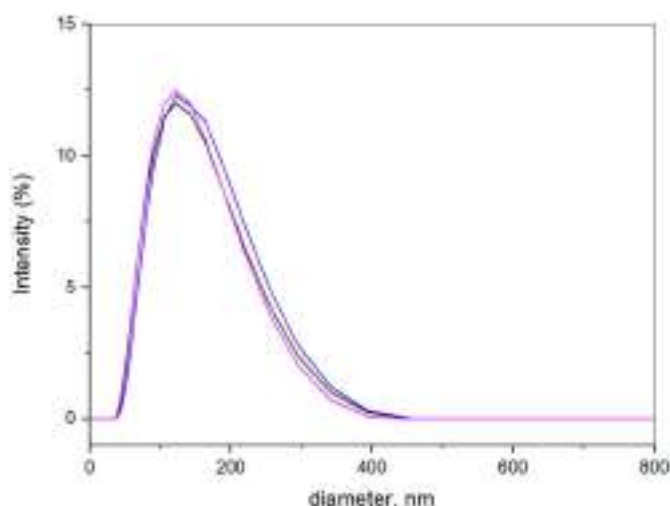
Figure 2. DLS of synthesised Fe$_3$O$_4$@SiO$_2$@PDA@Ag (medium: Water; size, d: 139.1 nm).

5.1.3. FTIR spectra

FT-IR was used to study the successful immobilization of various functionalities at each step of nanocomposite preparation. The stretching frequency of Fe$_3$O$_4$, Fe$_3$O$_4$@SiO$_2$, Fe$_3$O$_4$@SiO$_2$@PDA as well as Fe$_3$O$_4$@SiO$_2$@PDA@Ag have been recorded. The peak at 565 cm^{-1} is attributed to Fe–O vibration of the bulk Fe$_3$O$_4$. The immobilization of the silane on the magnetic nanoparticle surface was confirmed by the appearance of peaks at 455 cm^{-1} corresponding to Si–O–Si bending modes and peak at 1083 cm^{-1} corresponding to Si-O bending. However, the peak at 3385 cm^{-1} is due to O–H stretching vibrations of PDA and the peak displayed at 2372 cm^{-1} corresponds to C–H stretching vibrations. The appearance of peak at 1662 cm^{-1} is attributed to N-H group and the peaks at 1088 is associated with C-N stretching [53]. Hence, FT-IR spectra postulated that Fe$_3$O$_4$, SiO$_2$ and PDA persisted its characteristics in the lipid matrix (Figure 4).

5.1.4. Powder X-ray diffraction (PXRD) pattern

In order to determine the chemical composition of the so-formed nanocomposites, XRD analysis of Fe$_3$O$_4$, @SiO$_2$@PDA@Ag was carried out. The peaks at 30.32^o, 35.58^o, 46.19^o, 57.33^o, 62.86^o indicates the presence of magnetite nanoparticles. The position and relative intensities of all the peaks in the XRD pattern of Fe$_3$O$_4$@SiO$_2$@PDA@Ag nanocomposite displayed the peaks at 38.11^o, 43.25^o, 62.86^o, 77.46^o that correspond to 111, 200, 220 and 311 planes of Silver nanoparticles [54] (Figure 5).

5.1.5. Elemental analysis

The EDX analysis of Fe$_3$O$_4$@SiO$_2$@PDA@Ag nanocomposite displayed the presence of carbon, nitrogen, oxygen, silicon, silver and Iron in 6.71 wt %, 1.92 wt %, 32.36 wt %,13.49 wt %,11.15 wt % and 34.38 wt %, respectively (Figure 6).
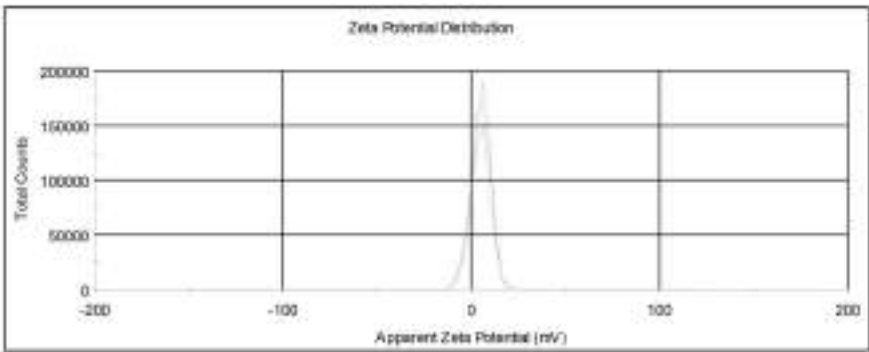
Nanocomposite	Avg. Zeta Potential (mV)	Temp (°C)	Poly Dispersity Index (PDI)	Diameter, d (nm)	Solvent
Fe_3O_4@SiO_2@PDA@Ag	5.02	25	0.237	139.1	Water

Figure 3. Zeta potential distribution image of synthesised Fe_3O_4@SiO_2@PDA@Ag.
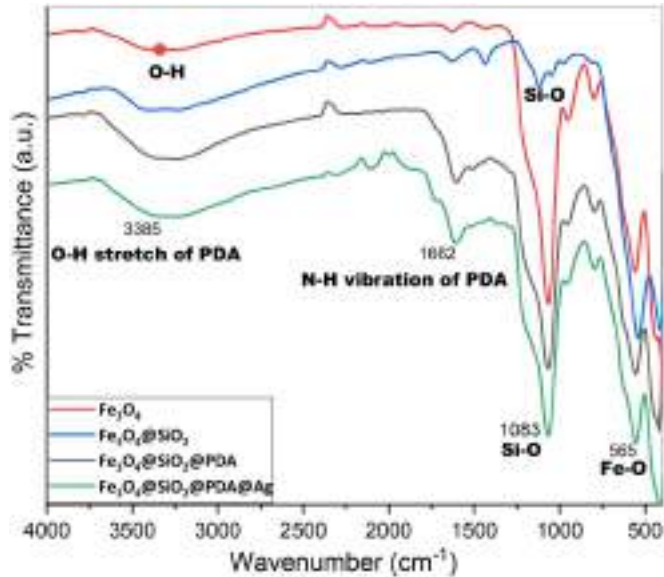
Figure 4. FT-IR of (a) Fe_3O_4, (b) Fe_3O_4@SiO_2, (c) Fe_3O_4@SiO_2@PDA, and (d) Fe_3O_4@SiO_2@PDA@Ag nanocomposite.

Figure 5. XRD of Fe_3O_4@SiO_2@PDA@Ag nanocomposite.

5.2. Stability data of the Fe_3O_4@SiO_2@PDA@Ag nanocomposite

The stability analysis of AgNPs was performed using DLS measurements at different time intervals. The suspension of AgNPs in water were made and kept at 4 °C and size was measured using DLS at 1, 7, 14, 21 days' time intervals. The size of AgNPs in water was found in the range of 120–150 nm. Also, size at different pH was measured and found to be in range of 130–300 nm in pbs and basic buffer, but in acidic buffer size increased to 500 nm after 14 days.

It can be concluded that particles have high stability despite pH and long storage (Figure 7).

5.3. Biological analysis

5.3.1. Evaluation of cytotoxic effect of nanoparticles using MTT assay

MTT assay is among the few preliminary assays to assess the effectiveness or toxicity of small molecules, biomaterials etc. on cultured cells. MTT (3-(4,5-dimethylthiazol-2-yl)-2,5-diphenyltetrazolium bromide)) is a yellow-coloured water-soluble dye that gives purple crystals on its reduction concept on which MTT assay is based upon. In a live cell, cellular respiration produces NADPH which reduces the yellow-coloured dye to purple formazan crystals after incubation; the amount of crystals formed or the amount of colour is directly proportional to levels of NADPH which in turn is proportional to cell viability. The formazan crystals are solubilised in DMSO and measured spectrophotometrically.
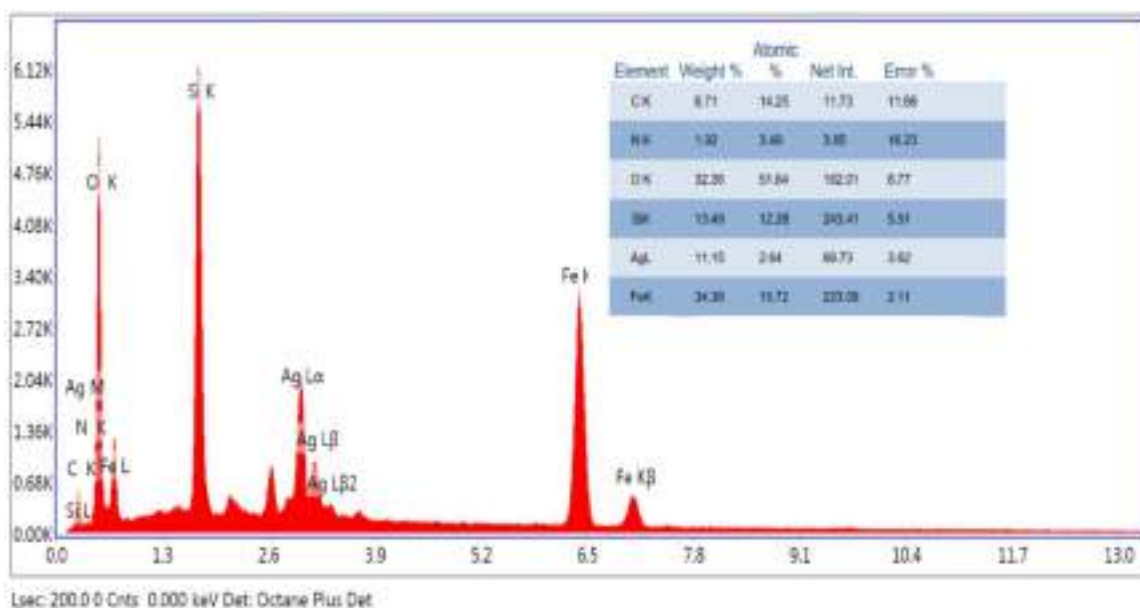
Figure 6. EDAX of $Fe_3O_4@SiO_2@PDA@Ag$ nanocomposite.
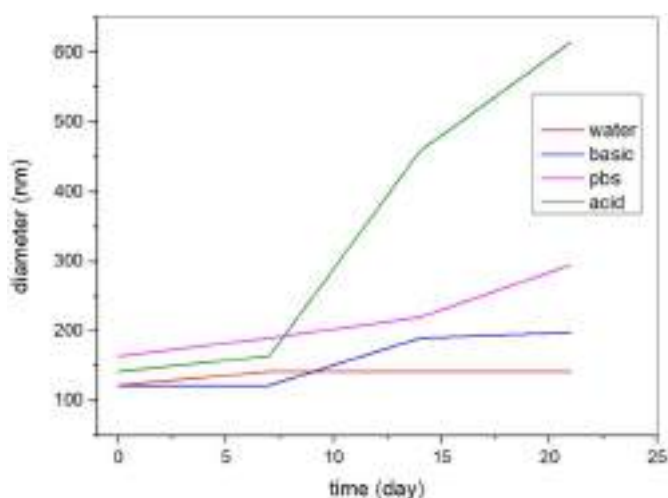
Figure 7. Stability data of $Fe_3O_4@SiO_2@PDA@Ag$ nanocomposite in water, PBS, acidic and basic buffers.

Herein, to assess the anticancer activity of $Fe_3O_4@SiO_2@PDA$ and $Fe_3O_4@SiO_2@PDA@Ag$ nanocomposite in non-small cell lung cancer cell line H1299, each cell line was treated with $Fe_3O_4@SiO_2@PDA$ and $Fe_3O_4@SiO_2@PDA$ @Ag nanocomposite with different concentration—5, 10, 20, 40, 60, 80, 100 µg/mL for 48 h. The % viability was calculated and plotted using the spectrophotometric data for each concentration along with standard deviation (Figure 8). The graphs depict a concentration-dependent effect of $Fe_3O_4@SiO_2@PDA$ and $Fe_3O_4@SiO_2@PDA@Ag$ nanocomposite on H1299 cells lines. The IC_{50} for H1299 were calculated as 62.84 µg/mL for $Fe_3O_4@SiO_2@PDA$. However, the IC_{50} for $Fe_3O_4@SiO_2@PDA@Ag$ nanocomposites were calculated as 21.52 µg/mL. Figure 9 displayed the microscopic images of the effect of the $Fe_3O_4@SiO_2@PDA@Ag$ nanoparticles on H1299 cancer cell line. A large population of nanoparticles (black dots) are internalised by target H1299 cancer cells.

5.3.2. Apoptosis assay of $Fe_3O_4@SiO_2@PDA@Ag$ nanoparticles using Flow cytometry

The mechanism of cell death that occurs in H1299 cells upon treatment with $Fe_3O_4@SiO_2@PDA@Ag$ nanoparticles using Annexin-V FITC/PI dual staining assay was performed, and cells were analysed using FACS. After treatment with increasing concentration for 48 h the apoptosis index in H1299 cells was increased to 21% in early apoptosis & 46 % in late apoptosis at 30 µg/mL (Figure 10).

5.3.2. Evaluation of antibacterial activity of nanoparticles

To comprehend the potency of the $Fe_3O_4@SiO_2@PDA@Ag$ nanocomposites as antibacterial agents, we performed the standard microbroth dilution assay with both Gram-positive and Gram-negative bacteria. The results showed that the nanoparticles were effective in inhibiting the growth of these bacteria at a concentration of 115 µg/mL, for both *S. aureus* and *P. aeruginosa*, indicating another beneficial property of these nanocomposites. This activity could be attributed to the interaction of the nano-sized particles with the larger surface area of the microorganisms. The relative survival percentage of these bacteria is endorsed in Figure 11 as compared to growth controls. It is evident from the findings that the antibacterial propensity of the nanocomposite (due to 11.15 wt% of silver atom) against both Gram-positive or Gram-negative is concentration-dependent. The presence of thick peptidoglycan layer around Gram-positive bacterial cells leads to less suppression in bacterial growth at the same concentration for *S. aureus* as compared to *P. aeruginosa*.

Additionally, the SEM images displayed in Figure 12 demonstrated morphologically induced changes like rupture of the cell membrane, cell shrinkage, aggregation of bacterial cells in $Fe_3O_4@SiO_2@PDA@Ag$ nanocomposites treated samples, whereas in control cells displayed normal, smooth and well-preserved cell membrane. The nanocomposite

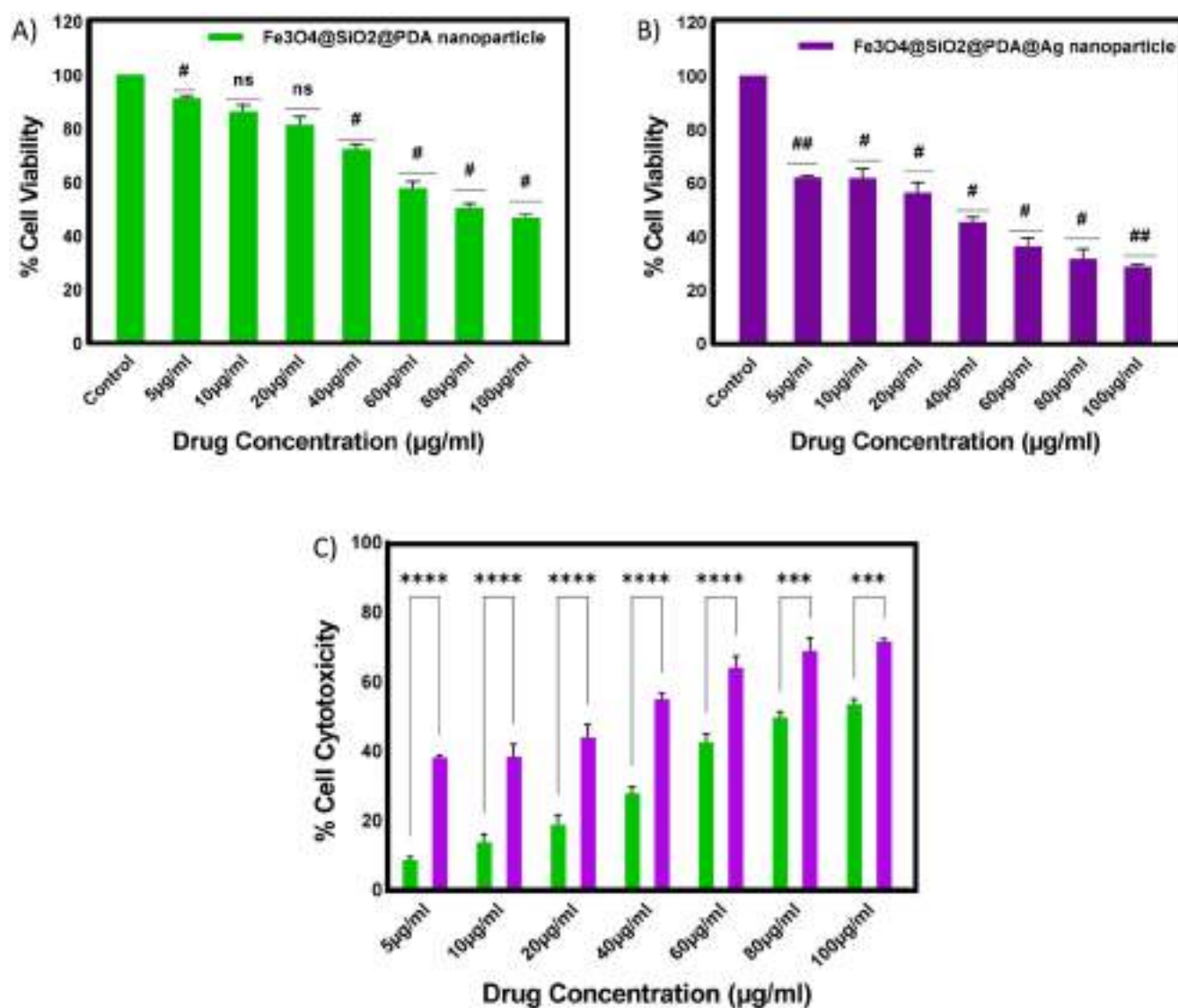**Figure 8.** MTT assay at various concentrations on H1299 cancer cell line; (A) % cell viability of $Fe_3O_4@SiO_2@PDA$ (B) % cell viability of $Fe_3O_4@SiO_2@PDA@Ag$ C) comparison of % cell cytotoxicity of $Fe_3O_4@SiO_2@PDA$ and $Fe_3O_4@SiO_2@PDA@Ag$.
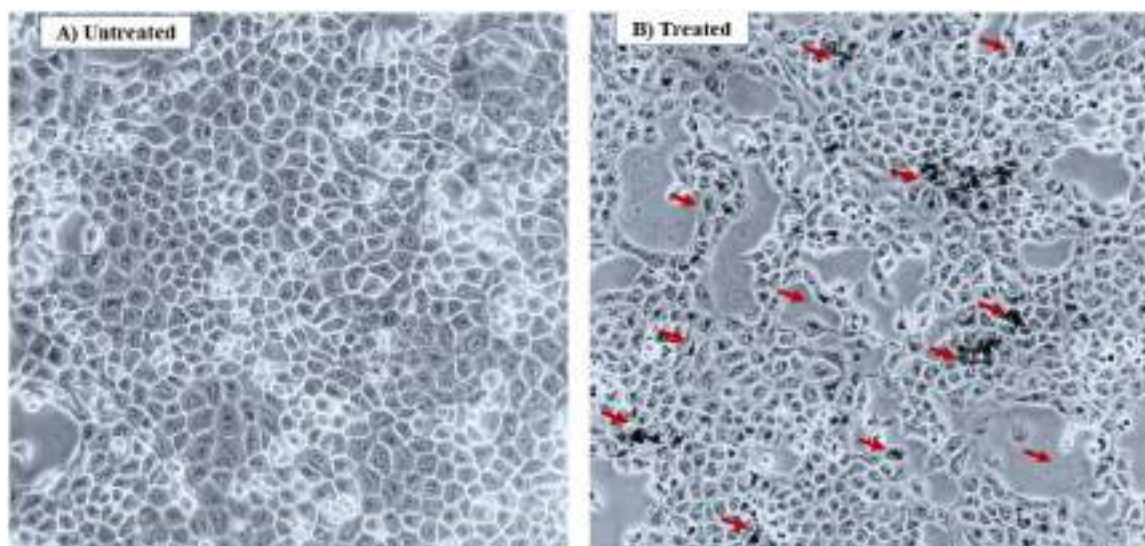

Figure 9. Microscopic images of the effect of the $Fe_3O_4@SiO_2@PDA@Ag$ nanoparticles on H1299 cancer cell line. (A) Untreated/control (B) at 50 μg/mL.
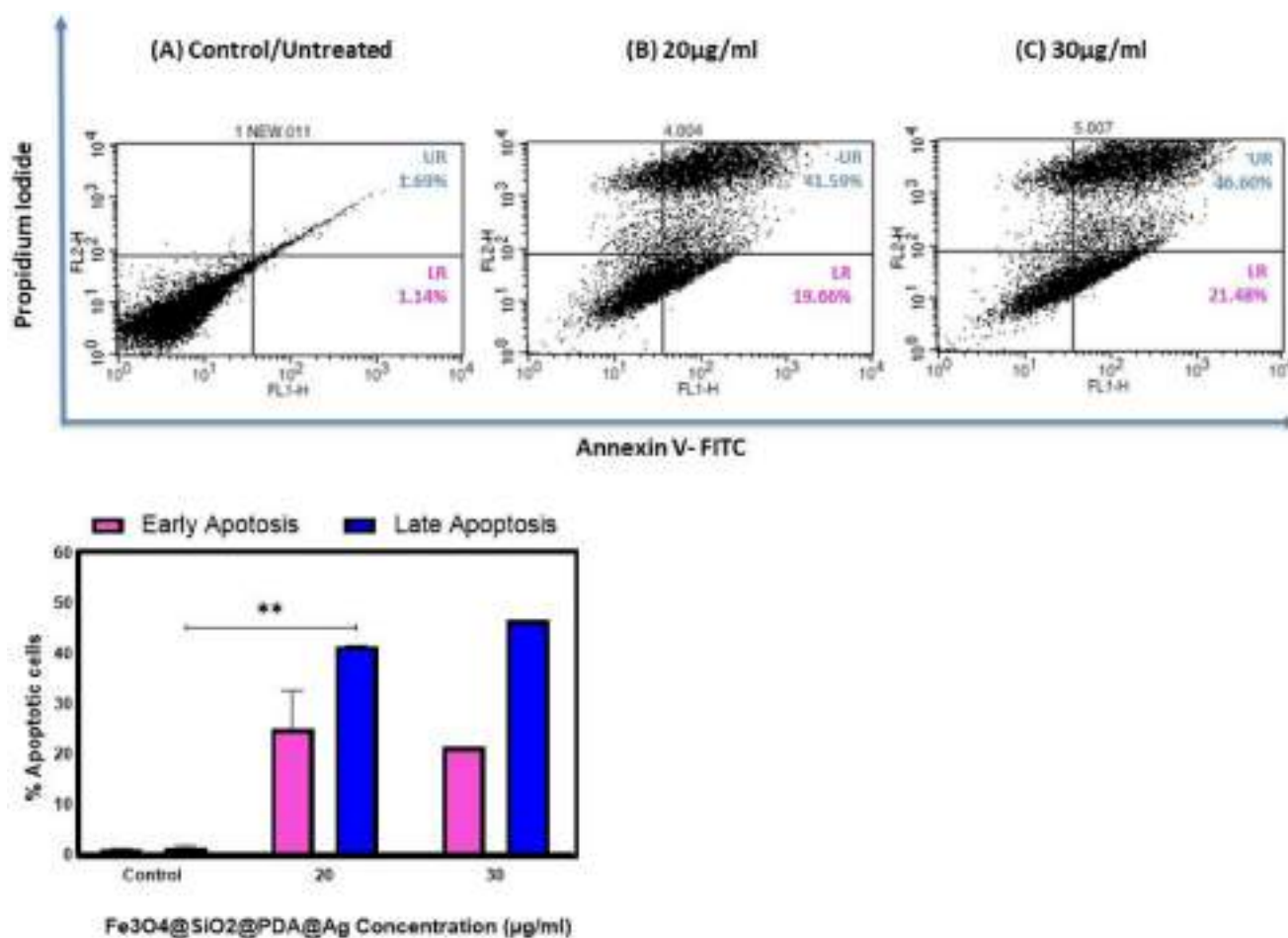
Figure 10. Cell apoptosis assay at different concentrations of $Fe_3O_4@SiO_2@PDA@Ag$ on H1299 cancer cell line (A) control; 0 μg/mL, (B) 20 μg/mL, (C) 30 μg/mL.
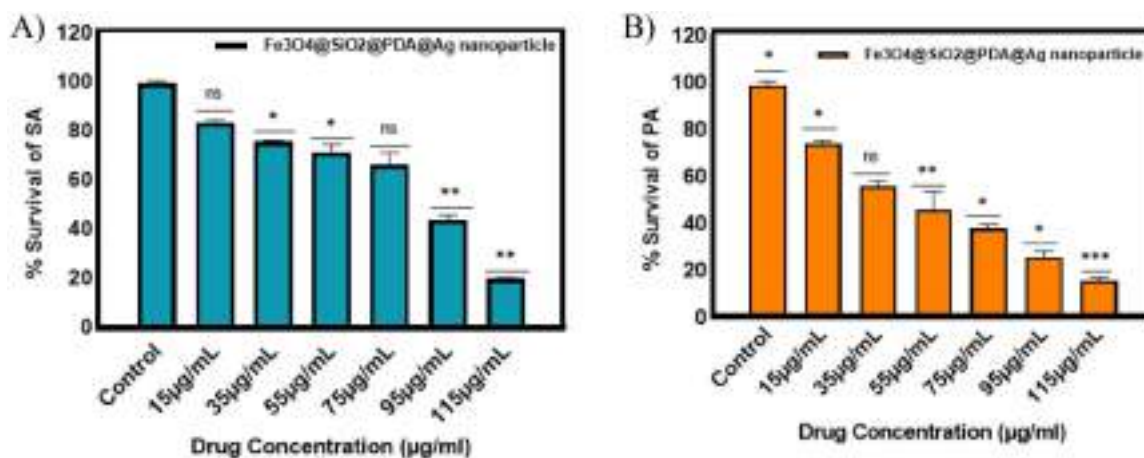
Figure 11. Antibacterial activity of $Fe_3O_4@SiO_2@PDA@Ag$ nanocomposites with increasing concentrations against (A) *S. aureus* and (B) *P. aeruginosa*.

treated cell had deformed and distorted cell structure indicating leakage of intracellular components. SEM images clearly indicated morphological alterations along with complete lysis of the outer membrane of bacteria. EDX analysis also confirmed the presence of strong Ag metallic signals in treated cells. Other signals like Si and Fe were observed due to the $Fe_3O_4@SiO_2$ shell present in the nanocomposite, in addition to the C, N, O present attributed to the bacterial biomolecules.

5.4. In vitro *Haemolysis assay*

Haemolysis study was conducted with 100, 250, 350, 450, 550 and 650 μg/ml concentrations of $Fe_3O_4@SiO_2@PDA@Ag$ nanoparticles. The haemolysis was found to be minimal at a concentration of 100 μg/mL. This concentration is relatively higher than the observed IC_{50} value (21.52 μg/mL) for this nanocomposite. At maximum concentration (650 μg/mL), which was 30 times the observed IC_{50}, the haemolysis was negligible. These

A) Control

B)

Element	Weight %	Atomic %	Net Int.	Error %
C K	54.34	60.46	156.14	5.1
N K	11.85	11.3	5.47	33.28
O K	33.81	28.24	48.06	11.48

C) Treated

D)

Element	Weight %	Atomic %	Net Int.	Error %
C K	22.78	32.27	46.84	10.36
N K	5.32	6.46	0.39	14.74
O K	42.83	45.66	222.32	9.24
Si K	23.6	14.3	716.31	3.26
Ag L	1.8	0.28	29.48	9.04
Fe K	3.67	1.12	30.79	4.92
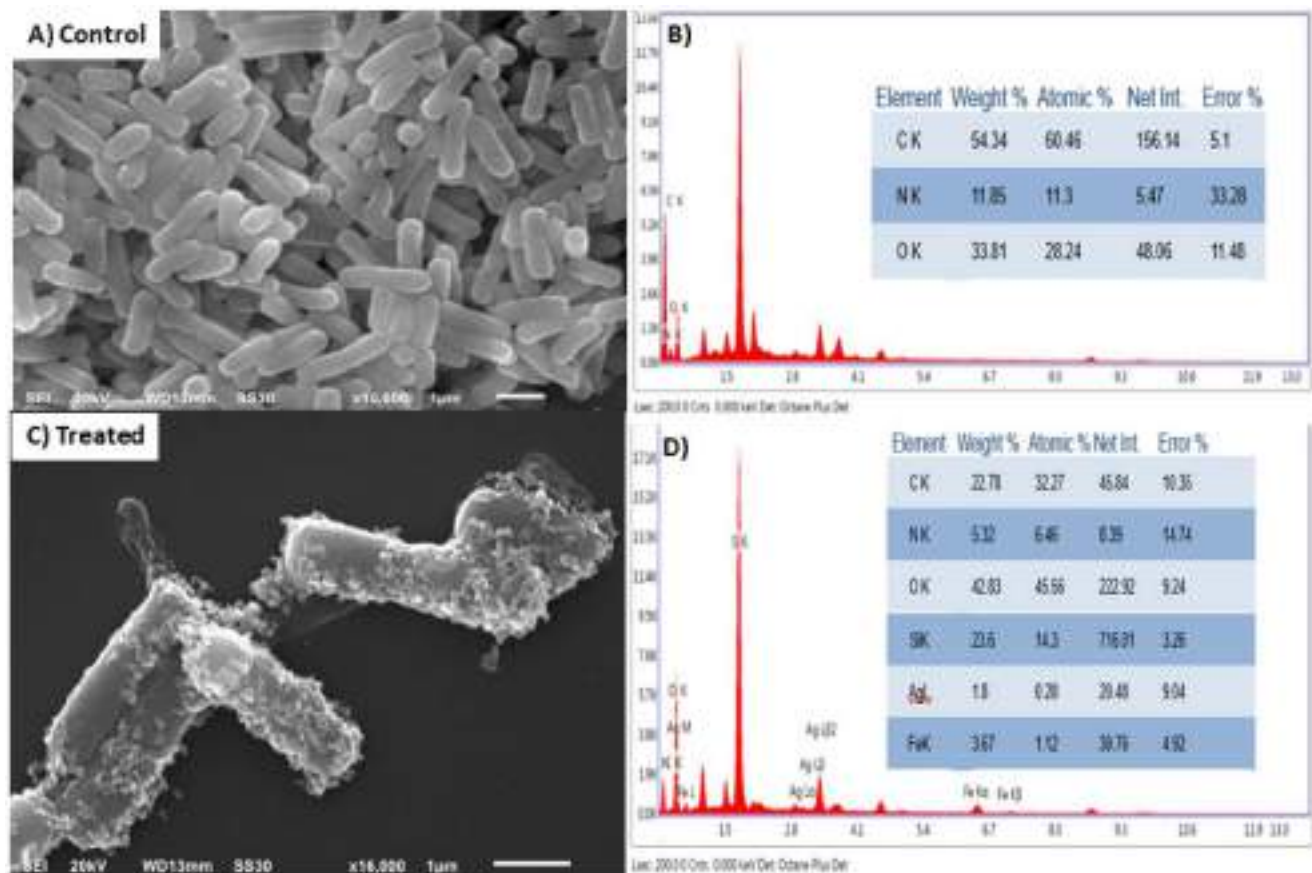
Figure 12. Scanning electron micrographs of (A) and (B) untreated *P. aeruginosa* cells and its EDAX composition (C) and (D) cells treated with Fe$_3$O$_4$@SiO$_2$@PDA@Ag nanocomposites at MIC and its EDAX composition.
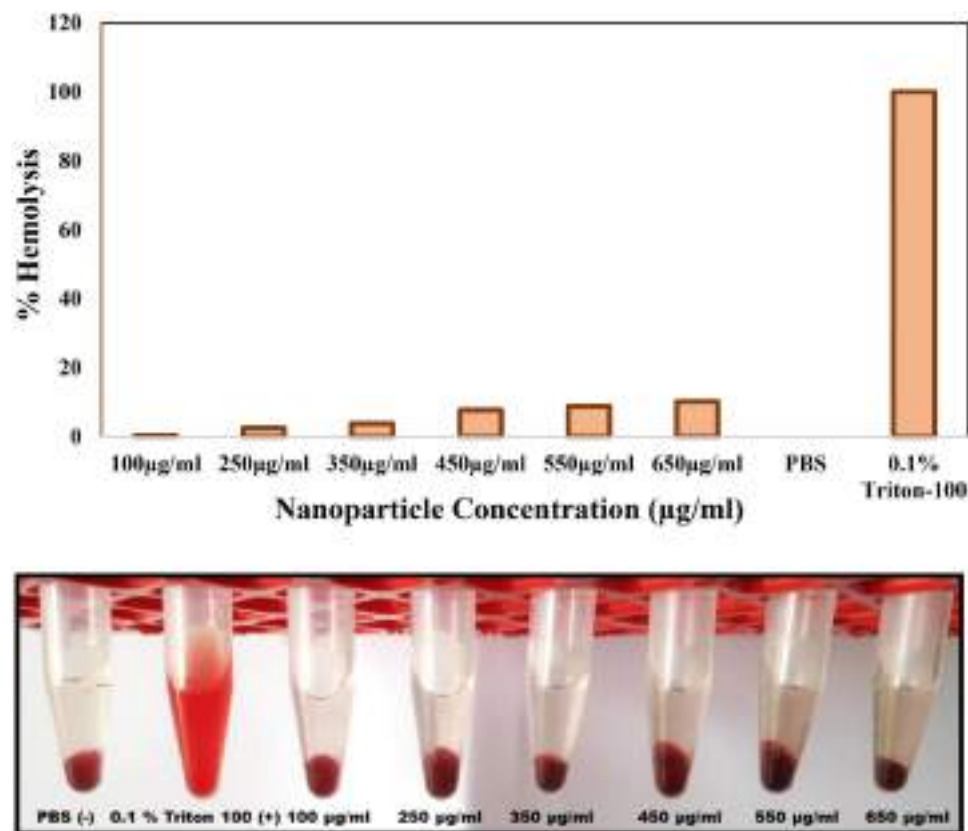
Figure 13. Haemolysis assay of Fe$_3$O$_4$@SiO$_2$@PDA@Ag nanoparticle at various concentrations.

observations demonstrated that these nanoparticles can be used directly or can be used as a drug delivery agent, which can reduce their toxicity on human cells (Figure 13).

6. Conclusion

Lung cancer is the most aggressive human cancer and a leading cause of death worldwide. Here, we have reported a simple protocol to synthesise Ag-wrapped $Fe_3O_4@SiO_2@PDA$ nanocomposites. The anticancer and antibacterial activity displayed by the Ag nanocomposites reported here represent a better alternative to available options. We have also shown the mode of cell death using apoptosis assay and biocompatibility of synthesised nanocomposites using haemolysis assay. The nanocomposites have effusively demonstrated their antibacterial activity against Gram-positive and Gram-negative bacteria but with different susceptibilities at the same concentration range. Thus, the ordinance of these nanocomposites serves as a lucrative option in this ever-evolving era of bacterial infections.

Disclosure statement of interest

The authors declare no potential competing interest.

ORCID

Snigdha Singh http://orcid.org/0000-0003-0319-8887
Ramesh Chandra http://orcid.org/0000-0002-3040-997X

Data availability statement

Raw data available on request.

Author's contribution

R.C, S.S., and T.G. contributed to the idea or design of the work. S.S, A.S., T.G. and H.C. performed the nanoparticle synthesis, characterization, analysis and interpretation of data for the work. H.C. and T.G. performed the anticancer activity and did the interpretation of the results. T.G. and M.T. did the apoptosis experiment and analysed the data. N.C. and I.R. did the antibacterial experiments and analysed the data. R.C., S.S. and M.T. supervised the project. S.S., A.S., T.G, H.C., N.C., I.R., M.T. and R.C. contributed to the drafting of the work, reviewing the intellectual content of the manuscript. All authors have agreed to the final version, helped in analysis of the data and provided critical feedbacks during the writing and revision of the manuscript.

References

[1] Ferlay J, Colombet M, Soerjomataram I, et al. Cancer statistics for the year 2020: an overview. Int J Cancer. 2021;149(4):778–789. doi: 10.1002/ijc.33588.

[2] Esteban EC, Rullán JAD, Castillo PB, et al. Current role of nanoparticles in the treatment of lung cancer. Campos J Clin Transl Sci. 2021;7:140–155.

[3] Baig N, Kammakakam I, Falath W. Nanomaterials: a review of synthesis methods, properties, recent progress, and challenges. Mater Adv. 2021;2(6):1821–1871. doi: 10.1039/D0MA00807A.

[4] Dabagh S, Haris SA, Isfahani BK, et al. Silver-decorated and silica-capped magnetite nanoparticles with effective antibacterial activity and reusability. ACS Appl Bio Mater. 2023;6(6):2266–2276. doi: 10.1021/acsabm.3c00122.

[5] Pei J, Fu B, Jiang L, et al. Biosynthesis, characterization, and anticancer effect of plant-mediated silver nanoparticles using coptis chinensis. Int J Nanomed. 2019;14:1969–1978. doi: 10.2147/IJN.S188235.

[6] Romdoni Y, Kadja GTM, Kitamoto Y, et al. Synthesis of multifunctional Fe3O4@SiO2-Ag nanocomposite for antibacterial and anticancer drug delivery. Appl Surf Sci. 2022;610:155610. doi: 10.1016/j.apsusc.2022.155610.

[7] Austin LA, Mackey MA, Dreaden EC, et al. The optical, photothermal, and facile surface chemical properties of gold and silver nanoparticles in biodiagnostics, therapy, and drug delivery. Arch Toxicol. 2014;88(7):1391–1417. doi: 10.1007/s00204-014-1245-3.

[8] Mohanta YK, Biswas K, Panda SK, et al. Phyto-assisted synthesis of bio-functionalised silver nanoparticles and their potential anti-oxidant, anti-microbial and wound healing activities. IET Nanobiotechnol. 2017;11(8):1027–1034. doi: 10.1049/iet-nbt.2017.0017.

[9] Zahran M, Khalifa Z, Zahran MA-H, et al. Recent advances in silver nanoparticle-based electrochemical sensors for determining organic pollutants in water: a review. Mater Adv. 2021;2(22):7350–7365. doi: 10.1039/D1MA00769F.

[10] Wang ZX, Chen CY, Wang Y, et al. Ångstrom-scale silver particles as a promising agent for low-toxicity broad-spectrum potent anticancer therapy. Adv Funct Mater. 2019;29:1808556.

[11] Stensberg MC, Wei Q, McLamore ES, et al. Toxicological studies on silver nanoparticles: challenges and opportunities in assessment, monitoring and imaging. Nanomedicine (Lond). 2011;6(5):879–898. doi: 10.2217/nnm.11.78.

[12] Algotiml R, Gab-Alla A, Seoudi R, et al. Anticancer and antimicrobial activity of biosynthesized Red Sea marine algal silver nanoparticles. Sci Rep. 2022;12(1):2421. doi: 10.1038/s41598-022-06412-3.

[13] Liu L, Wang M, Liu C, et al. Effective gene delivery based on facilely synthesized "core–shell" Ag@PDA@PEI nanoparticles. J Nanopart Res. 2022;24(9):184. doi: 10.1007/s11051-022-05571-8.

[14] Pieretti JC, Rolim WR, Ferreira FF, et al. Synthesis, characterization, and cytotoxicity of Fe3O4@Ag hybrid nanoparticles: promising applications in cancer treatment. J Clust Sci. 2020;31(2):535–547. doi: 10.1007/s10876-019-01670-0.

[15] He Y, Du Z, Ma S, et al. Effects of green-synthesized silver nanoparticles on lung cancer cells in vitro and grown as xenograft tumors in vivo. Int J Nanomedicine. 2016;11:1879–1887. doi: 10.2147/IJN.S103695.

[16] Gengan RM, Anand K, Phulukdaree A, et al. A549 lung cell line activity of biosynthesized silver nanoparticles using albizia adianthifolia leaf. Colloids Surf B Biointerf. 2013;105:87–91. doi: 10.1016/j.colsurfb.2012.12.044.

[17] Silva AC, Oliveira TR, Mamani JB, et al. Application of hyperthermia induced by superparamagnetic iron oxide nanoparticles in glioma treatment. Int J Nanomed. 2011;6:591–603. doi: 10.2147/IJN.S14737.

[18] Tian S, Saravanan K, Mothana RA, et al. Anti-cancer activity of biosynthesized silver nanoparticles using avicennia marina against A549 lung cancer cells through ROS/mitochondrial damages.

Saudi J Biol Sci. 2020;27(11):3018–3024. doi: 10.1016/j.sjbs.2020.08.029.

[19] Jeyaraj M, Rajesh M, Arun R, et al. An investigation on the cytotoxicity and caspase-3-mediated apoptotic effect of biologically synthesized silver nanoparticles using podophyllum hexandrum on human cervical carcinoma cells. Colloids Surf B Biointerf. 2013;102:708–717. doi: 10.1016/j.colsurfb.2012.09.042.

[20] Rashidipour M, Heydari R. Biosynthesis of silver nanoparticles using extract of olive leaf: synthesis and in vitro cytotoxic effect on MCF-7 cells. J Nanostructure Chem. 2014;4:112.

[21] Heydari R, Rashidipour M. Green synthesis of silver nanoparticles using extract of oak fruit hull (jaft): synthesis and in vitro cytotoxic effect on MCF-7 cells. Int J Breast Cancer. 2015;2015:846743–846746. doi: 10.1155/2015/846743.

[22] Sangour MH, Ali IM, Atwan ZW, et al. Effect of Ag nanoparticles on viability of MCF-7 and vero cell lines and gene expression of apoptotic genes. Egypt J Med Hum Genet. 2021;22(1):9. doi: 10.1186/s43042-020-00120-1.

[23] Miyazawa N, Hakamada M, Mabuchi M. Antimicrobial mechanisms due to hyperpolarisation induced by nanoporous Au. Sci Rep. 2018;8(1):3870. doi: 10.1038/s41598-018-22261-5.

[24] Wang L, Hu C, Shao L. The antimicrobial activity of nanoparticles: present situation and prospects for the future. Int J Nanomed. 2017;12:1227–1249. doi: 10.2147/IJN.S121956.

[25] Quirós J, Borges JP, Boltes K, et al. Antimicrobial electrospun silver-, copper- and zinc-doped polyvinylpyrrolidone nanofibers. J Hazard Mater. 2015;299:298–305. doi: 10.1016/j.jhazmat.2015.06.028.

[26] Heydari R, Koudehi MF, Pourmortazavi SM. Antibacterial activity of Fe3O4/Cu nanocomposite: green synthesis using *Carum carvi* L. Seeds Aqueous Extract. Chemistry Select. 2019.

[27] Bezza FA, Tichapondwa SM, Chirwa EMN. Fabrication of monodispersed copper oxide nanoparticles with potential application as antimicrobial agents. Sci Rep. 2020;10(1):16680. doi: 10.1038/s41598-020-73497-z.

[28] Agnihotri S, Bajaj G, Mukherji S, et al. Arginine-assisted immobilization of silver nanoparticles on ZnO nanorods: an enhanced and reusable antibacterial substrate without human cell cytotoxicity. Nanoscale. 2015;7(16):7415–7429. doi: 10.1039/c4nr06913g.

[29] Fekri MH, Tousi F, Heydari R, et al. Synthesis of magnetic novel hybrid nanocomposite (Fe3O4@SiO2/activated carbon by a green method and evaluation of its antibacterial potential. Iran J Chem Chem Eng. 2022;41:767–776.

[30] Chi Y, Yuan Q, Li Y, et al. Synthesis of Fe3O4@SiO2–Ag magnetic nanocomposite based on small-sized and highly dispersed silver nanoparticles for catalytic reduction of 4-nitrophenol. J Colloid Interface Sci. 2012;383(1):96–102. doi: 10.1016/j.jcis.2012.06.027.

[31] Pallavicini P, Taglietti A, Dacarro G, et al. Self-assembled monolayers of silver nanoparticles firmly grafted on glass surfaces: low Ag + release for an efficient antibacterial activity. J Colloid Interface Sci. 2010;350(1):110–116. doi: 10.1016/j.jcis.2010.06.019.

[32] Farzad E, Veisi H. Fe3O4/SiO2 nanoparticles coated with polydopamine as a novel magnetite reductant and stabilizer sorbent for palladium ions: synthetic application of Fe3O4/SiO2@PDA/Pd for reduction of 4-nitrophenol and suzuki reactions. J. IndusEng Chem. 2018;60:114–124. doi: 10.1016/j.jiec.2017.10.017.

[33] Sharma RK, Dutta S, Sharma S, et al. Fe3O4 (iron oxide)-supported nanocatalysts: synthesis, characterization and applications in coupling reactions. Green Chem. 2016;18(11):3184–3209. doi: 10.1039/C6GC00864J.

[34] Qianjun H, Jianlin S. Mesoporous silica nanoparticle based nano drug delivery systems: synthesis, controlled drug release and delivery, pharmacokinetics and biocompatibility. J Mater Chem. 2011;21(16):5845–5855. doi: 10.1039/c0jm03851b.

[35] Dolui SK, Das D, Choudhury P, et al. Synthesis and characterization of SiO2/polyaniline/Ag core-shell particles and studies of 2 their electrical and hemolytic properties: multifunctional core-shell particles. RSC Adv. 2014, 5, 2360–2367.

[36] Abbas M. Fe3O4/SiO2 core/shell nanocubes: novel coating approach with tunable silica thickness and enhancement in

stability and biocompatibility. J Nanomed Nanotechnol. 2014;5(06), 244. doi: 10.4172/2157-7439.1000244.

[37] Lee H, Dellatore SM, Miller WM, et al. Mussel-Inspired surface chemistry for multifunctional coatings. Science. 2007;318(5849):426–430. doi: 10.1126/science.1147241.

[38] Murari G, Bock N, Zhou H, et al. Effects of polydopamine coatings on nucleation modes of surface mineralization from simulated body fluid. Sci Rep. 2020;10(1):14982. doi: 10.1038/s41598-020-71900-3.

[39] Barclay TG, et al. Versatile surface modification using polydopamine and related polycatecholamines: chemistry, structure, and applications. Adv Mater Interf. 2017;4:1601192.

[40] Hong SH, et al. Sprayable ultrafast polydopamine surface modifications. Adv Mater Interf. 2016;3:1500857.

[41] Ryu JH, Messersmith PB, Lee H. Polydopamine surface chemistry: a decade of discovery. ACS Appl Mater Interf. 2018;10(9):7523–7540. doi: 10.1021/acsami.7b19865.

[42] Baskoutas S. Solid-state synthesis of Ag-doped PANI nanocomposites for their end-use as an electrochemical sensor for hydrogen peroxide and dopamine. Electrochim Acta. 2020, 363, 137158.

[43] Zhang N, Peng S, Liu Z, et al. Ag NPs decorated on the magnetic Fe3O4@PDA as efficient catalyst for organic pollutants removal and as effective antimicrobial agent for microbial inhibition. J Alloys Compd. 2022;928:167257. doi: 10.1016/j.jallcom.2022.167257.

[44] Wang G, Yang F, Huang W, et al. Recyclable Mussel-Inspired magnetic nanocellulose@polydopamine–Ag nanocatalyst for efficient degradation of refractory organic pollutants and bacterial disinfection. ACS Appl Mater Interf. 2022;14(46):52359–52369. doi: 10.1021/acsami.2c13915.

[45] Nikmah A, Taufiq A, Hidayat A, et al. Excellent antimicrobial activity of Fe3O4/SiO2/Ag nanocomposites. NANO Brief Rep Rev. 2021;16:2150049. doi: 10.1142/S1793292021500491.

[46] Lv B, Xu Y, Tian H, et al. Synthesis of Fe3O4\SiO2\Ag nanoparticles and its application in surface-enhanced Raman scattering. J Solid State Chem. 2010;183(12):2968–2973. doi: 10.1016/j.jssc.2010.10.001.

[47] Sun M, Zhao A, Wang D, et al. Cube-like Fe3O4@SiO2@Au@Ag magnetic nanoparticles: a highly efficient SERS substrate for detection of pesticide. Nanotechnology. 2018;29(16):165302. doi: 10.1088/1361-6528/aaae42.

[48] Gupta R, Yadav M, Gaur R, et al. A straightforward one-pot synthesis of bioactive N-aryl oxazolidin-2-ones via a highly efficient Fe3O4@SiO2-supported acetate-based butylimidazolium ionic liquid nanocatalyst under metal- and solvent-free conditions. Green Chem. 2017;19(16):3801–3812. doi: 10.1039/C7GC01414G.

[49] Yu X, Cheng G, Zheng SY. Synthesis of self-assembled multifunctional nanocomposite catalysts with highly stabilized reactivity and magnetic recyclability. Sci Rep. 2016;6:25459. doi: 10.1038/srep25459.

[50] Liaqat N, Jahan N, Anwar T, et al. Green synthesized silver nanoparticles: optimization, characterization, antimicrobial activity, and cytotoxicity study by hemolysis assay. Front Chem. 2022;10:952006. doi: 10.3389/fchem.2022.952006.

[51] Yadav S, Deka SR, Verma G, et al. Photoresponsive amphiphilicazobenzene–PEG self-assembles to form supramolecular nanostructures for drug delivery applications. RSC Adv. 2016;6(10):8103–8117. doi: 10.1039/C5RA26658K.

[52] Shivhare K, Garg C, Priyam A, et al. Enzyme sensitive smart inulin-dehydropeptide conjugate self-assembles into nanostructures useful for targeted delivery of ornidazole. Int J Biol Macromol. 2018;106:775–783. doi: 10.1016/j.ijbiomac.2017.08.071.

[53] Fuentes-García JA, Diaz-Cano AI, Guillen-Cervantes A, et al. Magnetic domain interactions of Fe3O4 nanoparticles embedded in a SiO2 matrix. 2018;8:5096.

[54] Kalishwaralal K, Deepak V, Ramkumarpandian S, et al. Extracellular biosynthesis of silver nanoparticles by the culture supernatant of *Bacillus licheniformis*. Mater Lett. 2008;62(29):4411–4413. doi: 10.1016/j.matlet.2008.06.051.